N° d'ordre: 2012 ISAL 0031 Année 2012

THESE

présentée devant

L'INSTITUT NATIONAL DES SCIENCES APPLIQUEES DE LYON

Pour obtenir

LE GRADE DE DOCTEUR

École doctorale : **Mécanique, Energétique, Génie Civil, Acoustique (MEGA)**

Spécialité: **MÉCANIQUE**

Par

Xiaoyu GU

(Ingénieur de l'Université Nord–EST - Chine)

INFLUENCE OF PLANET POSITION ERRORS AND ECCENTRICITIES ON PLANETARY GEAR DYNAMICS

INFLUENCE DES ERREURS DE POSITION ET EXCENTRICITES SUR LA DYNAMIQUE D'UN TRAIN PLANETAIRE

Soutenue le **11 Avril 2012** devant la Commission d'Examen

Jury :			
	M. Samuel BECQUERELLE	**Ingénieur de Recherche**	**Examinateur**
	M. Georges JACQUET-RICHARDET	**Professeur**	**Président**
	M. Robert G. PARKER	**Professeur**	**Rapporteur**
	M. Karsten STAHL	**Professeur**	**Rapporteur**
	M. Philippe VELEX	**Professeur**	**Directeur de thèse**

LaMCoS - UMR CNRS 5259 - INSA de Lyon
18-20, rue des Sciences, 69621 Villeurbanne Cedex (France)

INSA Direction de la Recherche - Ecoles Doctorales – Quinquennal 2011-2015

SIGLE	ECOLE DOCTORALE	NOM ET COORDONNEES DU RESPONSABLE
CHIMIE	**CHIMIE DE LYON** **http://www.edchimie-lyon.fr** Insa : R. GOURDON	M. Jean Marc LANCELIN Université de Lyon – Collège Doctoral Bât ESCPE 43 bd du 11 novembre 1918 69622 VILLEURBANNE Cedex Tél : 04.72.43 13 95 directeur@edchimie-lyon.fr
E.E.A.	**ELECTRONIQUE, ELECTROTECHNIQUE, AUTOMATIQUE** **http://edeea.ec-lyon.fr** Secrétariat : M.C. HAVGOUDOUKIAN eea@ec-lyon.fr	M. Gérard SCORLETTI Ecole Centrale de Lyon 36 avenue Guy de Collongue 69134 ECULLY Tél : 04.72.18 60 97 Fax : 04 78 43 37 17 Gerard.scorletti@ec-lyon.fr
E2M2	**EVOLUTION, ECOSYSTEME, MICROBIOLOGIE, MODELISATION** **http://e2m2.universite-lyon.fr** Insa : H. CHARLES	Mme Gudrun BORNETTE CNRS UMR 5023 LEHNA Université Claude Bernard Lyon 1 Bât Forel 43 bd du 11 novembre 1918 69622 VILLEURBANNE Cédex Tél : 04.72.43.12.94 e2m2@univ-lyon.fr
EDISS	**INTERDISCIPLINAIRE SCIENCES-SANTE** **http://ww2.ibcp.fr/ediss** Sec : Safia AIT CHALAL Insa : M. LAGARDE	M. Didier REVEL Hôpital Cardiologique de Lyon Bâtiment Central 28 Avenue Doyen Lépine 69500 BRON Tél : 04.72.68 49 09 Fax :04 72 35 49 16 Didier.revel@creatis.uni-lyon1.fr
INFOMATHS	**INFORMATIQUE ET MATHEMATIQUES** http://infomaths.univ-lyon1.fr	M. Johannes KELLENDONK Université Claude Bernard Lyon 1 LIRIS - INFOMATHS Bâtiment Nautibus 43 bd du 11 novembre 1918 69622 VILLEURBANNE Cedex Tél : 04.72. 43.19.05 Fax 04 72 43 13 10 infomaths@bat710.univ-lyon1.fr
Matériaux	**MATERIAUX DE LYON** Secrétariat : M. LABOUNE PM : 71.70 –Fax : 87.12 Bat. Saint Exupéry	M. Jean-Yves BUFFIERE INSA de Lyon MATEIS Bâtiment Saint Exupéry 7 avenue Jean Capelle 69621 VILLEURBANNE Cédex Tél : 04.72.43 83 18 Fax 04 72 43 85 28 Jean-yves.buffiere@insa-lyon.fr
MEGA	**MECANIQUE, ENERGETIQUE, GENIE CIVIL, ACOUSTIQUE** Secrétariat : M. LABOUNE PM : 71.70 –Fax : 87.12 Bat. Saint Exupéry mega@insa-lyon.fr	M. Philippe BOISSE INSA de Lyon Laboratoire LAMCOS Bâtiment Jacquard 25 bis avenue Jean Capelle 69621 VILLEURBANNE Cedex Tél :04.72.43.71.70 Fax : 04 72 43 72 37 Philippe.boisse@insa-lyon.fr
ScSo	**ScSo*** M. OBADIA Lionel Sec : Viviane POLSINELLI Insa : J.Y. TOUSSAINT	M. OBADIA Lionel Université Lyon 2 86 rue Pasteur 69365 LYON Cedex 07 Tél : 04.78.69.72.76 Fax : 04.37.28.04.48 Lionel.Obadia@univ-lyon2.fr

*ScSo : Histoire, Geographie, Aménagement, Urbanisme, Archéologie, Science politique, Sociologie, Anthropologie

To My Parents & Husband

Acknowledgments

I would like to express my sincere appreciation to my advisor Professor Philippe Velex for accepting me as his student, for his professional support, guidance, invaluable advice and patience over the entire Ph.D programme. It has been a great honour to work with him. This thesis would have not been possible without his help, support and confidence.

I would like to thank Prof. R. G. Parker from Michigan-Shanghai Jiao Tong University and Prof. K. Stahl from Munich Technical University for their careful review of the memoir. The contributions of the other members of the jury, Prof. G. Jacquet-Richardet from INSA Lyon, Mr. S. Becquerelle (Hispano-Suiza) are also gratefully acknowledged.

I would like to take this opportunity to express my heartfelt thanks to Dr. J. Bruyère and Mr. D. Ghribi for helping me in my research and personal life, for their unremitting support and deep understanding during this time. I also would like to thanks Dr. F. Ville., Mrs. M. Bouvier, P. Aeby, J. Cavoret and my fellow graduate students: N. Feki, R. Fargère, J. Wang and T. Osman, for their continuous help and support over these last three years.

I also thank my parents, my husband, my sister for their utmost love and constant encouragement. Special thanks to my friends: F. Deng, N. Wang, F. Duan, T. Li, S. Chen for their advice and kind help during my stay at INSA Lyon.

Finally, I would like to gratefully acknowledge the financial support of the China Scholarship Council (CSC) in collaboration with the French government through an Overseas Research Scholarship Programme.

I haven't failed. I've just found 10,000 ways that won't work.

Abstract

A dynamic model of planetary gears is presented which accounts for planet position errors and eccentricities for either rigid mounts or floating members. The theoretical formulation relies on infinitesimal generalised displacement screws which can simulate both errors and deflections. A unique feature of this model is that mesh properties (geometry and excitations) are coupled with the degrees-of-freedom thus leading to complex frequency and amplitude modulated excitation sources. For a number of planetary gears, it is found that the simulated load sharing between the planets compare well with the experimental evidence thus validating the contact modelling strategy. Finally, the results of extensive parameter analyses are displayed which illustrate the role of certain errors along with the interest and drawbacks of floating sun-gears or planets in high-speed applications.

Keywords: Planetary gears, Dynamics, Errors, Floating members, Tooth forces, Trajectories, Critical speeds.

Résumé

Un modèle de trains planétaires est proposé afin de tenir compte de l'influence d'erreurs de position et d'excentricités en lien avec d'éventuels montages 'flottants' sur le comportement dynamique d'une transmission. La formulation théorique repose sur le formalisme des torseurs de déplacements infinitésimaux pour simuler à la fois les erreurs géométriques et les degrés de liberté du modèle. Une des propriétés principales de cette approche est que la géométrie des engrènements et les excitations correspondantes sont couplées aux degrés de liberté, conduisant ainsi à des excitations complexes présentant des modulations d'amplitude et de phase. Les résultats de simulation sont comparés avec des mesures sur banc d'essai et un très bon accord est obtenu en terme de partage de charge entre les satellites, validant ainsi le modèle de contact développé. Enfin, des résultats d'études paramétriques portant sur le rôle de certaines erreurs ainsi que sur l'apport éventuel de solaire et/ou satellites flottants dans des applications grandes vitesses concluent ce travail de thèse.

Mots Clés: Trains planétaires, Comportement dynamique, Erreurs de montage, Excentricités, Membres flottants, Charges sur les contacts, Trajectoires, Vitesses critiques.

Table of contents

List of figures

CHAPTER I:

CHAPTER II:

CHAPTER III:

CHAPTER IV:

List of tables

CHAPTER I:

CHAPTER II:

CHAPTER III:

CHAPTER IV:

Nomenclature

$\mathbf{C}$	:damping matrix
e_j	:eccentricity error of planet #j
e_k	:eccentricity error of centre member (sun-gear (k =S), carrier (k =C) , ring-gear (k=R))
e_{xj}, e_{yj}	:radial and tangential position errors of planet #j
$\mathbf{F}_{gj}(t, \mathbf{X}_{gj})$	:elastic contribution to mesh force caused by initial separation
$\mathbf{F}_{\mathbf{KE}}$	:total elastic contributions to mesh forces caused by initial separations
$\mathbf{F}_0$	:constant force vector (torque)
$\mathbf{F}_{\dot{\Omega}}(t)$	:inertial forcing terms due to unsteady rigid-body rotational speeds
$\mathbf{I}_{G_i}$	:polar moment of inertia of solid i
$k_{gj}(t, \mathbf{X}_{gj})$	:time-varying possibly nonlinear mesh stiffness function associated with mesh #j
$k_{kx}, k_{ky}, k_{k\theta}$	:bearing stiffness elements (two translational directions, and one rotational
$\mathbf{K_b}$	:total bearing stiffness matrix
$\mathbf{K}_G(t, \mathbf{X})$	:global time-varying possibly nonlinear mesh stiffness matrix
$\mathbf{K}_{gj}(t, \mathbf{X}_{gj})$	:time-varying possibly nonlinear mesh stiffness matrix associated with mesh #j direction)
$\overline{\mathbf{K}}$	:average global stiffness matrix
m_i	:mass of solid i
$\mathbf{M}$	:global mass matrix
$\mathbf{n}_j / \mathbf{n}_j', \mathbf{n}_j^* / \mathbf{n}_j^*{}'$	:constant/variable outward unit normal vector to sun-gear and planet #j tooth flank
Ra_S, Ra_j	:addendum circle radius of sun-gear and planet #j
Rb_S, Rb_R, Rb_j	:base radius of sun-gear, ring-gear and planet #j
R_C, R_{gj}, R_{gj}'	:radius of carrier, constant / variable center distance of sun/ring gear-planet #j
Rt_R	:addendum circle radius of ring-gear
$\mathbf{X}$	:total DOF vector (3N+9 components, N: number of planets)
$\mathbf{X}_{kj}$	:elastic displacement vector of sun / ring /carrier-planet #j
U_j^*	:see equation (6)
$\mathbf{u}_k^{\Re}(\mathbf{O}_k), \mathbf{u}_j^{C}(\mathbf{O}_j)$	:translational displacement vector of solid k and planet #j relative to rigid-body motions
$\mathbf{u}_k^{\wp 1}(\mathbf{O}_k), \mathbf{u}_j^{\wp j}(\mathbf{O}_j)$	:translational displacement vector of solid k and planet #j relative to the rotating frames of $\{S_k^{\wp 1}\}, \{S_j^{\wp j}\}$

$\mathbf{u}_k^{\Re}\left(\mathbf{M}/\mathbf{M}^*\right),\mathbf{u}_j^{C}\left(\mathbf{M}/\mathbf{M}^*\right)$	:translational displacement vector at point $\mathbf{M}/\mathbf{M}^*$ relative to rigid body motions
$\mathbf{u}_k^{\Re}\left(G_k\right),\mathbf{u}_j^{C}\left(G_j\right)$	:eccentricity error vector at point G_k / G_j
$\mathbf{V}_{gj}$	:structural vector (dependent on gear geometry)
$\mathbf{V}_{\mathbf{S/R}}^{\mathbf{j}}(\mathbf{M}/\mathbf{M}^*)$	:relative velocities of sun/ring gear-planet j at the point of contact M or M^*
x_i, y_i	:translational degrees of freedom in $\mathbf{x}_i$ and $\mathbf{y}_i$ directions
$\alpha_{gj}, \alpha_{gj}'$	:pressure angle with constant and variable gear geometry
β_b	:base helix angle
$\delta\left(M_{gj}'\right)$	:deflection at any potential point of contact M_{gj}'
$\delta_j^*\left(M^*\right)$	:general expression of the separation at any point of contact M^*
$\delta e_j, \delta e_j^*$	:initial separations of sun/planet j, of ring/planet j, caused by position and eccentricities
$\Delta(M_{gj}')$	:contact deflection at M_{gj}'
ε_S	:+1 for sun-gear counter-clockwise rotation, $\varepsilon_S = -1$ otherwise
ζ	: $\zeta = +1$ if the ring-gear is fixed, $\zeta = 0$ if the carrier is fixed
θ_i	:torsional degree of freedom of solid i
λ_i	:initial position angle of eccentricity for solid i,(i = C, S, R, j)
φ_j, ϕ_k	:additional rigid-body angle induced by errors for planet j and for central members
Φ_j, Φ_{gj}'	:planet spacing angle for constant and variable gear geometry
ψ_i	:no-error rotational angle with respect to the carrier rotary frame $\psi_i = \Omega_{i0}t + \lambda_i$, i = C, S, R, j
$\boldsymbol{\omega}_k^{\Re}, \boldsymbol{\omega}_j^{C}$	:angular displacement vector of solids with respect to rigid-body motions
$\boldsymbol{\omega}_k^{\wp 1}, \boldsymbol{\omega}_j^{\wp j}$	:angular displacement vector of solids with respect to reference frame
$2\Omega_C\mathbf{D}, \Omega_C^2\mathbf{L}$	:gyroscopic matrix and centrifugal stiffness matrix induced by carrier rotation.
Ω_i^0	:angular velocity vector with respect to the inertial frame
$\Omega_k^{\Im}$	:angular velocity vector with respect to the carrier frame
$\dot{\Omega}_k^{\Im}$	:angular acceleration vector with respect to the carrier frame
$\vert\ \vert, \Vert\ \Vert$	:vector amplitude, remainder of natural division

Indices:

k=S, R, C	:sun-gear, ring-gear and carrier
i=S, R, C, #*j*	:sun-gear, ring-gear, carrier and planet #j
g= S, R	:sun-gear, ring-gear

GENERAL INTRODUCTION

Gears are present in all kinds of machinery and vehicles because of their advantages over other available methods of transmitting power and matching the speeds and torques of one machine to another. Gear transmissions usually exhibit high power-to-weight ratios, can be made very compact and present the major advantage of high efficiency. All industrial sectors are concerned and gears range in size from micro-mechanisms with diameters of less than 1mm up to the very large units of several meters in diameter found in mining and cement mills for example. Epicyclic or planetary gears are particularly useful for transmitting significant power with large speed reductions or multiplications. Their multiple paths of motion transfer from one central member to the output make them more reliable than conventional gear trains because the total power, hence the load, is divided between the various branches of the mechanism. Today, competitive pressure, the increasing power of prime-movers, the demand for higher speeds and environmental concerns combine to force the pace of development in favour of more efficient, more compact, more silent, less costly units, improvements which are achieved mostly as a result of better manufacturing techniques and material strength. Wind turbines, new generation aircraft engines, hybrid car transmissions are just some of the fields of application where planetary gears appear as key elements which, to a considerable extent, control the reliability and efficiency of the entire system. In particular, the growing interest in renewable energies has led to the development of the wind turbine industry, which is expected to accelerate in the future and drive technological challenges and improvements to planetary gear systems in order to reduce maintenance costs. Indeed, recent surveys have highlighted the fact that gears are critical elements in most rotating machineries since 60% of the failures occur on gear teeth and, for instance, planetary gear failures are recognised as a significant handicap in the wind turbine industry. In this context, one of the major drawbacks of planetary gears is their sensitivity to position and mounting errors which can greatly alter the load sharing between the various meshes thus leading to premature failures and/or vibration and noise. One technological solution consists in allowing certain members to ‘float’, i.e., to be supported by flexible mounts in order to generate a degree of self-balancing which, in turn, can generate dynamic problems in high-speed applications.

The main objective of this research work is to introduce planetary gear models capable of predicting the impact of classic errors in terms of vibrations and dynamic forces on gear tooth contacts. A number of sophisticated models have been recently introduced which can simulate planetary gears with great precision but mostly for quasi-static regimes. An alternative approach is therefore proposed in this memoir with a conceptually simple lumped-parameter dynamic model but with emphasis being placed on the precise dynamic modelling of errors with or without floating members. It is shown that the results even at low speeds compare well with the experimental evidence in the literature and some original results concerning high-speed applications are displayed. After a literature review on planetary gear dynamics, the theoretical formulation of an original dynamic model is developed which, to a great extent, relies on the formalism of infinitesimal displacement screws. The complex interactions between geometry, errors and displacements are tackled and an iterative scheme is set up which combines the solution of the equations of motion, the normal contact problem on the teeth and the coupling between degrees-of-freedom, mounting errors and gear mesh geometry and excitations. Finally, some static and dynamic results are shown which illustrate the versatility and efficiency of the proposed approach.

CHAPTER I

LITERATURE REVIEW

1 – Introduction
2 – Literature review on planetary gears
3 – Research objectives and thesis outline

1 – Introduction

The terminology ‘planetary transmission’ comes from the gear arrangement similar to that of planets in a solar system. A sun-gear is located at the centre of the mechanism and is in mesh with several planets which orbit around it. The planets are mounted on a carrier which can either be fixed or rotating. Figure 1 shows a schematic representation of a planetary gear set comprising planet gears (pinions), a sun-gear, a ring (internal)-gear and a planet carrier (a relatively rigid structure that supports the planets).

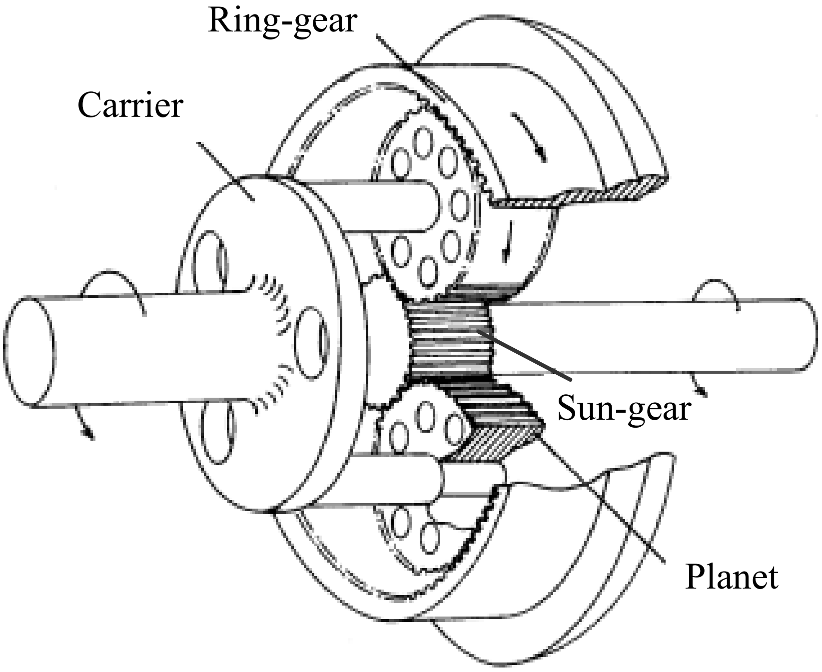

Figure 1 – Schematic representation of a planetary gear (Lynwander [1])

Mechanical transmissions by epicyclic or planetary gears have been applied in industry as early as 1781 when James Watt invented a system composed of a sun-gear and one planet for one of his machines. Lanchester (1895) is known as the first user of planetary gears in automotive gearboxes with the introduction of a compound planetary whose first stage ring-gear was the planet carrier of the second stage. Later, Stoeckicht introduced a number of extensions in aeronautics and marine transmissions based on flexible mounts and floating members in order to improve the load sharing amongst the various meshes.

Presently, planetary gear sets are recognised as particularly compact and efficient mechanisms used in a wide variety of machinery applications such as automobiles (Figure 2), aeronautics (Figure 3 helicopters and aircraft engines transmissions), robotics, wind turbines, gas turbine gear boxes, heavy machinery, marine and industrial power transmission systems.

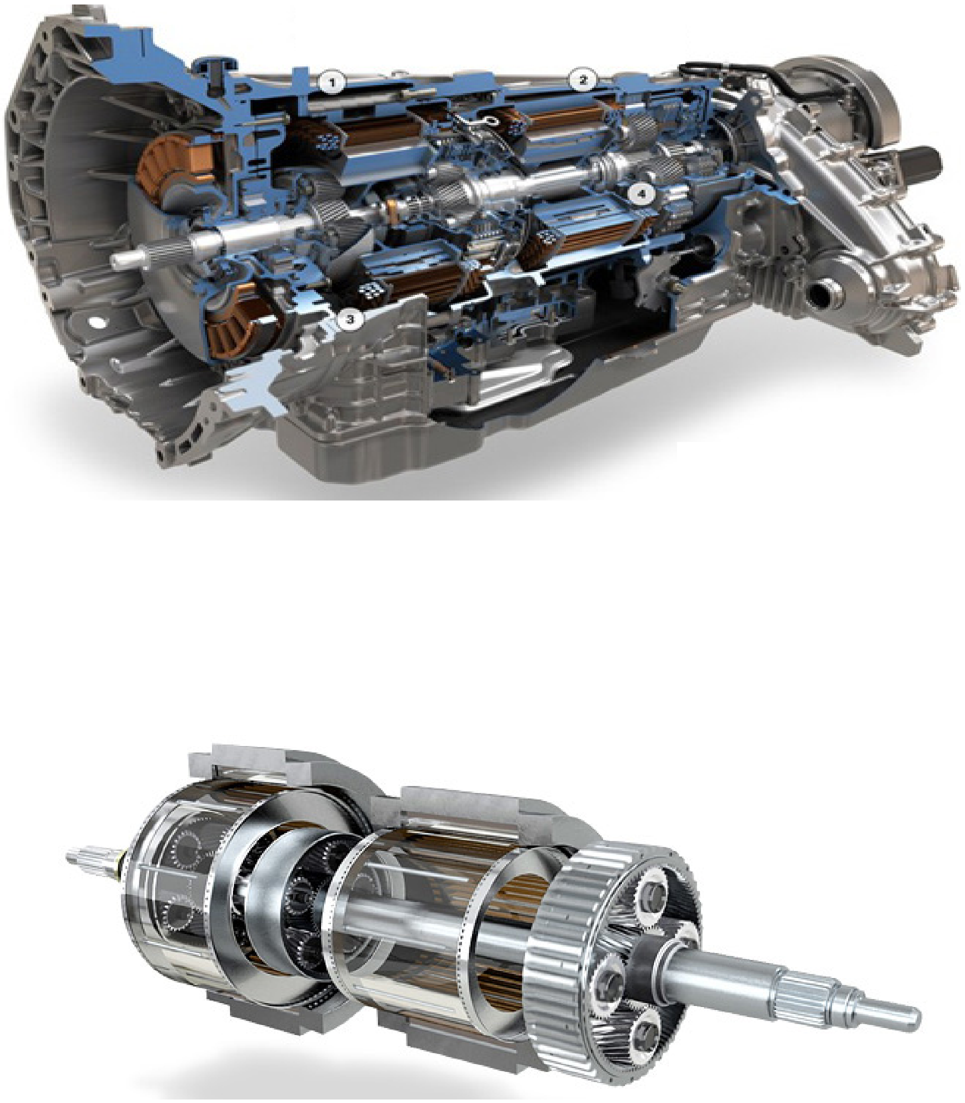

Figure 2 – BMW X6 Active Hybrid with three planetary gear sets [2-3]

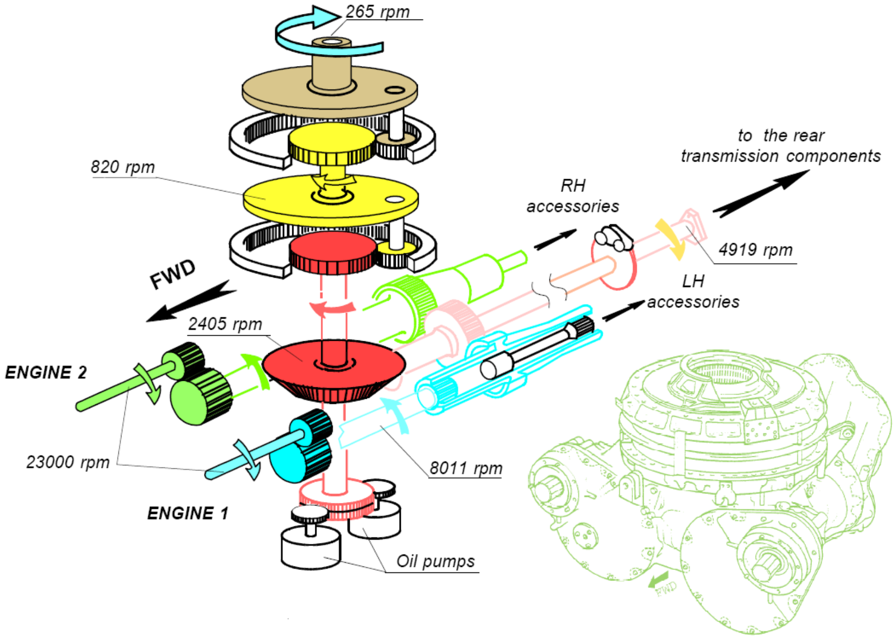

Figure 3 – Super puma main gear box drawing [4]

The advantages of planetary gears over parallel axis gears are:

a) Higher power densities (power-to-volume ratio) since the input torque is shared between several identical parallel sun-gear/planet/ring-gear branches thus leading to smaller, lighter gears compared with conventional gears.

b) Several speed ratios: different input-to-output speed (torque) ratios can be achieved with the same planetary gear set by simply changing the input, output and reaction (fixed) members. Through different power flow arrangements, the maximum admissible power can be increased simply by increasing the number of parallel paths, i.e., the number of pinions in the planetary gear set.

c) Compact and self-adaptability: compactness is provided by the coaxial arrangement of the parts which also offers self-centring capability. By allowing some of the central members (typically the sun gear) to float, the sensitivity of the gear set to various manufacturing errors can be minimized [1], [5].

d) Cancellation of radial bearing forces as long as the system is axi-symmetric and load is equally shared amongst the planets.

e) Relatively easier manufacturing since smaller gears are used (compared with conventional gear sets) which can be manufactured with more precision.

f) Higher efficiency: the power losses induced by tooth friction are decreased by the reduction of the tooth load and pitch line velocities. Similarly, bearing losses are diminished because smaller bearings can be used since the radial forces on the central members are reduced.

Despite their numerous advantages, planetary gears exhibit a number of drawbacks which should be considered in any design analysis:

a) Because of the number of meshes, they have a tendency to generate larger noise levels in operation.

b) Some members are highly loaded because of the multiple contacts and can develop significant failures. The compact gear arrangement makes tooth failure very destructive since a fractured tooth can damage several parts in the transmission.

c) The equal load sharing between all the planets in the epicyclic system corresponds to an ideal situation. In practice, however, variations in mesh stiffness along with manufacturing and mounting errors may generate not only noise and vibration but also contact and/or structural fatigue of the components. For example, in a number of helicopters, the final reduction stage of the planetary gears is directly connected to the helicopter cabin thus contributing strongly to the structure borne noise. This is confirmed by spectral analyses which clearly show that the mesh frequency and its harmonics are the dominant frequencies in terms of cockpit noise (Figure 4).

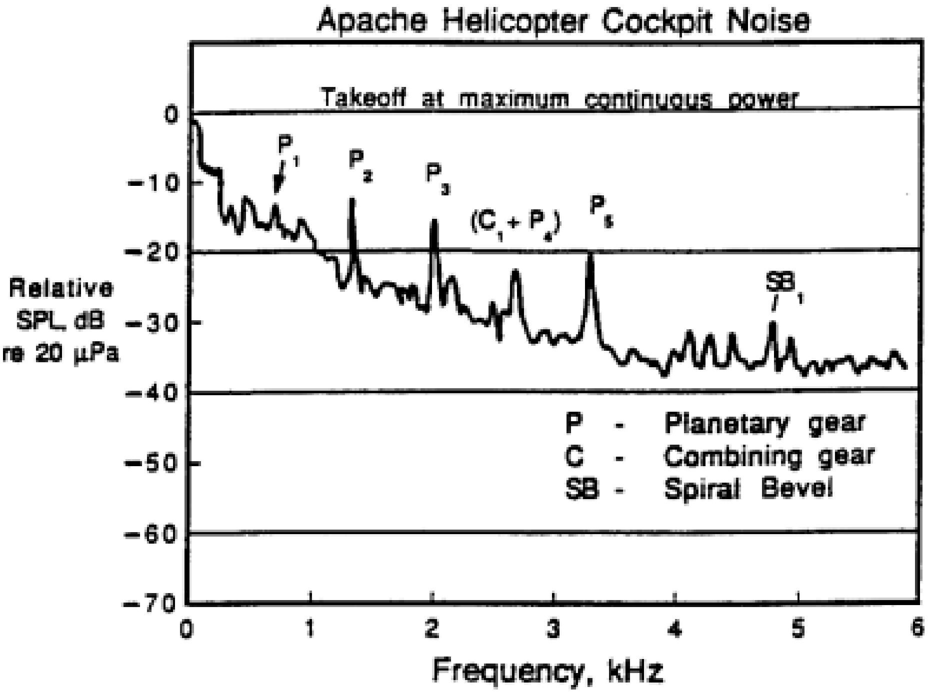

Figure 4 – Helicopter cabin noise spectra [6]

A rather similar situation is encountered in automatic gearboxes in which the gear vibration transferred via the bearings and the housing to the carriage, is usually recognized by passengers as a symbol of poor quality and reliability. This sensitivity to vibration is therefore recognised as a sensitive issue and justifies further research in planetary gear dynamics.

2 – Literature review on planetary gears

2.1 – Vibration sources in planetary gears

The excitations in geared systems are generally associated with: a) the instantaneous mesh stiffness variations associated with the contact length variations on tooth flanks, b) the various geometry and mounting errors on rotating parts and, c) the external load fluctuations, i.e. , the input and/or output torque variations. The dynamic response to time-varying input torque is generally easier to analyse than that induced by mesh stiffness parametric excitation and geometrical errors, which are the main topics tackled in this memoir.

2.1.1 – Mesh deflections, mesh stiffness

a) Mesh deflections

The deformation of a tooth pair in mesh is the result of both local phenomena (contact deflections) and more global contributions due to tooth bending, base rotation etc. A number of analytical methods can be found in the literature in order to estimate mesh stiffness. Contact deformations are generally determined by using the Hertzian theory and its variants. For structural deflections, Weber [7], and later Weber and Banascheck [8], Tavakoli and Houser [9], Lin et al. [10] assimilate a tooth to a cantilever of variable cross-section whose bending displacements can be determined by equating the work of the external force to the strain energy in the beam. The tooth root and base are modelled as an elastic half- plane submitted to a tangential and a normal force (Weber [7]). Extensions and variants of the methodology were introduced by O'Donnell [11-12] with regard to the foundation effects and by Attia [13], Cornell [14] among others, concerning the analytical developments. All these individual deflections are then superimposed for the pinion and the gear teeth and the resulting total displacement in the force direction leads to the mesh stiffness.

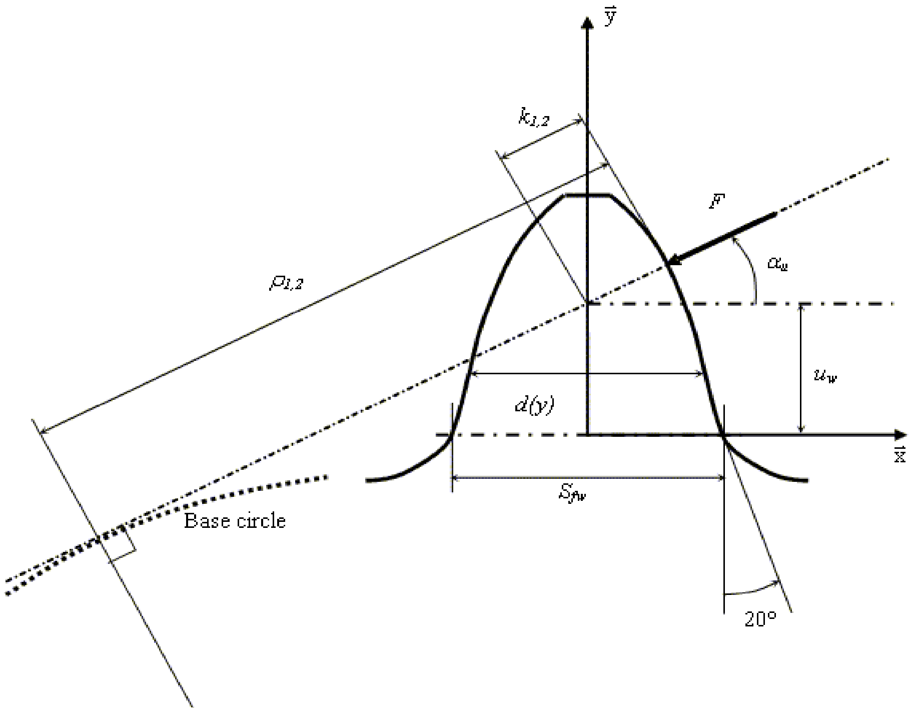

Figure 5 – Parameters for Weber's formulae

b) Contact deformation

Weber [7] analyzed the contact compliance by using the Hertzian 2D theory for two cylinders in contact with the datum for displacements taken at the tooth centre line and gave the normal approach between the contacting parts under the form:

$$\delta_c = 4\frac{F}{b}\frac{1-v^2}{\pi E}\left[\ln\frac{2\sqrt{k_1 k_2}}{a} - \frac{v}{2(1-v)}\right] \tag{1}$$

with:

δ_c : contact deformation in the direction of the force F

F: force on the tooth

b: tooth face width

k_1, k_2: distances between the point of contact and the tooth centre-line for the pinion and the gear respectively (see Figure 5)

$a = \sqrt{8\frac{F}{b}\frac{\rho_1\rho_2}{\rho_1+\rho_2}\frac{1-v^2}{\pi E}}$: contact half width (in the profile direction)

E, v: Young's modulus, Poisson's ratio

ρ_1, ρ_2: radii of curvature (see Figure 5)

Another widely-used formula is that of Lundberg [15] who considered the deflection at the centre of a semi-elliptic pressure band at the free surface of a 3D elastic half-space. The approximate Hertzian approach originally used at Hamilton Standard [14] and the semi-empirical formula developed by Palmgren for rollers [14].

c) Bending deformations

Tooth bending deformations can be derived by considering the tooth as a cantilever of variable cross-section and equating the strain energy to the work of the external force. The corresponding equation for bending displacements in the force direction reads:

$$\delta_b = \frac{F}{b}\frac{1}{E}\cos^2\alpha_u\left[10.92\int_0^{u_w}\frac{\left(u_w - y\right)^2}{d\left(y\right)^3}dy + 3.1\left(1+0.294tg^2\alpha_u\right)\int_0^{u_w}\frac{dy}{d\left(y\right)}\right] \tag{2}$$

where:

δ_b : bending deformation in the direction of the force F

α_u : pressure angle

u_w and d(y) are defined in Figure 5

b: tooth width

E: Young's modulus

The other parameters are defined in figure 5

d) Foundation or base displacement

The teeth are generally not fixed to a rigid part and the contribution of gear body elasticity must be taken into consideration. To this end, the tooth is now supposed to be rigid and the gear body is assimilated to an elastic half plane submitted to the contribution of normal and tangential stress determined at the built-in-edge of the cantilever (see above). Assuming a linear distribution of normal stress and a constant shear stress at the tooth root, an estimate of the displacement in the direction of the tooth load can be found under the form:

$$\delta_{fw} = \frac{F}{b}\frac{1}{E}\cos^2\alpha_u\left[L\left(\frac{u_w}{S_{fw}}\right)^2 + M\left(\frac{u_w}{S_{fw}}\right) + P\left(1+Qtg^2\alpha_u\right)\right] \tag{3}$$

with:

δ_{fw} : foundation or base displacement in the direction of the force F

S_{fw}: tooth thickness at the critical section according to Weber (see Figure 5)

L, M, P and Q : constants which slightly differ depending on the authors as indicated in Table 1.

Table 1 – Constants in Equation (3) for ν=0.3

	L	M	P	Q
Weber [7] - Attia [13]	5.2	1	1.4	0.294 - 0.32
Cornell*[14]	5.306	1.4 (plane stress) 1.14 (plane strain)	1.534	0.32

* *E for plane stress,* $E/(1-\nu^2)$ *for plane strain*

Although the equations above are based on a simplified bi-dimensional approach, they are still widely used in gear design. For example, the mesh stiffness formulae in the ISO standard 6336 [16] stem from (1)-(3), which were modified to bring the values in closer agreement with the experimental results.

Numerical methods such as the finite element method, the boundary element method and finite differences have also been extensively used, Chabert et al. [17], Wang and Cheng [18], Sainsot [19], etc., to name a few. In the context of three-dimensional gear dynamic simulations however, these methods may be not flexible enough and can still lead to heavy computational time constraints not compatible with parameter analyses, for instance.

e) Mesh stiffness functions

The mesh stiffness of one tooth pair in contact is deduced from the sum of the deflections listed above and varies depending on the position of the contact points on the profiles. Some simplified representations are often used in gear dynamics, Cai and Hayashi [20], Küçükay [21], Iwatsubo and Arii [21], Velex and Saada [23-24], etc., where the mesh stiffness per unit of contact length is supposed to be constant thus leading to periodic piecewise continuous mesh stiffness function (step functions for spur gears, trapezoidal functions for helical gears). It is to be noted that, even for perfect geometries, gears generate vibrations because of these parametric excitations (time-varying stiffness functions) as opposed to what is normally observed in rotating machinery where vibrations are often induced by defects such as imbalance, eccentricity, etc.

In planetary systems, planet mesh phase is known as an important parameter for the dynamic performance of planetary gear and has been analytically investigated by Seager [25], Kahraman [26], Kahraman and Blankenship [27]. Parker [28] has deduced the theoretical conditions for cancelling the mesh excitations on the central members (sun-gear, ring-gear) by the effectiveness of planet phasing. The author et al. [29], in particular, has produced an accurate description of the mesh phase relationships for sun-gear/planets and planets/ring-gear. Velex and Flamand [30] proposed a numerical method compatible with time step integrations which gives the positions of all the contacting points at all times from an arbitrary initial contact point. The displacement of the instantaneous contact lines and the corresponding mesh stiffness evolutions are calculated step by step according to rigid body motions.

2.1.2 – Tooth shape errors and mounting errors

Significant errors such as tooth profile deviations, position errors, run-out, thickness errors etc. are, to some extent, present in all gears because of machining inaccuracies, thermal distortions after heat treatments, assembly errors, etc. which, in practice, cannot be avoided. Such errors may induce partial or total contact losses; alter the motion transfer (transmission error) and the load sharing amongst the paths of transmission in multi-mesh gears. The classic tooth shape errors are listed and briefly described below:

a) Pitch errors

One usually separates:

i) The individual pitch error defined as the deviation between the actual measured pitch value between any adjacent tooth surface and the theoretical circular pitch.
ii) The pitch variation error measured between any two adjacent teeth.
iii) The accumulated pitch error which is the difference between the theoretical summation over any number of tooth intervals and the summation of the actual pitch measurement over the same interval.

b) Thickness errors

Thickness error is the amount by which the circular tooth thickness at the pitch circle differs from the nominal amount.

c) Tooth profile errors

Tooth profile error (Figure 6) is the summation of the deviations measured perpendicular to the actual profile between the actual tooth profile and the correct involute curve which passes through the pitch point. Note that tooth modifications are not considered as part of profile errors.

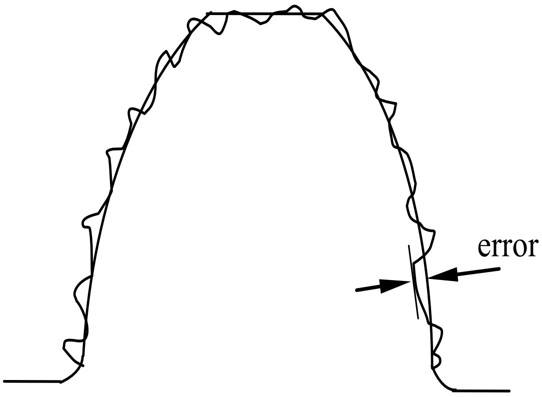

Figure 6 – Tooth profile errors

d) Tooth lead errors

Lead errors correspond to the deviations of the actual advance of the tooth profile from the ideal value or position. Lead errors result in distorted flank traces on the base plane and are likely to deteriorate tooth contacts, particularly by concentrating contacts in certain areas.

Apart from gear geometrical errors, the mounting/assembly precision of the various parts can strongly modify the static and dynamic loads on the tooth contacts. Some of the most significant mounting errors are listed below.

2.1.3 – Mounting / position errors

a) Planet position errors

In epicyclic gear systems, planet position error is defined as the error in the location of the planet centres which is decomposed into radial error (in the centre-line direction) and tangential position error (perpendicular to the radial error). It has been shown that these two kinds of error have a contrasted influence on planet loading: radial errors slightly modify centre-distances, pressure angles, etc. but remain far less influential than tangential errors which strongly modify planet load sharing.

b) Misalignment errors

Strictly speaking misalignments are three-dimensional error distributions which, when considering a single pinion-gear pair, are separated into a deviation and an inclination.

Following [34], misalignments can be simulated using displacement screws with two infinitesimal angles Φ_j^* and Ψ_j^* associated with solid j (Figure 7). Using the shifting property of screw moments, the displacement imposed at any potential point of contact in the base plane can be deduced leading to linear distributions of initial separations along the face widths.

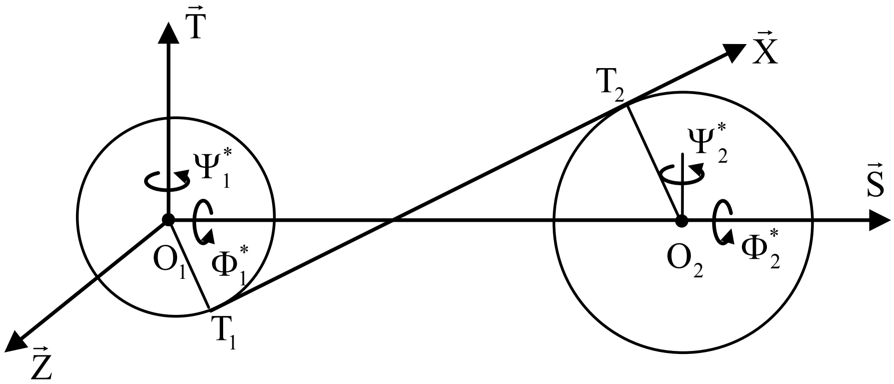

Figure 7 – External gear with misalignment errors, parameter definition for misalignment modeling

c) Eccentricity and run-out errors

Keeping a 2D representation, eccentricity corresponds to the deviation between the centre of rotation of one part and its geometrical centre. The screw formalism can be used here again and the contribution of eccentricity e_j on solid j (see Figure 8) to tooth contact can be derived by using the same shifting property [31].

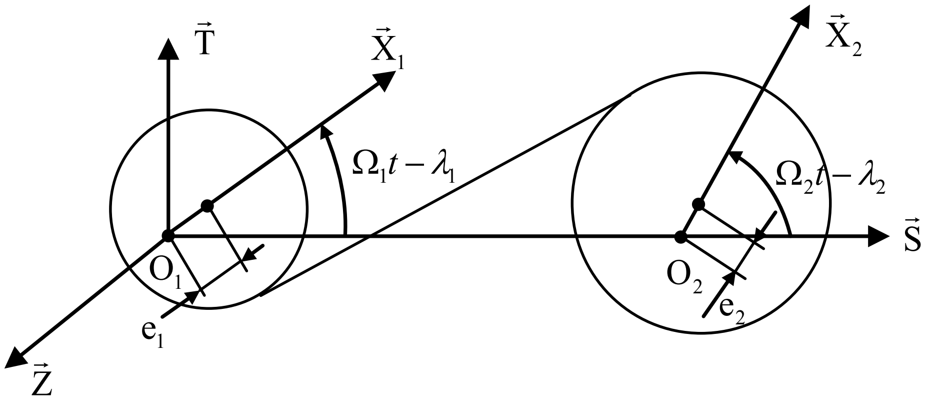

Figure 8 – External gear with eccentricity errors; parameter definition for eccentricity modelling: $G_{1,2}$ centre of inertia of pinion and wheel, respectively; $O_{1,2}$ centre of rotation of pinion and wheel, respectively.

d) *Tooth shape modifications*

As opposed to the previously described deviations, intentional profile and lead modifications are frequently used in order to improve the load distribution and dynamic properties of gears. Both profile and lead deviations can be used to compensate for elastic deflections (off-line of action contacts, misalignments, etc.) and reduce mesh excitations. Tip (or root) relief is a modifications of a tooth profile whereby a small amount of material is removed near the tip (or root) of the gear tooth as shown in Figures 9-a and 9-b. In order to prevent shocks at engagement due to tooth deflections and obtain a satisfactory tooth load distribution along the path of contact in the transverse section, profile modifications are commonly applied by slightly modifying the shape of the tooth tips and/or roots. Profile relief are characterised mainly by their amplitude or depth of modification at tooth tip or root and by their extent or length either measured along the profile or the path of motion on the base plane.

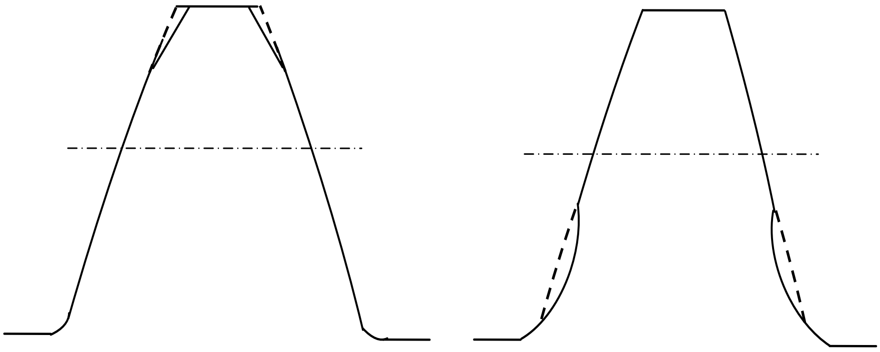

Figure 9-a – Tip relief Figure 9-b – Root relief

Figure 9 – Tip and root relief (bi-dimensional representation) [32]

Lead modifications and helix corrections (in the face width direction) are designed to compensate for the uneven deflection of the gear teeth due to load, thermal or other effects such as misalignments. Two examples of lead modifications: crowning and chamfering are shown in Figure 10.

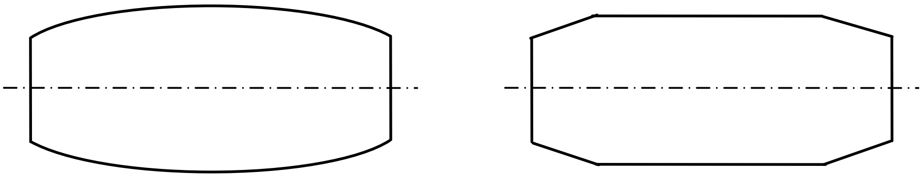

Figure 10 – Lead modifications (spur gear) [32]

2.1.4 – Total deviation

All the deviations presented above have to be superimposed in order to generate the equivalent total error at the various meshes. Bodas and Kahraman [5], [33] stated that a large number of manufacturing errors influencing planet load-sharing characteristics could be combined into a total planet error.

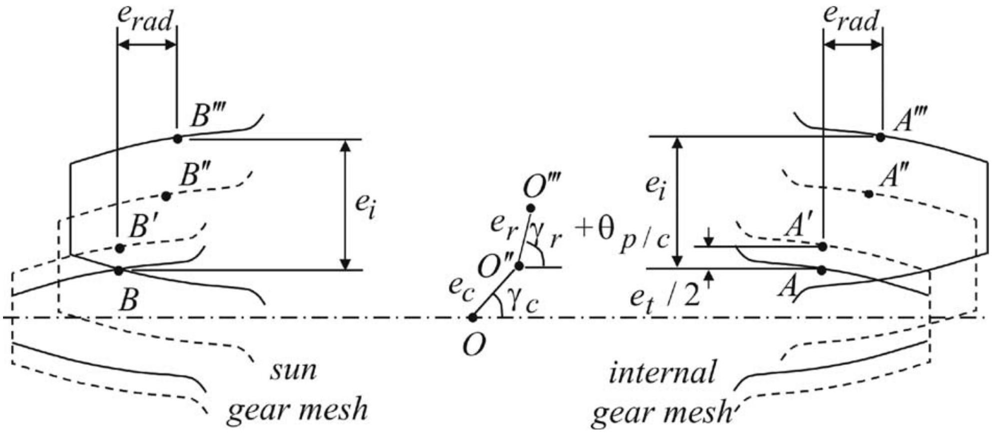

Figure 11 – A schematic showing how different types of manufacturing errors influence the position of planet tooth contact [33], carrier pin hole position error of magnitude e_c; tooth thickness error of magnitude e_t; planet run-out error of magnitude e_r

They classified these errors in three distinct groups (Figure 11):

(1) constant assembly independent errors (planet pinhole position errors, pinhole diameter errors).

(2) constant assembly dependent errors (planet tooth thickness errors, planet bore diameter errors, planet bearing needle diameter errors, and planet pin diameter errors).

(3) both rotation and assembly dependent errors (pitch line run-out errors of the sun-gear, planets, and the ring-gear).

2.1.5 – Transmission errors

The concept of transmission error (*T.E.*) was first introduced by Harris in 1958 [34] in relation to the study of the dynamic tooth forces generated in a pinion-gear pair. The author realised that for high speed applications the problem was one of continuous vibrations rather than a series of impacts as had been thought before. Harris showed that the measure of departure from perfect motion transfer between two gears (which is the definition of *T.E.*) was strongly correlated with the excitations and dynamic responses. TE is classically defined as the deviation in the position of the driven gear (for any given position of the driving gear), relative to the position that the driven gear would occupy if both gears were geometrically perfect and rigid.

No-load transmission error (NLTE) is directly related to geometrical errors and, for example, can be linked to the results of single flank gear tester. In this test, the gear is mated with a master gear on a fixed centre distance apparatus and set in such a way that only one tooth side makes contact. The gears are rotated through this single flank contact action, and the angular transmission error of the driven gear is measured.

Transmission error under load is similar to NLTE but it incorporates elastic deflections. From a practical viewpoint, one separates the quasi-static transmission error under load (TEs) and the dynamic transmission error under load (DTE). TEs is currently used as an indicator of the excitations and noise level in a transmission and, as demonstrated by Velex and Ajmi [35], it captures most of the mesh excitation for a single stage gear as long as linear behaviour prevails.

2.2 – Load sharing in planetary gears

Hidaka et al. [36-49] and Muller [40] confirmed, both experimentally and theoretically, that perfect load sharing in a three-planet gear can be achieved only if, at least, one central member (sun-gear, ring-gear or carrier) is allowed to float. Hidaka [37] analysed the relation between run-out errors and the motion of the sun-gear centre in a Stoeckicht planetary gear with several floating parts. Similar studies by other authors [41-43] emphasised the importance of the sun-gear support (piloting) conditions on planet load sharing. Kahraman et al. [5], [36], [44-46] extended the analysis to planetary gears with four and more planets. Singh [47-50] carried out several theoretical and experimental analyses on quasi-static load sharing and proposed a series analytical formulae for the prediction of planet loading in the presence of position errors. In particular, the author demonstrated through models and experiments that tangential pin-hole errors on planets are much more influential than radial pin-hole position error and that the sensitivity to position errors increases as the number of planets increases [47]. It has also been shown that floating systems experience better load sharing than non-floating systems [36-37], [47], for 3-planet systems equal load sharing under floating conditions can be obtained [36-37], [40], [51] whereas, for 4-planet systems, equal loads are found on diagonally opposed planets [47-48] .

The effects of run-out and position errors on the static and dynamic characteristics of planetary gears have been investigated by Cheon [52-53] with particular emphasis placed on the influence of bearing stiffness. Recently, Montestruc [54] has derived a closed-form formula for the load sharing ratio directly based on the design tolerance, the average deflection of one planet and the number of planets. The author also investigated the improvement on planet load sharing brought by Hicks-type flexible planet pins [55].

The flexibility of the ring-gear (rim thickness) is another key parameter which may influence noise, tooth load distributions and reliability. The rim must be as light as possible in order to increase power density and add flexibility by reducing the rim thickness. A flexible ring-gear can, to a certain extent, reduce the influence of geometry and mounting errors thus improving the load sharing between the planets [38], [40]. Abousleiman and Velex [56] proposed a hybrid model of a planetary gear set which combines a finite-element model of a ring gear and carrier with a lumped parameter model for the other components. Discrete mesh stiffness elements and equivalent normal deviations are introduced along the contact lines, and their values are updated as the mating flank positions vary with time. Kahraman et al. [46], [57-58] investigated experimentally and analytically the influence of ring-gear flexibility on the quasi-static stresses in planetary gears and confirmed that the ring-gear deflections and supporting conditions are first order parameters to be included in the design process.

2.3 – Cancellations of some excitations

In practical design, planet mesh phasing schemes can be applied to cancel or neutralize the excitations from the various meshes on the sun-gear and/or the ring-gear. Hidaka et al. [59] found that the vibrations in planetary gears can be reduced by proper gear mesh phasing. Kahraman et al. [26-27] using a 3D lumped-parameter investigated the effectiveness of vibration neutralisation by adjusted planet mesh phases and illustrated how some excitation harmonics vanish by changing mesh phasing. Using the modal properties of planetary gears, Parker [29] showed how proper mesh phasing can suppress the contributions of translational and rotational modes for certain harmonics of the mesh frequency. Along the same lines, Ambarisha and Parker [60] established formulae giving the particular contact ratios and mesh phasing that eliminate certain harmonics of planet mode response in planetary gear dynamics.

2.4 – Other critical issues in planetary gear dynamics

2.4.1 – Free vibration modal

Free vibration analyses are aimed at calculating natural frequencies and vibration modes that are key parameters in nearly every dynamic investigation. Using a 13-DOF lumped parameter model, Cunliffe et al. [61] determined the eigenvalues for an example of planetary gear. Later, Botman [62], Frater et al. [63], Antony [64] analysed the evolution of the tooth natural frequencies and vibration modes versus planet bearing stiffness and studied the effect of carrier. Saada and Velex [65] introduced an extended modular 3D model based on external, internal gear elements and studied the influence of ring gear support stiffness on the natural frequencies. Parker et al. [66] set up a 3D lumped parameter model to determine and classify the rotational-axial, translational-tilting and planet modes (Figure 12) and compared with the results from a finite element model. In the continuation of this work, the author used this discrete model to study natural frequency and mode shape sensitivity [67], the veering of natural frequencies [68], the parametric instabilities associated with elastic continuum ring gears [69], diametrically opposed planets [70], the modal properties of compound planetary gears [71].

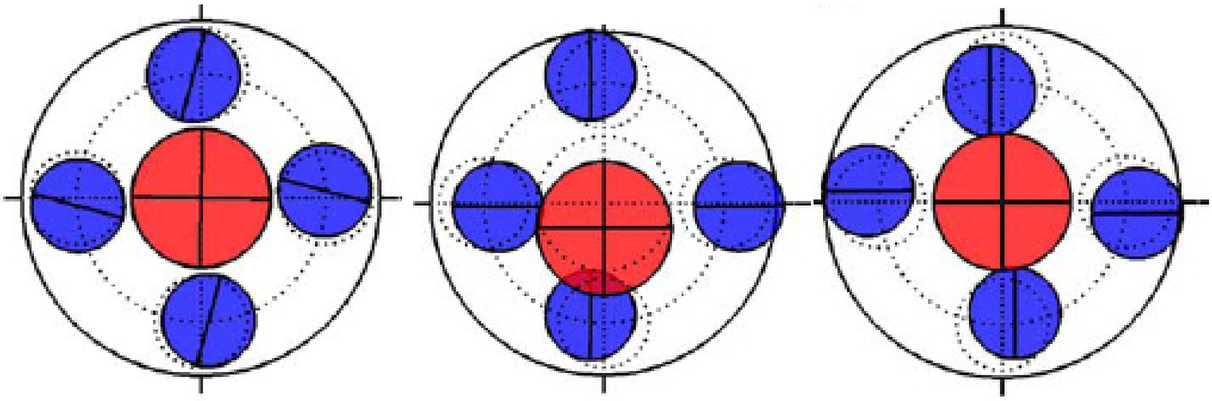

(a) (b) (c)

Figure 12 – (a) rotational–axial modes (b) translational–axial modes (c) planet modes [66]

2.4.2 – Parametric instability and non-linear behaviour

Near resonant operating conditions, gears can experience momentary tooth separations leading to non-linear effects such as jump phenomena, shocks, back strike and sub- and super-harmonic resonances. Tooth separations occur due to large relative vibrations and the presence of unavoidable backlash [72-73]. The experimental studies on the dynamic behaviour of spur gears were initiated in the Universities of Cambridge and Munich in the late 50’s and are still of the day [74-76]. Planetary gears being more complex, only a limited number of studies, mostly theoretical, can be found in the literature. Botman [62], [77] experimentally showed the presence of tooth separation in planetary gears with spur gears. Kahraman [45] included the possibility of contact losses in his model but, the back collisions of teeth were not included. Velex and Flamand [30] showed that the dynamic tooth loads can be large enough to generate tooth separations at critical speeds. More recently, Tao and HaiYan [78] investigated the non-linear frequency response of a planetary gear with multiple clearances for a fixed ring gear configuration. Using finite element and lumped parameter models, Ambarisha and Parker [79] predicted tooth contact losses leading to large mesh (Figure 13) and bearing forces [80]. Considering the torsional DOFs only, Bahk and Parker [81] derived closed-form dynamic solutions for planetary gears submitted to tooth separations. Finally, Guo and Parker [82] studied the nonlinear tooth wedging behaviour and its correlation with planet bearing forces.

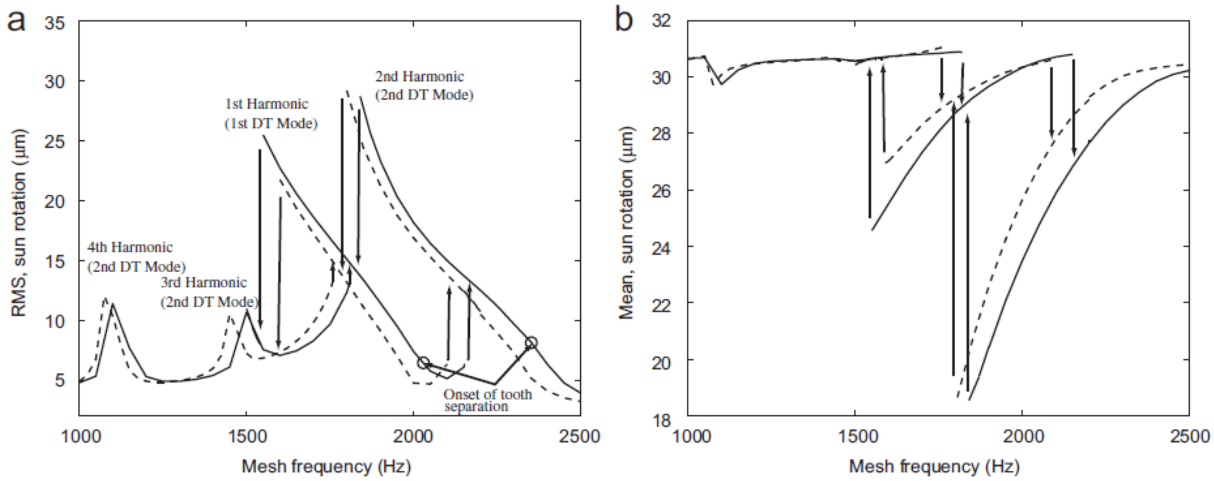

Figure 13 – Steady state (a) rms values (mean removed), and (b) mean values of sun rotation for increasing and decreasing speeds in finite element and analytical models for case 1 (note: DT Mode – distinct mode): (—) FE model and (- - -) analytical model [79]

2.5 – Current dynamic models of planetary gears

As a conclusion of this literature review, it seems interesting to synthesize the various numerical models commonly employed in the prediction of planetary gear dynamic behaviour.

Basically, three kinds of model have been used which comprise: a) lumped parameter models with a limited number of DOFs, b) hybrid models combining finite elements and lumped parameter elements and, c) larger finite element approaches which are more reliable and versatile in terms of structural components but time-consuming and not necessarily well adapted to refine tooth contact simulations.

2.5.1 – Lumped-parameter models

These models rely on the combination of lumped masses, inertias, spring elements etc. Gears are normally assimilated to rigid cylinders connected by some more or less complex arrangements of springs and dampers aimed at representing tooth/gear body flexibility and its evolutions with time or with the contact conditions (misalignments, instantaneous contact losses, etc.). The 13 DOF-model of Cunliffe et al. [61] is one of the earliest; it was developed for the analysis of the natural frequencies and modes in a single stage train with a fixed carrier. Jarchow and Vonderschmidt [83] developed a model with three planets taking into account manufacturing tooth errors and mesh stiffness variations which may cause vibrations and consequently dynamic tooth forces. A two-dimensional transverse-torsional model with constant stiffness was elaborated by Botman [62] who studied numerically the influence of the carrier rotation and planet bearing stiffness on the system natural frequencies (critical mode shapes). The particular role of axi-symmetric modes on the generation of severe vibrations was emphasized. Dynamic loads and the contributions of gear errors and misalignments were discussed later on the same kind of modeling by Botman and Ma [84]. August and Kasuba [85] built a torsional model for basic epicyclic gear systems with 2 additional transverse degrees of freedom for the sun displacements. Kahraman [86] proposed a pure torsional model, and extended it to three-dimensional PTGs to predict the natural frequencies of planetary gear trains. A similar model but restricted to the torsional degrees-of-freedom was used by the same author in order to analyse compound planetary gears typical of automotive gearboxes [87]. Parker et al. analysed the possibility to suppress instabilities [64], along with the structured vibration mode and natural frequency properties of compound planetary gears [88], the mode shape sensitivity [67], tooth contact losses and nonlinear phenomena [79]. Finally, Tao and HaiYan [78] established a two-dimensional lumped parameter model that included N+4 rotational DOFs and 2 tansverse DOFs (horizontal and vertical transverse DOFs of sun gear).

2.5.2 – Hybrid models

Kahraman et al. [33], [46] developed a sophisticated model with a combination of semi-analytical techniques, 2D finite elements, and detailed contact modelling of the tooth mesh. Recently, flexible ring gears have been introduced in both finite element and analytical models [89]. Parker et al. [70] investigated the vibration modes of planetary gears with flexible ring-gears using a hybrid continuous-discrete model. Velex et al. [56], [90] introduced an alternative modelling strategy based on a hybrid approach combining FE and lumped parameters. The parts with linear behaviour are synthesised by using a sub-structuring technique whereas the various meshes are explicitly dealt with. By so doing, the number of DOFs remains limited and a contact algorithm can be coupled with a time-step integrator for solving the instantaneous tooth load distributions.

2.5.3 – Finite Element Model

Finite element models address the shortcomings of the lumped parameter simulations since they account for many effects including gear blank deflections, support and spline conditions, mesh stiffness and stresses. However, the majority of these FE models are dedicated to static or quasi-static analyses and the computational costs are still an issue which, for instance, limit the possibility of massive parameter analyses. In real gear sets, flexible ring-gears which can hardly be accounted for by lumped parameter models, help improve the load sharing amongst the planets in the presence of manufacturing and assembly errors [36] [40]. Using a 2D finite element model, Hidaka et al. [91] calculated ring-gear deflections and showed their significant influence on tooth loads and load sharing properties. In a series of papers, Singh [47], Kahraman et al. [33] [46], Parker et al. [89] conducted a number of 3D static calculations and experiments on a fully instrumented test rig. The authors stressed the significant effect of internal gear flexibility and planet position errors on load sharing by the different meshes. Later, a more sophisticated three-dimensional 3D version of this PTG model had been used [48] exhibiting very good correlations with the measured strains on the ring-gear. Other FE models have been presented which, not only simulate accurately rim deflections and spline support conditions, but also include the bi-dimensional dynamic analysis of tooth profile variations under the form of intentional profile modifications, manufacturing errors [58] or wear [92]. Wu and Parker [89] developed a model that includes planetary gear discrete degrees of freedom (rotational and translational) along with ring gear elastic deflections. Parker et al. [93-94] adopted a unique finite element FE/contact analysis method. Helsen [95-97] focused on the gear box modal behaviour assessment of a generic gearbox consisting of one planetary and two helical gear stages by means of three modelling techniques of increasing complexity: a purely torsional multibody models a six degrees of freedom rigid multi-body model with discrete flexibility and a flexible multi-body technique.

3 – Research objectives and thesis outline

Based on the review above, it appears that, in spite of a vast number of contributions in the literature, the dynamic simulation of PTGs remains topical. Among the research fields which still merit further investigation, the combined influence of flexible fixtures and errors on mesh geometry for dynamic regimes has received very little attention. In this context, significant errors along with quasi-static and/or dynamic displacements can alter the positions of the pinions/gears thus changing the orientations of the planes of action (mesh forces) and the parametric excitations associated with the contact length evolutions between the mating tooth flanks. As far as the author knows, the problem has only been tackled in a recent article [98] with no full coupling between the system degrees-of-freedom and geometry.

In chapter 2, an original lumped parameter PTG model is presented which makes it possible to capture the quasi-static and dynamic load sharing characteristics in planetary gears with fixed and rotating carriers. Planet position errors are considered and the influence of deflections on instantaneous gear mesh properties is incorporated leading to amplitude, frequency and phase modulated mesh stiffness functions depending on the errors. The resulting state equations point to a non-linear parametrically excited differential system which is solved iteratively by combining a time-step integration scheme, a fixed-point method and a normal contact algorithm. In view of the variety of the dynamic interactions taken into consideration, a compromise had to be reached in terms of the number of DOFs or equations and modelling strategies (lumped parameter model as opposed to finite element models for instance). It is believed that the proposed approach is balanced in that respect and that it can simulate actual dynamic loads in PTGs as illustrated in chapter 3 which displays a number of comparisons with benchmark results from the literature. Finally, extensive numerical simulations are presented in chapter 4 in order to characterize the role of i) planet position errors and ii) eccentricities for either rigid or flexible mounts and assess some commonly employed design rules.

CHAPTER II

DYNAMIC MODEL OF PLANETARY GEARS

1 – Introduction

In planetary gears under ideal conditions, each path carries an equal amount of load but, because of geometrical errors due to the manufacturing quality and the assembly precision, the situation can be dramatically different and give rise to severe overloads on some meshes. Errors such as flank deviations, pin-hole and position errors, eccentricities, thickness errors, etc. may lead to contact losses, partial contacts and introduce additional dynamic excitations in the system. Based on the literature review in chapter 1, planet pin-hole errors and eccentricities (also leading to so-called run out errors) can be considered as some of the most influential parameters on planet load sharing. In this chapter, the theoretical bases for simulating these two kinds of defects are presented and an original PTG dynamic model is derived. In what follows, the state of reference corresponds to rigid-body motions in the presence of errors whereas the degrees-of-freedom are defined as small generalised displacements superimposed on large rigid-body rotations.

Because of the redundant paths for the motion transfer from the input (sun-gear in this memoir) to the output (carrier or ring-gear), contacts in rigid-body conditions can be lost between parts normally in contact for errorless gears. In the model, every planet is attributed an additional rigid-body angle about its pin axis in order to satisfy the following functional requirements (for rigid-body conditions): a) all the planets are in contact with the sun-gear and b) there is, at least, one contact between a planet and the ring-gear in order to close the kinematic chain. The mathematical solution leads to a) the definition of the additional planet rotational angles giving rise to rigid-body angular speeds and accelerations and b) some possible separations (gaps) between the planet and ring-gear teeth where contacts cannot be re-established by planet rigid-body rotations only. Using the rigid-body contact constraints on the base planes and the initial separations between the planets and the ring-gear, the rigid-body angular velocities and accelerations of the sun-gear, ring-gear, carrier, planets are deduced.

An original model simulating the instantaneous mesh stiffness functions (IMSF) is presented which includes the influence of deflections, eccentricities and position errors. The corresponding mesh parametric excitations are controlled by a) the evolutions of the contact length during rotation (which exist even for errorless rigid gears) possibly altered by eccentricity and position errors and, b) the variations in centre-distance, pressure angle, etc.

caused by deflections and errors. Moreover, tooth contacts can also generate strong non-linear phenomena with contact losses leading to a mesh stiffness which momentarily drops to zero and shocks when contacts are re-established (backlash). Finally, complex modulations of the instantaneous contact length evolutions and consequently the mesh stiffness functions can also take place because of unsteady rotational speeds.

An important task is the development of the dynamic PGT model so that it is possible to continuously track the individual gear components and derive the forcing functions, i.e., driving torque, and the load. An accurate determination of the positions of the component members is critical since the mesh stiffness is considered as a function of gear displacements. The model should also take into consideration: a) the possibility of mounting floating or rigid fixtures; b) rotating or stationary carriers, i.e., account for gyroscopic and centrifugal effects or not. Finally, the model should lend itself to easy parameter analyses in order to assess several design solutions: floating versus rigid members, bearing stiffness, etc. on dynamic tooth load distributions, trajectories, vibrations, etc.

2 – Gear member definitions with planet position errors and eccentricities

In planetary gear systems, errors in the positions of the planet centres are due to manufacturing tolerances and, in particular, those associated with the location of the planet pinholes on the carrier. Such errors have been recognised as particularly influential on planet load sharing and consequently on the system reliability. Eccentricity error (also related to run-out error and imbalance) corresponds to a centre of rotation which does not coincide with the geometric centre of the gear.

In the presence of such errors, contacts for rigid-body conditions can be lost or interrupted between parts normally connected for errorless conditions. Considering the situation at one given time t, the deviations with respect to errorless conditions can be simulated via screws of infinitesimal generalised displacements attributed to every solid. The translation vector (screw moment) simulates the eccentricity and position errors (restricted here to planet position errors) and one additional infinitesimal rigid-body rotational angle (sum of the wrench) is introduced on the driven members to ensure that, at least, one transmission path is continuous between the input and the output. In what follows, it will be supposed that the sun-gear is the driving member and that its rigid-body angular speed is constant (its additional angle ϕ_S is therefore nil). Similarly, the angle ϕ_k associated with the reaction member, either the ring-gear or the carrier, will be set to zero (fixed member).

The modelling principle is illustrated in the case of eccentricity alone on the central members (i.e., the sun-gear, ring-gear and carrier) as shown in Figure 1. In this case, the screw coordinates are:

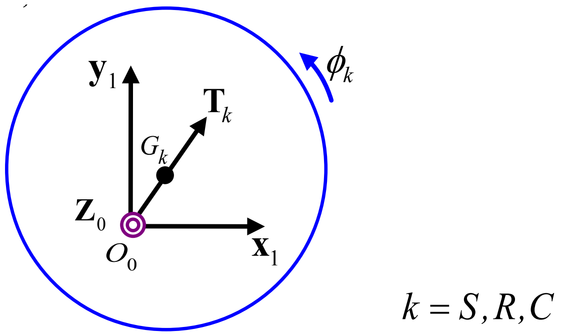

Figure 1 – Model definition for sun-gear, ring-gear and carrier

$$\left\{S_k^{\Re}\right\}\begin{cases}\mathbf{u}_k^{\Re}\left(G_k\right)=\mathbf{O}_0\mathbf{G}_k=e_k\,\mathbf{T}_k\\ \boldsymbol{\omega}_k^{\Re}=\phi_k\,\mathbf{z}_{0,k}\end{cases}\tag{1}$$

where:

superscript $\Re$ indicates that the perturbations are measured from the errorless configuration of solid k.

e_k is the eccentricity error in the direction of $\mathbf{T}_k$

ϕ_k is the additional rotational angle of possibly induced by errors.

Considering the case of N equally spaced planets, their positions on the carrier are characterised by using the spacing angles $\Phi_j = 2\pi(n-1)/N, n=1,2,3...$ where index j refers to planet #j. Position errors are usually separated into a) radial position errors e_{xj} in the $\mathbf{x}_j$ direction and, b) tangential position errors e_{yj} in the $\mathbf{y}_j$ direction as represented in Figure 2.

As for central members, the screw formalism is employed leading to:

$$\left\{S_j^{C}\right\}\begin{cases}\mathbf{u}_j^{C}\left(G_j\right)=\mathbf{O}_{pj}\mathbf{O}_{j0}+\mathbf{O}_{j0}\mathbf{G}_j=e_{xj}\mathbf{x}_j+e_{yj}\mathbf{y}_j+e_j\mathbf{T}_j\\ \boldsymbol{\omega}_j^{C}=\varphi_j\,\mathbf{z}_j\end{cases}\tag{2}$$

where:

e_j represents the eccentricity error in the direction of $\mathbf{T}_j$

φ_j is the additional rotational angle of planet #j possibly induced by errors

e_{xj} and e_{yj} are the radial and tangential position errors

superscript C refers to the carrier frame from which all the errors are measured/defined

In these conditions, the total perturbations from errorless conditions result of the combination of the carrier errors plus those of planet #j which gives:

$$\left\{S_j^{\Re}\right\} = \left\{S_j^{C}\right\} + \left\{S_C^{\Re}\right\} \tag{3}$$

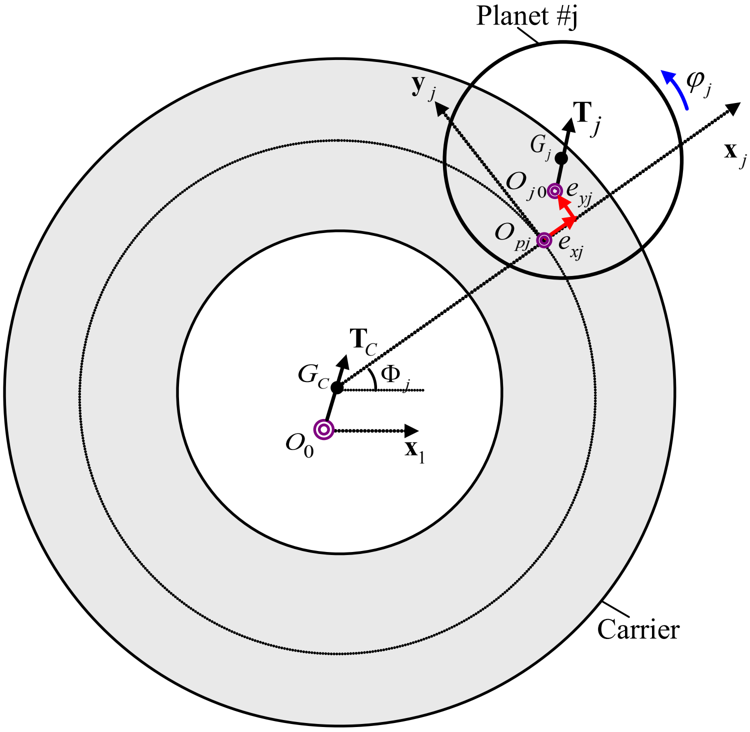

Figure 2 – Definition of planet #j frame

3 – Rigid-body contact constraints on mesh planes

In the analysis of the motion transfer in Figure 3, it is assumed that there is always contact at all the sun-gear / planet interfaces regardless of the errors. This implies that there is always a combination of additional small rigid-body angles on the carrier (ϕ_C) and the planets (φ_j) such that contacts can be re-established on the sun-gear/planet base planes. The corresponding conditions can be formulated as:

$$\mathbf{u}_S^j(M_{Sj}) \cdot \mathbf{n}_j = 0 \tag{4}$$

$$
\begin{aligned}
\mathbf{u}_S^j(M_{Sj})\cdot\mathbf{n}_j &= \left(\mathbf{u}_S^{\Re}\left(M_{Sj}\right)-\mathbf{u}_j^{\Re}\left(M_{Sj}\right)\right)\cdot\mathbf{n}_j \\
&= \left(\mathbf{u}_S^{\Re}\left(M_{Sj}\right)-\mathbf{u}_C^{\Re}\left(M_{Sj}\right)-\mathbf{u}_j^{C}\left(M_{Sj}\right)\right)\cdot\mathbf{n}_j \\
&= \left(\mathbf{u}_S^{\Re}\left(G_S\right)-\zeta\mathbf{u}_C^{\Re}\left(G_C\right)-\zeta\phi_C\ \mathbf{z}_{0,j}\times\mathbf{G}_C\mathbf{M}_{Sj}-\mathbf{u}_j^{C}\left(G_j\right)-\varphi_j\ \mathbf{z}_{0,j}\times\mathbf{G}_j\mathbf{M}_{Sj}\right)\cdot\mathbf{n}_j \\
&= \left(\mathbf{u}_S^{\Re}\left(G_S\right)-\zeta\mathbf{u}_C^{\Re}\left(G_C\right)-\zeta\phi_C\ \mathbf{z}_{0,j}\times\mathbf{G}_C\mathbf{G}_j-\mathbf{u}_j^{C}\left(G_j\right)-(\varphi_j+\zeta\phi_C)\mathbf{z}_{0,j}\times\mathbf{G}_j\mathbf{M}_{Sj}\right)\cdot\mathbf{n}_j
\end{aligned}
$$

with:

$\mathbf{n}_j$, an unit normal vector at the point of contact M_{Sj} on the sun-gear / planet #j base plane (Figure 4).

$\zeta=1$ if the ring-gear is fixed and $\zeta=0$ if the carrier is fixed.

Noting that a vector is represented by a symbol in bold which can be one bold character or a combination of two bold characters (if the two characters are unbold, each of them represents a geometrical point).

Solving for $\varphi_{\mathrm{j}}+\zeta\phi_{\mathrm{C}}$, the following expression is obtained from (4)

$$
\phi_j+\zeta\phi_C=\frac{\left(\mathbf{u}_S^{\Re}\left(G_S\right)-\zeta\mathbf{u}_C^{\Re}\left(G_C\right)-\zeta\phi_C\ \mathbf{z}_{0,j}\times\mathbf{G}_C\mathbf{G}_j-\mathbf{u}_j^{C}\left(G_j\right)\right)\cdot\mathbf{n}_j}{\left(\mathbf{z}_{0,j}\times\mathbf{G}_j\mathbf{M}_{Sj}\right)\cdot\mathbf{n}_j} \tag{5}
$$

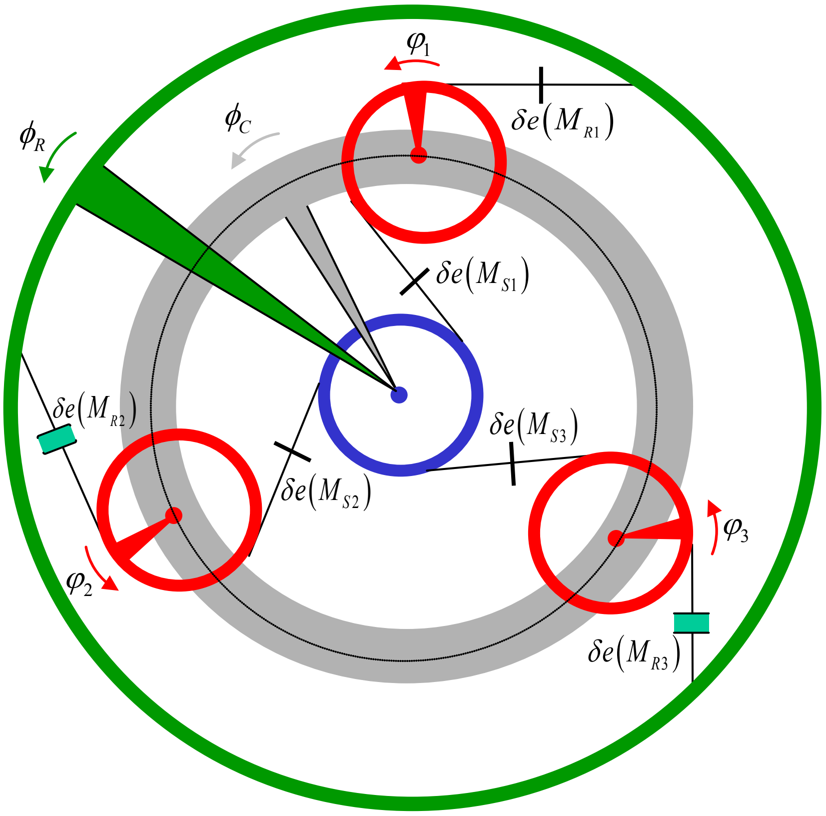

Initial separation error: — $\delta e\left(M_{Sj/Rj}\right)=0$; 🟩 $\delta e\left(M_{Sj/Rj}\right)\neq 0$

Figure 3 – Rigid-body contact constraints on mesh planes-Schematic representation

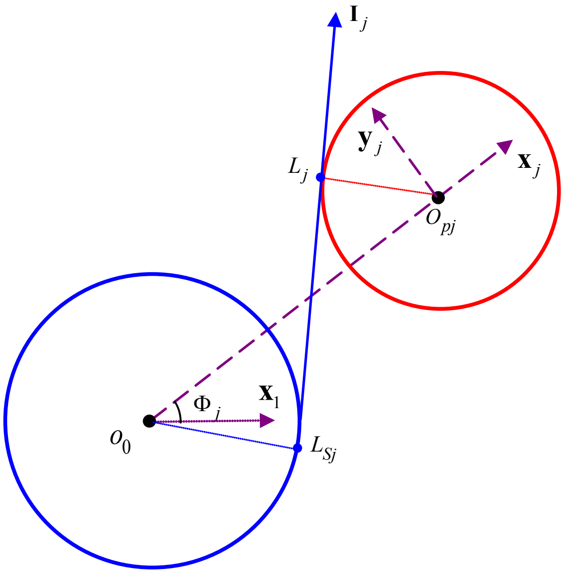

Figure 4-a – Parameters for sun-gear/planet #j mesh

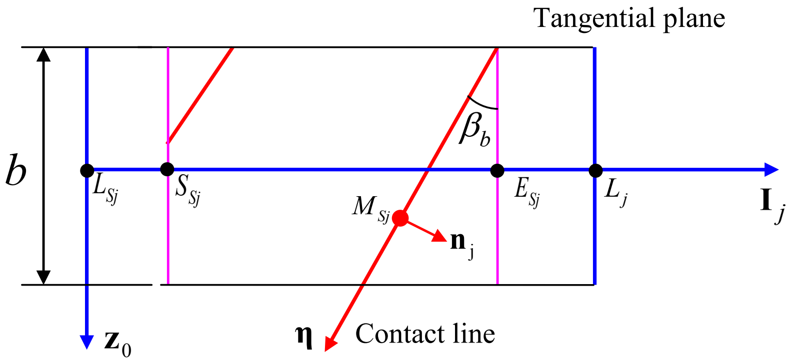

Figure 4-b – Parameters for sun-gear/planet #j mesh plane

Turning to the planet / ring-gear interfaces in Figure 3, two configurations must be distinguished depending if the ring-gear or the carrier are fixed. However, the solution technique is similar and consists in finding the base plane(s) with the minimum initial separation (separations between planets and ring-gear can occur) because of the additional angles (φ_j) required to ensure contacts at the sun-gear / planet meshes and determine the additional angle either on the ring-gear (ϕ_R) or the carrier (ϕ_C) to re-establish contact, at least, at one planet / ring-gear mesh to ensure the kinematic chain continuity from the input to the output member. The separation at point M_{Rj} can be formally expressed as:

$$\delta\left(M_{Rj}\right)=\mathbf{u}_R^j\left(M_{Rj}\right)\cdot\mathbf{n}_j^* \qquad (6\text{-a})$$

which is developed as:

$$\begin{aligned}
\mathbf{u}_R^j\left(M_{Rj}\right)\cdot\mathbf{n}_j^{\,*} &= \left(\mathbf{u}_R^{\Re}\left(M_{Rj}\right)-\mathbf{u}_j^{\Re}\left(M_{Rj}\right)\right)\cdot\mathbf{n}_j^{\,*} \\
&= \left(\mathbf{u}_R^{\Re}\left(M_{Rj}\right)-\mathbf{u}_C^{\Re}\left(M_{Rj}\right)-\mathbf{u}_j^{C}\left(M_{Rj}\right)\right)\cdot\mathbf{n}_j^{\,*} \\
&= \left(\mathbf{u}_R^{\Re}\left(G_R\right)+\left(1-\zeta\right)\phi_R\ \mathbf{z}_{0,j}\times\mathbf{G}_r\mathbf{M}_{Rj}-\mathbf{u}_C^{\Re}\left(G_C\right)-\zeta\phi_C\ \mathbf{z}_{0,j}\times\mathbf{G}_C\mathbf{M}_{Rj}-\mathbf{u}_j^{C}\left(G_j\right)-\phi_j\ \mathbf{z}_{0,j}\times\mathbf{G}_j\mathbf{M}_{Rj}\right)\cdot\mathbf{n}_j^{\,*} \\
&= \left(\mathbf{u}_R^{\Re}\left(G_R\right)+\left(1-\zeta\right)\phi_R\ \mathbf{z}_{0,j}\times\mathbf{G}_r\mathbf{M}_{Rj}-\mathbf{u}_C^{\Re}\left(G_C\right)-\zeta\phi_C\ \mathbf{z}_{0,j}\times\mathbf{G}_C\mathbf{G}_j-\mathbf{u}_j^{C}\left(G_j\right)-\left(\phi_j+\zeta\phi_C\right)\mathbf{z}_{0,j}\times\mathbf{G}_j\mathbf{M}_{Rj}\right)\cdot\mathbf{n}_j^{\,*}
\end{aligned} \tag{6-b}$$

where:

* stands for vectors associated with planet / ring-gear meshes.

$\mathbf{n}_j^{\,*}$ is a unit normal vector at the point of contact M_{Rj} on the planet #j / ring-gear base plane (Figure 5).

The various vector products give:

$$\left(\mathbf{z}_{0,j}\times\mathbf{G}_j\mathbf{M}_{Sj}\right).\mathbf{n}_j=\left(\mathbf{z}_{0,j}\times\mathbf{G}_j\mathbf{M}_{Rj}\right).\mathbf{n}_j^*=-\varepsilon_s Rb_j\cos\beta_b \tag{6-c}$$

$$\left(\mathbf{z}_{0,j}\times\mathbf{G}_C\mathbf{G}_j\right).\mathbf{n}_j=\varepsilon_s R_C\cos\beta_b\cos\alpha_{Sj} \tag{6-d}$$

$$\left(\mathbf{z}_{0,j}\times\mathbf{G}_C\mathbf{G}_j\right).\mathbf{n}_j^*=-\varepsilon_s R_C\cos\beta_b\cos\alpha_{Rj} \tag{6-e}$$

$$\left(\mathbf{z}_{0,j}\times\mathbf{G}_R\mathbf{M}_{Rj}\right).\mathbf{n}_j^*=-\varepsilon_s Rb_R\cos\beta_b \tag{6-f}$$

Introducing (5), one obtains:

$$\delta(M_{Rj})=U_j^*+\left(\left(1-\zeta\right)\phi_R\ \mathbf{z}_{0,j}\times\mathbf{G}_R\mathbf{M}_{Rj}-\zeta\phi_C\ \mathbf{z}_{0,j}\times\mathbf{G}_C\mathbf{G}_j\right)\cdot\mathbf{n}_j^{\,*}+\left(\zeta\phi_C\mathbf{z}_{0,j}\times\mathbf{G}_C\mathbf{G}_j\right)\cdot\mathbf{n}_j \tag{7}$$

with:

$$\begin{aligned}
U_j^* &= \left(\mathbf{u}_R^{\Re}\left(M_{Rj}\right)-\mathbf{u}_C^{\Re}\left(G_C\right)-\mathbf{u}_j^{C}\left(G_j\right)\right)\cdot\mathbf{n}_j^{\,*}-\left(\mathbf{u}_S^{\Re}\left(G_S\right)-\mathbf{u}_C^{\Re}\left(G_C\right)-\mathbf{u}_j^{C}\left(G_j\right)\right)\cdot\mathbf{n}_j \\
&= \left(e_R\mathbf{T}_R-e_C\mathbf{T}_C-e_j\mathbf{T}_j-e_{xj}\mathbf{x}_j-e_{yj}\mathbf{y}_j\right)\cdot\mathbf{n}_j^{\,*}-\left(e_S\mathbf{T}_S-e_C\mathbf{T}_C-e_j\mathbf{T}_j-e_{xj}\mathbf{x}_j-e_{yj}\mathbf{y}_j\right)\cdot\mathbf{n}_j \\
&\cong \varepsilon_s\cos\beta_b\left\{e_R\sin\sigma_R-e_S\sin\sigma_S-e_C\left(\sin\sigma_C^*-\sin\sigma_C\right)-e_j\left(\sin\sigma_j^*-\sin\sigma_j\right)-e_{xj}\left(\sin\alpha_{Rj}-\sin\alpha_{Sj}\right)+\varepsilon_s e_{yj}\left(\cos\alpha_{Rj}+\cos\alpha_{Sj}\right)\right\}
\end{aligned} \tag{8}$$

with:

$\sigma_{\mathrm{S}}=\alpha_{Sj}-\varepsilon_S\Phi_j+\varepsilon_S\psi_S$; $\sigma_{\mathrm{C}}=\alpha_{Sj}-\varepsilon_S\Phi_j+\varepsilon_S\lambda_C$; $\sigma_{\mathrm{j}}=\alpha_{Sj}+\varepsilon_S\psi_j$;

$\sigma_{\mathrm{R}}=\alpha_{Rj}+\varepsilon_S\Phi_j-\varepsilon_S\psi_R$; $\sigma_{\mathrm{C}}^*=\alpha_{Rj}+\varepsilon_S\Phi_j-\varepsilon_S\lambda_C$; $\sigma_{\mathrm{j}}^*=\alpha_{Rj}-\varepsilon_S\psi_j$;

$\psi_i=\Omega_{i0}t+\lambda_i$: rotational angle without error relative to rotating carrier frame, (*i* = s, r, j).

NB: In equation (8), second-order terms of the form $\left(e_i / Rb_i\right)^2$ have been discarded.

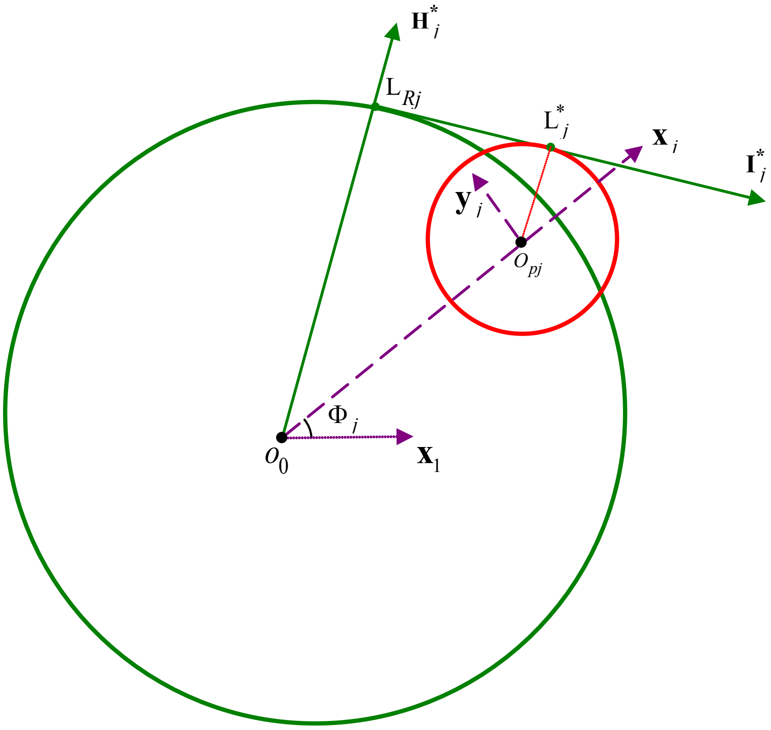

Figure 5-a – Parameters for planet #j/ring-gear mesh

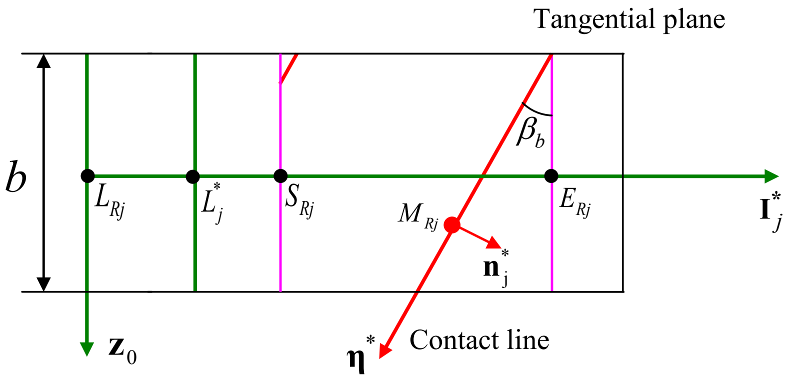

Figure 5-b – Parameters for planet #j/ring-gear mesh plane

In a frame rotating with angular speed Ω_C^0, the classic results for errorless parts read:

a) For a fixed carrier ($\zeta = 0$) $\quad \Omega_{S0} = \Omega_S^0$; $\Omega_{j0} = -\dfrac{Rb_R}{Rb_j}\Omega_S^0$; $\Omega_{R0} = -\dfrac{Rb_S}{Rb_R}\Omega_s^0$

b) For a fixed ring-gear ($\zeta = 1$) $\quad \Omega_{S0} = \dfrac{Rb_R}{Rb_S + Rb_R}\Omega_S^0$; $\Omega_{j0} = -\dfrac{Rb_R \cdot Rb_S}{Rb_j\left(Rb_S + Rb_R\right)}\Omega_S^0$

$$\Omega_{R0} = -\frac{Rb_S}{Rb_S + Rb_R}\Omega_S^0$$

It can be noticed:

a) that $\delta(M_{Rj})$ is positive or nil if $\mathbf{n}_j^*$ is the outer unit normal vector with respect to the planet tooth flanks since the condition $\delta(M_{Rj})<0$ would correspond to the interpenetration of the parts.

and b) that, for one given base plane or mesh, $\delta(M_{Rj})$ is independent of the position of the point of contact M_{Rj}.

The necessary additional angle on the carrier or the ring-gear to ensure contact at one ring-gear/planet mesh, at least , is determined by considering the minimum of U_j^* at any given time t:

$$\min\left(U_j^*\right)+\phi_R\ \mathbf{z}_{0,j}\times\mathbf{G}_R\mathbf{M}_{Rj}.\mathbf{n}_j^*=0 \qquad \text{if} \quad \zeta=0 \ : \text{a fixed carrier}$$

$$\min\left(U_j^*\right)-\phi_C\ \mathbf{z}_{0,j}\times\mathbf{G}_C\mathbf{G}_j\cdot\mathbf{n}_j^{*}+\phi_C\ \mathbf{z}_{0,j}\times\mathbf{G}_C\mathbf{G}_j\cdot\mathbf{n}_j=0 \qquad \text{if} \quad \zeta=1 \ : \text{a fixed ring-gear} \tag{9}$$

thus leading to the following additional angle on the ring-gear ϕ_R or on the carrier ϕ_C as:

$$\phi_R=\min\left(U_j^*\right)/\left(\varepsilon_S Rb_R\cos\beta_b\right) \qquad \text{if} \quad \zeta=0$$

or

$$\phi_C=-\min\left(U_j^*\right)/\left(\varepsilon_S R_C\cos\beta_b\left(\cos\alpha_{Rj}+\cos\alpha_{Sj}\right)\right) \qquad \text{if} \quad \zeta=1 \tag{10}$$

Finally, the initial normal separations are given by:

$$\delta e(M_{Sj})=0 \qquad \text{for sun-gear / planet mesh}$$

$$\delta e(M_{Rj})=U_j^*-\min\left(U_j^*\right) \qquad \text{for planet / ring-gear mesh} \tag{11}$$

Figure 6 shows an example of the initial separations of planet / ring-gear mesh $\delta e(M_{Rj})$ versus time for a 4-planet gear set with an eccentricity error of $e_S=2\cdot10^{-5}m$ on the sun-gear, position errors of $e_{x1}=1\cdot10^{-5}m$ (radial direction) and $e_{y1}=3\cdot10^{-5}m$ (tangential direction) on planet #1.

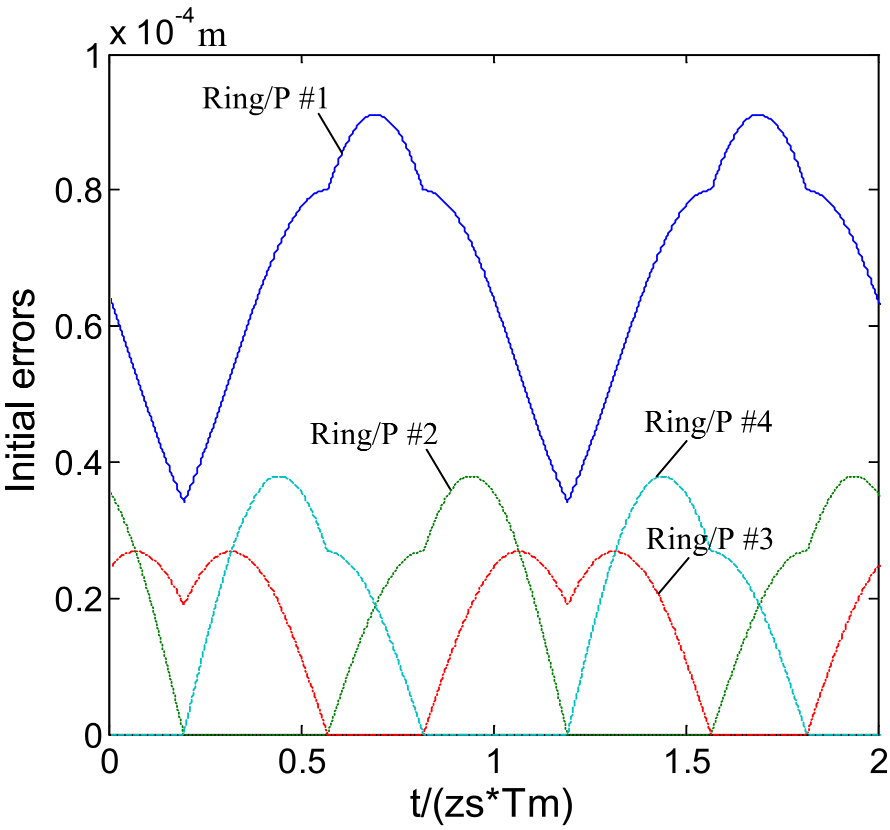

Figure 6 – Initial separations of ring-gear/ planet mesh $\delta e\left(M_{Rj}\right)$ versus time

A 4-planet gear set with an eccentricity error of $e_S = 2\cdot 10^{-5}m$ on the sun-gear, position errors of $e_{x1} = 1\cdot 10^{-5}m$ (radial direction) and $e_{y1} = 3\cdot 10^{-5}m$ (tangential direction) on planet #1.

4 – Rigid-body kinematics

With M_{Sj} and M_{Rj} denoting points of contact between the sun-gear/planet #j and the ring-gear / planet #j respectively, the fundamental property of rigid-body kinematics imposes that, at every non-singular point of contact, the relative sliding velocity should be in the tangent plane, i.e.

a) for sun-gear / planet:

$$\mathbf{V}_S^j\left(M_{Sj}\right)\cdot\mathbf{n}_j = 0 \qquad (12)$$

re-written as:

$$\mathbf{V}_S^j\left(M_{Sj}\right)\cdot\mathbf{n}_j=\left(\mathbf{V}_S^{\Im}\left(O_0\right)+\boldsymbol{\Omega}_S^{\Im}\times\mathbf{O}_0\mathbf{M}_{Sj}-\boldsymbol{\Omega}_j^{\Im}\times\mathbf{O}_j\mathbf{M}_{Sj}\right)\cdot\mathbf{n}_j=0$$
$$=\varepsilon_S\cos\beta_b\left(\Omega_S^{\Im}\left(e_S\cos\sigma_S+Rb_S\right)-\Omega_j^{\Im}\left(e_j\cos\sigma_j-Rb_j\right)\right)=0$$

b) for ring-gear / planet:

The initial normal separations $\delta e\left(M_{Rj}\right)=U_j^*-\min\left(U_j^*\right)$ at the ring-gear / planet meshes have been determined under the condition that, at least, there is contact between one particular planet labelled planet j' and the ring-gear which imposes the condition:

$$\mathbf{V}_R^{j'}\left(M_{Rj}\right)\cdot\mathbf{n}_{j'}^*=0 \tag{13}$$

developed as:

$$\mathbf{V}_R^{j'}\left(M_{Rj}\right)\cdot\mathbf{n}_{j'}^*=\left(\mathbf{V}_R^{\Im}\left(O_0\right)+\boldsymbol{\Omega}_R^{\Im}\times\mathbf{O}_0\mathbf{M}_{Rj}-\boldsymbol{\Omega}_{j'}^{\Im}\times\mathbf{O}_{j'}\mathbf{M}_{Rj}\right)\cdot\mathbf{n}_{j'}^*=0$$
$$=\varepsilon_S\cos\beta_b\left(\Omega_R^{\Im}\left(-e_R\cos\sigma_R-Rb_R\right)-\Omega_{j'}^{\Im}\left(-e_{j'}\cos\sigma_{j'}^*-Rb_j\right)\right)=0$$

The rigid-body angular velocities and accelerations for all the PTG members can be deduced from (12) and (13) and, after neglecting second-order terms of the form $\left(e_i/Rb_i\right)^2$, lead to the following expressions:

i) For the carrier:

* Angular velocity and acceleration with respect to inertial frame:

– With fixed carrier: $\zeta=0$

$$\Omega_C^0=0\ ;\dot{\Omega}_C^0=0 \tag{14}$$

– With fixed ring-gear: $\zeta=1$

$$\Omega_C^0=\Omega_S^0\left(\frac{Rb_S}{Rb_S+Rb_R}+\frac{Rb_S\cdot Rb_R}{\left(Rb_S+Rb_R\right)^2}\left(\frac{e_S}{Rb_S}\cos\sigma_S+\frac{e_{j'}}{Rb_{j'}}\left(\cos\sigma_{j'}+\cos\sigma_{j'}^*\right)-\frac{e_R}{Rb_R}\cos\sigma_R\right)\right)$$

$$\dot{\Omega}_C^0=\Omega_S^0\frac{Rb_S\cdot Rb_R}{\left(Rb_S+Rb_R\right)^2}\left(-\varepsilon_S\Omega_{S0}\frac{e_S}{Rb_S}\sin\sigma_S+\varepsilon_S\Omega_{j0}\frac{e_{j'}}{Rb_{j'}}\left(-\sin\sigma_{j'}+\sin\sigma_{j'}^*\right)-\varepsilon_S\Omega_{R0}\frac{e_R}{Rb_R}\sin\sigma_R\right) \tag{15}$$

*Angular velocity and acceleration with respect to reference frame '$\Im$':

$$\Omega_C^{\Im}=0\ ;\ \dot{\Omega}_C^{\Im}=0 \tag{16}$$

ii) For the sun-gear:

$$\Omega_S^{\Im}=\Omega_S^0-\Omega_C^0\ ;\ \dot{\Omega}_S^{\Im}=-\dot{\Omega}_C^0 \tag{17}$$

iii) For planet #*j*:

$$\Omega_j^{\Im}=-\Omega_S^{\Im}\frac{Rb_S}{Rb_j}\left\{1+\frac{e_S}{Rb_S}\cos\sigma_S+\frac{e_j}{Rb_j}\cos\sigma_j\right\}$$

$$\dot{\Omega}_j^{\Im}=-\dot{\Omega}_S^{\Im}\frac{Rb_S}{Rb_j}-\Omega_{S0}\frac{Rb_S}{Rb_j}\left\{-\varepsilon_S\Omega_{S0}\frac{e_S}{Rb_S}\sin\sigma_S-\varepsilon_S\Omega_{j0}\frac{e_j}{Rb_j}\sin\sigma_j\right\} \tag{18}$$

iv) For ring-gear:

– With fixed carrier: $\zeta=0$

$$\Omega_R^{\Im}=-\Omega_S^{\Im}\frac{Rb_S}{Rb_R}\left\{1+\frac{e_S}{Rb_S}\cos\sigma_S+\frac{e_{j'}}{Rb_{j'}}\left(\cos\sigma_{j'}+\cos\sigma_{j'}{}^{*}\right)-\frac{e_R}{Rb_R}\cos\sigma_R\right\}$$

$$\dot{\Omega}_R^{\Im}=-\dot{\Omega}_S^{\Im}\frac{Rb_S}{Rb_R}-\Omega_{S0}\frac{Rb_S}{Rb_R}\left\{-\varepsilon_S\Omega_{S0}\frac{e_s}{Rb_S}\sin\sigma_S+\varepsilon_S\Omega_{j0}\frac{e_{j'}}{Rb_j}\left(-\sin\sigma_{j'}+\sin\sigma_{j'}^{*}\right)-\varepsilon_S\Omega_{R0}\frac{e_R}{Rb_R}\sin\sigma_R\right\} \tag{19}$$

Using the same conditions as for Figure 6, the results in Figure 7 show, for a rotating gear, the time variations of the ring-gear relative angular speed; some sudden variations are observed when the contact moves from one mesh to another.

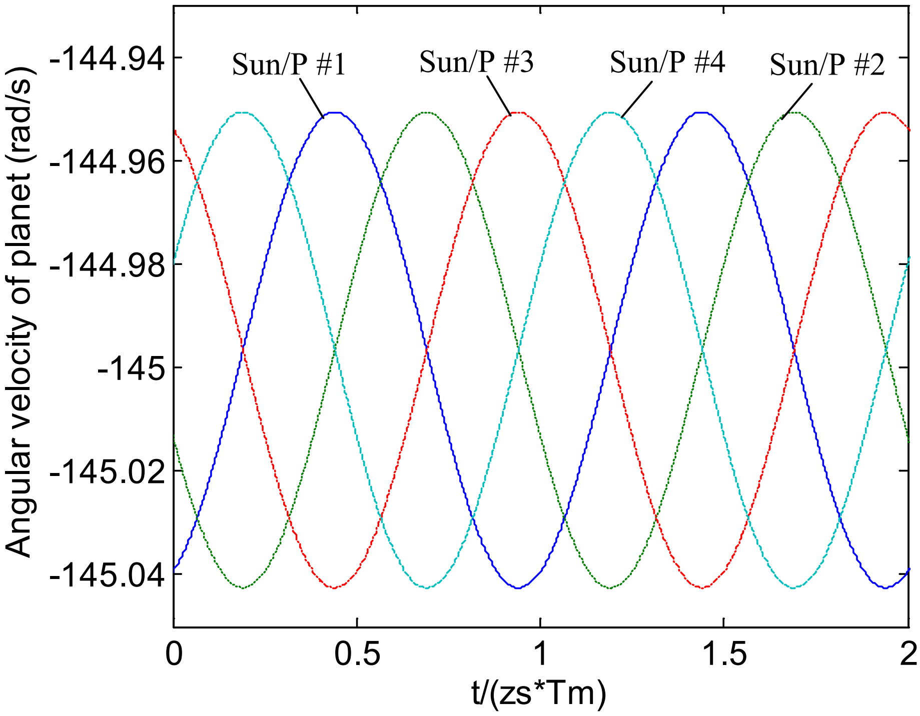

Figure 7-a – Angular velocity of planets versus time

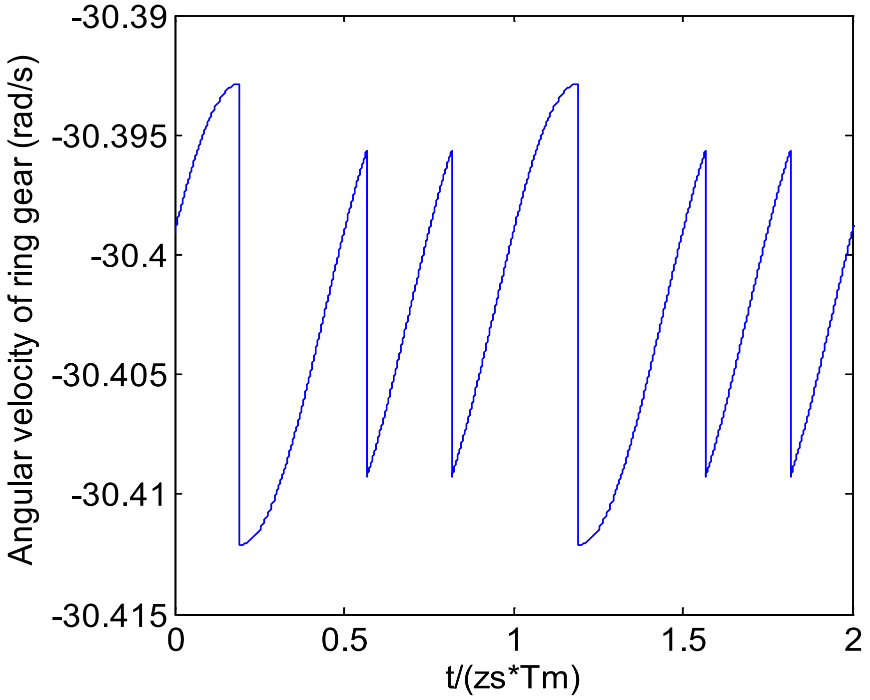

Figure 7-b – Angular velocity of ring-gear versus time

5 – Time, position-varying mesh stiffness functions

The computation of realistic mesh stiffness functions at the various interfaces is still a challenging issue. However, it has been demonstrated that a thin-slice approach eventually leading to a scalar time-varying and possibly non-linear stiffness function was able to capture most of the dynamic mesh features. Depending on tooth geometry, the exact calculation can be complex and require sophisticated 3D finite element models hardly compatible with dynamic simulations and extensive parameter analyses. In order to focus on the specific physical phenomena associated with planetary gears with position and eccentricity errors, a simplified approach has been chosen which relies on a constant mesh stiffness per unit of contact length (as is the case in the developments in the ISO 6336 standard).

5.1 – Parameters definition

The following parameters are introduced (see Figure 8):

a) $\mathbf{L}_{Sj}', \mathbf{L}_j^{*}'$: points of tangency between the actual base planes and base cylinders for sun-gear/planet #j and ring-gear/planet #j.

b) $\mathbf{I}_j', \mathbf{I}_j^{*}'$ are two unit vectors in the direction of the line of contact translations in the base plane for sun-gear/planet #j, and planet #j/ring-gear. Their coordinates in the frame attached to the sun-gear/planet #1 centre line are:

$$\mathbf{I}_j' = \mathbf{x}_1 \cdot \sin\left(\alpha_{Sj}' - \varepsilon_S \Phi_{Sj}'\right) + \mathbf{y}_1 \cdot \varepsilon_S \cos\left(\alpha_{Sj}' - \varepsilon_S \Phi_{Sj}'\right)$$
$$\mathbf{I}_j^{*}' = \mathbf{x}_1 \cdot \sin\left(\alpha_{Rj}' + \varepsilon_S \Phi_{Rj}'\right) - \mathbf{y}_1 \cdot \varepsilon_S \cos\left(\alpha_{Rj}' + \varepsilon_S \Phi_{Rj}'\right) \tag{20}$$

Alternatively, their coordinates expressed in a frame attached to the sun-gear/planet #j centre line read:

$$\mathbf{I}_j' = \mathbf{x}_j \cdot \sin \alpha_{Sj}' + \mathbf{y}_j \cdot \varepsilon_S \cos \alpha_{Sj}'$$
$$\mathbf{I}_j^{*}' = \mathbf{x}_j \cdot \sin \alpha_{Rj}' - \mathbf{y}_j \cdot \varepsilon_S \cos \alpha_{Rj}' \tag{21}$$

From a general viewpoint, the instant geometry is deduced from the nominal (constant) PTG geometry on which first order variations caused by assembly errors and elastic deformation are superimposed, thus leading to non-linear mesh stiffness and mesh forces. The most important parameters are:

- the instant centre distance of sun-gear/planet #j or ring-gear/planet #j (Figure 8) defined as:

$$\begin{aligned} R_{gj}' &= \left|\mathbf{G}_g\mathbf{G}_j\right| = \left|-e_g\mathbf{T}_g - x_g\mathbf{x}_1 - y_g\mathbf{y}_1 + e_c\mathbf{T}_c + R_C\mathbf{x}_j + e_{xj}\mathbf{x}_j + e_{yj}\mathbf{y}_j + x_j\mathbf{x}_j + y_j\mathbf{y}_j + e_j\mathbf{T}_j\right|, g = S, R \\ &= \Delta R_{gj} + R_C \end{aligned} \tag{22}$$

with:

$\mathbf{G}_i$: geometrical centre of member $i = S, R, C, j$, sun-gear, ring-gear, carrier, planet #j

$\Delta R_{gj} = -e_g \cos(\Phi_j - \psi_g) - x_g \cos \Phi_j - y_g \sin \Phi_j + e_C \cos(\Phi_j - \psi_C) + e_{xj} + x_j + e_j \cos\left(\psi_j\right)$

in which, second-order terms of the form $\left(e_i / R_i\right)^2$ are discarded.

- the instant pressure angles which can be deduced by using the following equations:

$$R_{gj}' \mathit{cos}\, \alpha_{gj}' = R_{gj} \mathit{cos}\, \alpha_{gj} = Rb_S + Rb_j \;\mathit{or}\; Rb_R - Rb_j \tag{23}$$

$$R_{gj}'\cos\alpha_{gj}' = \left(R_{gj}+\Delta R_{gj}\right)\cos\left(\alpha_{gj}+\Delta\alpha_{gj}\right) \\ = R_{gj}\cos\alpha_{gj} - R_{gj}\sin\alpha_{gj}\Delta\alpha_{gj} + \Delta R_{gj}\cos\alpha_{gj} \qquad (24)$$

which give the variation in pressure angle as:

$$\Delta\alpha_{gj} = \frac{\Delta R_{gj}}{R_{gj}\cdot tg\alpha_{gj}} \qquad (25)$$

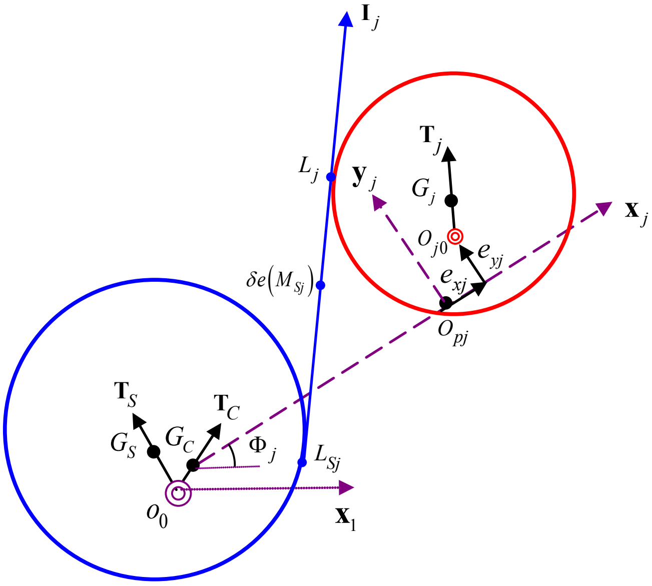

Figure 8-a – Sun-gear/planet #j mesh with varying parameters

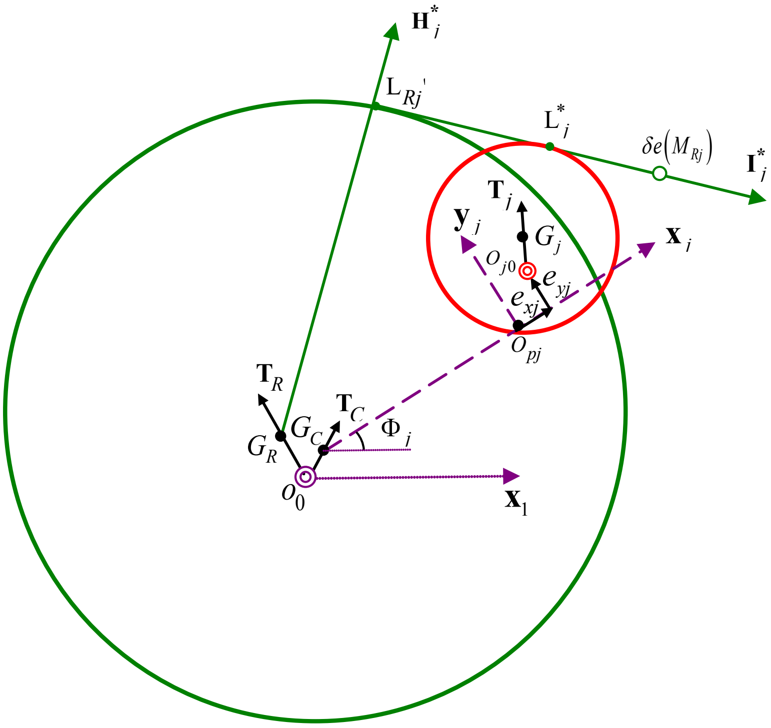

Figure 8-b – Planet #j/ring-gear mesh with varying parameters

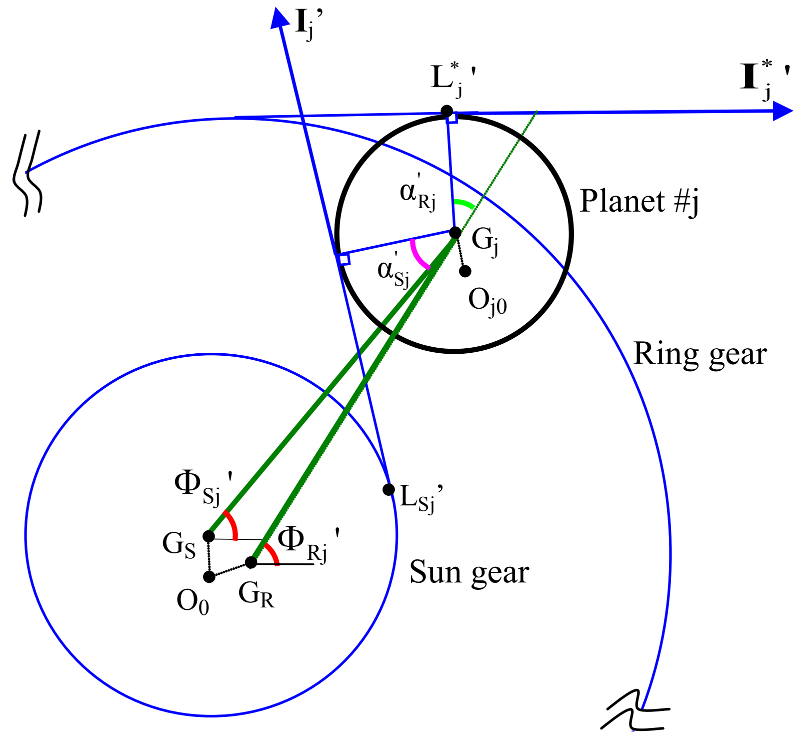

Figure 8 – Planetary gear geometry with varying parameters

5.2 – Potential position of the border of mesh zone (Figure 9)

In a second phase, the limits of the meshing zones in all the base planes which depend on deflections and errors are established. For sun (ring)-gear /planet #j interface, point $\mathbf{S}_{gj}'$ represents the start point of meshing (engagement) and $\mathbf{E}_{gj}'$, the end point corresponding to the end of recess (g = S, R). These points, shown in Figure 9, define the border of the meshing zone in the base planes.

For sun-gear/planet #j base plane, the position of $\mathbf{S}_{Sj}'$ is defined as the intersection of the addendum circle of planet #j and the base plane so that the corresponding distance $\mathbf{L}_{Sj}'\mathbf{S}_{Sj}'$ from the tangency to the base cylinder is:

$$\begin{aligned}\mathbf{L}_{Sj}'\mathbf{S}_{Sj}' &= \mathbf{L}_{Sj}'\mathbf{L}_j' - \mathbf{S}_{Sj}'\mathbf{L}_j' = \mathbf{G}_S\mathbf{G}_j \cdot \mathbf{I}_j' - \sqrt{Ra_j^{\,2} - Rb_j^{\,2}} \cdot \mathbf{I}_j' \\ &= R_{Sj}'\sin\left(\alpha_{Sj}'\right) \cdot \mathbf{I}_j' - \sqrt{Ra_j^{\,2} - Rb_j^{\,2}} \cdot \mathbf{I}_j'\end{aligned} \tag{26}$$

In the same way, the end point of meshing $\mathbf{E}_{Sj}'$ is placed at the intersection of the sun-gear addendum circle and the base plane such that:

$$\mathbf{L}_{Sj}'\mathbf{E}_{Sj}' = \sqrt{Ra_S^{\;2} - Rb_S^{\;2}}\;\mathbf{I}_j' \tag{27}$$

Considering now the internal meshes between ring-gear/planet #j, a similar reasoning leads to the position of the start mesh point $\mathbf{S}_{Rj}'$ as:

$$\begin{aligned}\mathbf{L}_j^*{}'\mathbf{S}_{Rj}' &= \mathbf{L}_{Rj}'\mathbf{S}_{Rj}' - \mathbf{L}_{Rj}'\mathbf{L}_j^*{}' = \sqrt{Rt_R^{\;2} - Rb_R^{\;2}}\cdot\mathbf{I}_j^* - \mathbf{G}_R\mathbf{G}_j^*\cdot\mathbf{I}_j^*{}' \\ &= \sqrt{Rt_R^{\;2} - Rb_R^{\;2}}\cdot\mathbf{I}_j^*{}' - R_{Rj}'\sin\left(\alpha_{Rj}'\right)\cdot\mathbf{I}_j^*{}'\end{aligned} \tag{28}$$

and the end mesh point $\mathbf{E}_{Rj}'$ as:

$$\mathbf{L}_j^*{}'\mathbf{E}_{Rj}' = \sqrt{Ra_j^{\;2} - Rb_j^{\;2}}\;\mathbf{I}_j^*{}' \tag{29}$$

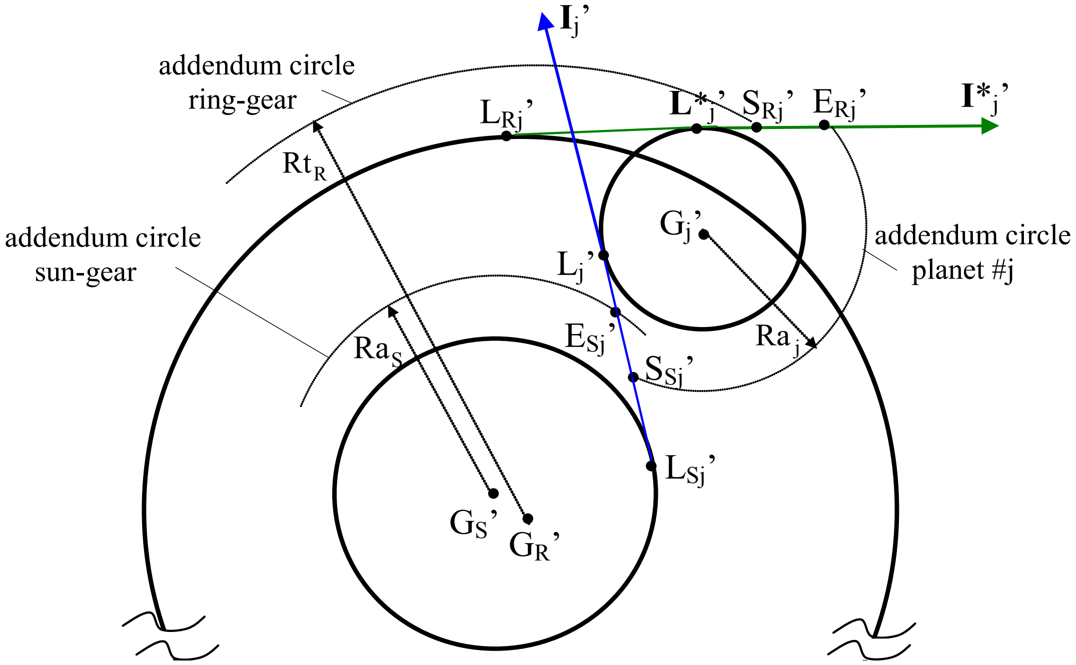

Figure 9 – Limits of engagement on base planes

5.3 – Positions of the contact lines

The next step consists in following the evolutions of the contact lengths in all the time-varying base planes. To this end, the methodology presented by Abousleiman et al. [60] has been used. It is, first, conventionally assumed that i) the initial conditions correspond to the engagement of one tooth pair at point $\mathbf{S}_{S1}'$, the first point of contact for this particular mesh on the base plane of sun-gear/planet #1 and, ii) the other positions for all the contact lines can be deduced once the relative mesh phases are obtained.

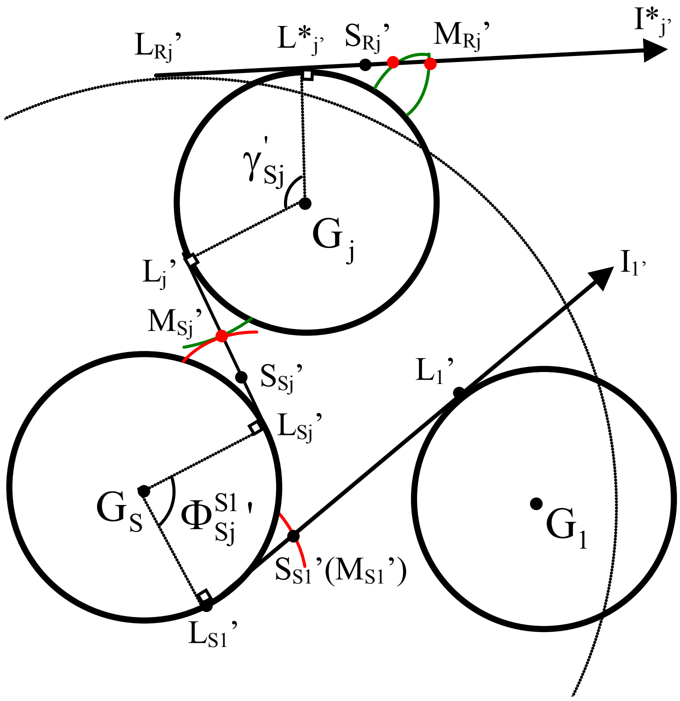

Figure 10 – Initial mesh positions and phases

By setting the initial position of sun-gear/planet #1, all the contact points of mesh pairs in a planetary gear train can be located by means of calculating of mesh phases on the action planes.

The mesh phases for sun-gear/planet #j relative to that of sun-gear /plant #1 Δ_{Sj}^{S1}, is deduced as:

$$\Delta_{Sj}^{S1} = \left\| \frac{\left|\mathbf{S}_{Sj}'\mathbf{M}_{Sj}'\right|}{pb_a} \right\| \tag{30}$$

where the distance $\left|\mathbf{S}_{Sj}'\mathbf{M}_{Sj}'\right|$ between the potential point of contact $\mathbf{M}_{Sj}'$ and mesh start point $\mathbf{S}_{Sj}'$ (Figure 10) in the $\mathbf{I}_j'$ direction of the sun-gear/planet #j base plane reads:

$$\begin{aligned} \left|\mathbf{S}_{Sj}'\mathbf{M}_{Sj}'\right| &= \left|\mathbf{L}_{S1}'\mathbf{S}_{S1}'\right| + \left|\mathbf{S}_{S1}'\mathbf{M}_{Sj}'\right| - \overset{\frown}{L_{S1}'L_{Sj}'} - \left|\mathbf{L}_{Sj}'\mathbf{S}_{Sj}'\right| \\ &= \left|\mathbf{L}_{S1}'\mathbf{S}_{S1}'\right| + \varepsilon_S N \cdot pb_a - \varepsilon_S \Phi_{Sj}^{S1}{}' Rb_S - \left|\mathbf{L}_{Sj}'\mathbf{S}_{Sj}'\right| \end{aligned} \tag{31}$$

where, $\Phi_{Sj}^{S1}{}' = \Phi_{Sj}' - \Phi_{S1}'$.

If M_{Sj}' is outside the actual contact zone (the $S_{Sj}'E_{Sj}'$ interval). Δ_{Sj}^{S1} is decremented by integer multiples of the apparent base pitch until M_{Sj}' lies between the contact $S_{Sj}'E_{Sj}'$. Since one point of contact is located, all the contact lines in the considered base plane are deduced by an integer of apparent base pitch far from point M_{Sj}' .

The mesh phase of ring-gear/planet #j, relative to that of sun-gear/planet #1 Δ_{Rj}^{S1} can be derived when all the initial positions for sun-gear/planet meshes are known and one obtains:

$$\Delta_{Rj}^{S1} = \left\| \frac{\left|\mathbf{S}_{Rj}'\mathbf{M}_{Rj}'\right|}{pb_a} \right\| = \Delta_{Sj}^{S1} + \left\| \frac{S_{bj} - \left|\mathbf{S}_{Sj}'\mathbf{S}_{Rj}'\right|}{pb_a} \right\| \tag{32}$$

with:

pb_a : apparent base pitch

S_{bj} : tooth thickness on the base circle tangential line

By virtue of the involutes properties and because of opposite active tooth flanks on external and internal meshes, the following equations are obtained which make it possible to express the position of one potential point of contact M_{Sj}' between planet #j and ring-gear $\left|\mathbf{S}_{Rj}'\mathbf{M}_{Sj}'\right|$ (Figure 10):

$$\left|\mathbf{S}_{Rj}'\mathbf{M}_{Sj}'\right| = \left|\mathbf{S}_{Sj}'\mathbf{M}_{j}'\right| + \varepsilon_S N \cdot pb_a + S_{bj} - \left|\mathbf{S}_{Sj}'\mathbf{S}_{Rj}'\right| \tag{33}$$

with:

$$\begin{aligned} \left|\mathbf{S}_{Sj}'\mathbf{S}_{Rj}'\right| &= \left|\mathbf{S}_{Sj}'\mathbf{L}_{j}'\right| + \widehat{L_j'L_j^{*}'} + \left|\mathbf{L}_{j}^{*}'\mathbf{S}_{Rj}'\right| = \left|\mathbf{S}_{Sj}'\mathbf{L}_{j}'\right| + \widehat{L_j'L_j^{*}'} + \left|\mathbf{L}_{Rj}^{*}'\mathbf{S}_{Rj}'\right| - \left|\mathbf{L}_{Rj}^{*}'\mathbf{L}_{j}^{*}'\right| \\ &= \sqrt{Ra_j^2 - Rb_j^{\,2}} + \gamma_{\mathrm{Sj}}' \cdot Rb_j + \sqrt{Ra_R^2 - Rb_R^{\,2}} - R_{Rj}'\sin(\alpha_{Rj}') \end{aligned} \tag{34}$$

$$\gamma_{\mathrm{Sj}}' = \pi - \vartheta_{SR}^{j} - \alpha_{Sj}' - \alpha_{Rj}'\,;\ \vartheta_{SR}^{j} \approx \Phi_{Rj}' - \Phi_{Sj}' \text{ see (Figure 11)}$$

The engagement of planet #j with both the sun-gear and the ring-gear (Figure 10), introduces a mesh phase between the two meshes, which relatives to the curvilinear distance on action plan between L_j' and L_j^{*}', and opposite active tooth flanks on external and internal meshes S_{bj}.

As previously, M_{Rj}'may be outside the contact zone and, in such situation, Δ_{Rj}^{S1} A/j is decreased by integer multiples of the apparent base pitch until M_{Rj}'represents an actual point of contact.

where the planet spacing angle Φ_{gj}'around sun(ring)-gear is defined by:

$$\Phi_{gj}' = \angle \mathbf{G}_g\mathbf{G}_j, \mathbf{x}_1 = \Delta\Phi_{gj} + \Phi_{gj}$$

and

$$\Delta\Phi_{gj} \approx \frac{\mathbf{G}_g\mathbf{G}_j}{\left\|\mathbf{G}_g\mathbf{G}_j\right\|}\cdot\mathbf{y}_j \approx \frac{\left(-e_g\mathbf{T}_g - x_g\mathbf{x}_1 - y_g\mathbf{y}_1 + e_C\mathbf{T}_C + R_C\mathbf{x}_j + e_{xj}\mathbf{x}_j + e_{yj}\mathbf{y}_j + x_j\mathbf{x}_\mathbf{j} + y_j\mathbf{y}_\mathbf{j} + e_j\mathbf{T}_j\right)}{R_C}\cdot\mathbf{y}_j$$
$$\approx\left\{x_g\sin\Phi_j - y_g\cos\Phi_j + e_g\sin\left(\Phi_j - \psi_g\right) - e_C\sin\left(\Phi_j - \psi_C\right) + e_{yj} + y_j + e_j\sin\psi_j\right\}/R_C \tag{35}$$

Finally, the initial mesh phase of ring-gear/plant #j relative to that of sun-gear/plant #1 is defined by:

$$\Delta_{Rj}^{Sj} = \Delta_{Rj}^{S1} - \Delta_{Sj}^{S1} \tag{36}$$

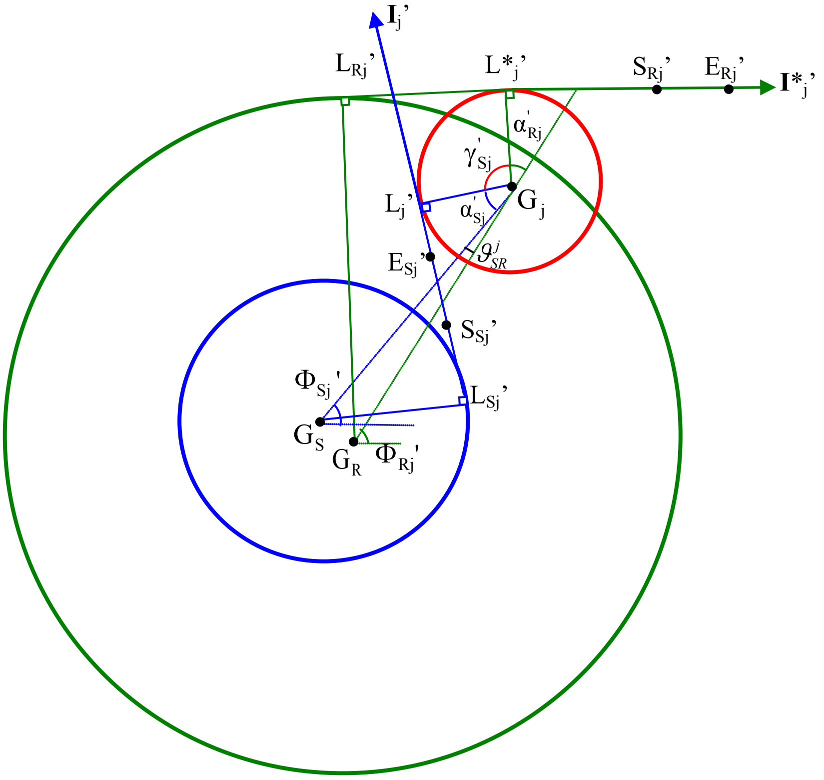

Figure 11 – Parameter definition for mesh positions and phases

5.4 – Instantaneous positions of potential contact points M_{gj}', $M_{gj}^{*}{}'$ at any time

Once the initial positions of the contact lines are known, their evolutions can be determined step-by-step in time or using Taylor first order developments.

a) Sun-gear / planet #j:

- Supposing that, at time t, for sun-gear/planet #j mesh pair, in Figure 12, the distance of $\left|\mathrm{L_{Sj}}'\mathrm{M_{Sj}}\right|^{\mathrm{t}}=\left(\mathrm{L_{Sj}}'\mathrm{M_{Sj}}\right)^{\mathrm{t}}\cdot\left(\mathrm{I_j}'\right)^{\mathrm{t}}$ is known, $\left|\mathbf{L}_{Sj}'\mathbf{M}_{Sj}'\right|^{t+\Delta t}$ with respect to reference frame '$\Im$', can be expressed as:

$$\begin{aligned}\left|\mathbf{L}_{Sj}'\mathbf{M}_{Sj}'\right|^{t+\Delta t}&=\left(\mathbf{L}_{Sj}'\mathbf{M}_{Sj}'\cdot\mathbf{I}_j'\right)^{t+\Delta t}\approx\left(\mathbf{L}_{Sj}'\mathbf{M}_{Sj}'\cdot\mathbf{I}_j'\right)^{t}+\frac{d^{\Im}}{dt}\left(\mathbf{L}_{Sj}'\mathbf{M}_{Sj}'\cdot\mathbf{I}_j'\right)^{t}\cdot dt\\&\approx\left(\mathbf{L}_{Sj}'\mathbf{M}_{Sj}'\cdot\mathbf{I}_j'\right)^{t}+\frac{d^{\Im}}{dt}\left(\mathbf{L}_{Sj}'\mathbf{M}_{Sj}'\right)^{t}\cdot\left(\mathbf{I}_j'\right)^{t}\cdot dt+\left(\mathbf{L}_{Sj}'\mathbf{M}_{Sj}'\right)^{t}\cdot\frac{d^{\Im}}{dt}\left(\mathbf{I}_j'\right)^{t}\cdot dt\end{aligned}\tag{37}$$

In the equation above, $\frac{d^{\Im}}{dt}\left(\mathbf{L}_{Sj}'\mathbf{M}_{Sj}'\right)^{t}\left(\mathbf{I}_j'\right)^{t}$ can be separated into two parts as:

$$\frac{d^{\Im}}{dt}\left(\mathbf{L}_{Sj}'\mathbf{M}_{Sj}'\right)^{t}\left(\mathbf{I}_j'\right)^{t}=\frac{d^{\Im}}{dt}\left(\mathbf{O}_0\mathbf{L}_{Sj}'-\mathbf{O}_0\mathbf{M}_{Sj}'\right)^{t}\cdot\left(\mathbf{I}_j^{*}{}'\right)^{t}=\frac{d^{\Im}}{dt}\left(\mathbf{O}_0\mathbf{L}_{Sj}'\right)^{t}\cdot\left(\mathbf{I}_j^{*}{}'\right)^{t}-\frac{d^{\Im}}{dt}\left(\mathbf{O}_0\mathbf{M}_{Sj}'\right)^{t}\cdot\left(\mathbf{I}_j^{*}{}'\right)^{t}\tag{38}$$

The two scalar products in (38) can be developed as follows:

1) $\frac{d^{\Im}}{dt}\left(\mathbf{O}_0\mathbf{M}_{Sj}'\right)^{t}\cdot\left(\mathbf{I}_j'\right)^{t}=\mathbf{V}_S^{\Im}\left(M_{Sj}'\right)^{t}\cdot\left(\mathbf{I}_j'\right)^{t}$

$$\begin{aligned}&=\left[\mathbf{V}_S^{\Im}(\boldsymbol{\Omega}\mathbf{O}_0)+\mathbf{O}\,{}_S^{\Im}\mathbf{G}\times\left(\mathbf{G}_S\,\mathbf{L}_S+\mathbf{L}_S\,{}_{Sj}\mathbf{M}\,{}_{Sj}'\,{}_{Sj}'\right)\right]^{t}\cdot\left(\mathbf{I}_j'\right)^{t}\\&=\left[\frac{d^{\Im}}{dt}\left(x_S\mathbf{x}_1+\boldsymbol{\Omega}y_S\mathbf{y}_1\right)\mathbf{O}+\mathbf{G}_S^{\Im}\times\left({}_S\,\mathbf{H}_S-\varepsilon_S\mathbf{R}b_S\,\mathbf{M}_j'+{}_{Sj}'\,{}_{Sj}'\right)\right]^{t}\cdot\left(\mathbf{I}_j'\right)^{t}\\&=\left[\dot{x}_S\mathbf{x}_1+\dot{y}_S\mathbf{y}_1+\varepsilon_S\Omega_S e_S\cos\sigma_S\cdot\mathbf{I}_j'+\varepsilon_S\Omega_S Rb_S\cdot\mathbf{I}_j'\right]\cdot\left(\mathbf{I}_j'\right)^{t}\end{aligned}\tag{39-a}$$

with:

$\mathbf{O}_S,\mathbf{O}_R,\mathbf{O}_j$: position of deflexion of sun-gear, ring-gear, and planet #j in the planetary geometry and noticing that:

$$\boldsymbol{\Omega}_S^{\Im} \times \mathbf{G}_S\mathbf{L}_{Sj}' = \boldsymbol{\Omega}_S^{\Im} \times \left(-\varepsilon_S Rb_S \mathbf{H}_j'\right) = \varepsilon_S \Omega_S Rb_S \cdot \mathbf{I}_j';$$

$\left(\mathbf{L}_{Sj}'\mathbf{M}_{Sj}'\right)^t // \left(\mathbf{I}_j'\right)^t$, so $\boldsymbol{\Omega}_S^{\Im} \times \left(\mathbf{L}_{Sj}'\mathbf{M}_{Sj}'\right)^t \cdot \left(\mathbf{I}_j'\right)^t = 0$;

$\mathbf{H}_j'$ is the perpendicular vector of $\mathbf{I}_j'$

$$\frac{d^{\Im}}{dt}\mathbf{H}_j' = \left(-\varepsilon_S \dot{\alpha}_{Sj}' + \dot{\Phi}_{Sj}'\right)\mathbf{Z}_0 \times \mathbf{H}_j' = \left(\varepsilon_S \dot{\alpha}_{Sj}' - \dot{\Phi}_{Sj}'\right)\mathbf{I}_j'$$

the angle between $\mathbf{x}_1$ and $\mathbf{H}_j'$: Anti-clockwise: $\angle \mathbf{H}_j', \mathbf{x}_1 = \pi - \alpha_{Sj}' + \Phi_{Sj}'$, clockwise: $\angle \mathbf{H}_j', \mathbf{x}_1 = \alpha_{Sj}' + \Phi_{Sj}'$.

2) $$\frac{d^{\Im}}{dt}\left(\mathbf{O}_0\mathbf{L}_{Sj}'\right)^t \cdot \left(\mathbf{I}_j'\right)^t = \left[\frac{d^{\Im}}{dt}\left(\mathbf{O}_0\mathbf{O}_S + \mathbf{O}_S\mathbf{G}_S + \mathbf{G}_S\mathbf{L}_{Sj}'\right)\right]^t \cdot \left(\mathbf{I}_j'\right)^t$$

$$\begin{aligned} &= \left[\frac{d^{\Im}}{dt}\left(x_S\mathbf{x}_1 + y_S\mathbf{y}_1 + \mathbf{O}_S\mathbf{G}_S - \varepsilon_S Rb_S \mathbf{H}_j'\right)\right]^t \cdot \left(\mathbf{I}_j'\right)^t \\ &= \left[\dot{x}_S\mathbf{x}_1 + \dot{y}_S\mathbf{y}_1 + \varepsilon_S \Omega_S e_S \cos\sigma_S \cdot \mathbf{I}_j' - \varepsilon_S Rb_s \left(\varepsilon_S \dot{\alpha}_{Sj}' - \dot{\Phi}_{Sj}'\right) \cdot \mathbf{I}_j'\right]^t \cdot \mathbf{I}_j' \end{aligned} \tag{39-b}$$

Noticing that $\frac{d^{\Im}}{dt}\left(\mathbf{I}_j'\right) \cdot \left(\mathbf{I}_j'\right)^t = 0$, one obtains:

$$\left(\mathbf{L}_{Sj}'\mathbf{M}_{Sj}'\right)^t \cdot \frac{d^{\Im}}{dt}\left(\mathbf{I}_j'\right)^t \cdot dt = 0 \tag{40}$$

Combining (39-a & b) and (40) finally leads to the expression of $\left|\mathbf{L}_{sj}'\mathbf{M}_{Sj}'\right|^{t+\Delta t}$ under the form:

$$\begin{aligned} \left|\mathbf{L}_{Sj}'\mathbf{M}_{Sj}'\right|^{t+\Delta t} &= \left|\mathbf{L}_{Sj}'\mathbf{M}_{Sj}'\right|^{t} + \frac{d^{\Im}}{dt}\left(\mathbf{O}_0\mathbf{M}_{Sj}'\right)^t \cdot \left(\mathbf{I}_j'\right)^t - \frac{d^{\Im}}{dt}\left(\mathbf{O}_0\mathbf{L}_{Sj}'\right)^t \cdot \left(\mathbf{I}_j'\right)^t \\ &= \left|\mathbf{L}_{Sj}'\mathbf{M}_{Sj}'\right|^{t} + \left[\varepsilon_S \Omega_S Rb_S + \varepsilon_S Rb_S \left(\varepsilon_S \dot{\alpha}_{Sj}' - \dot{\Phi}_{Sj}'\right)\right]^t \cdot dt \end{aligned} \tag{41}$$

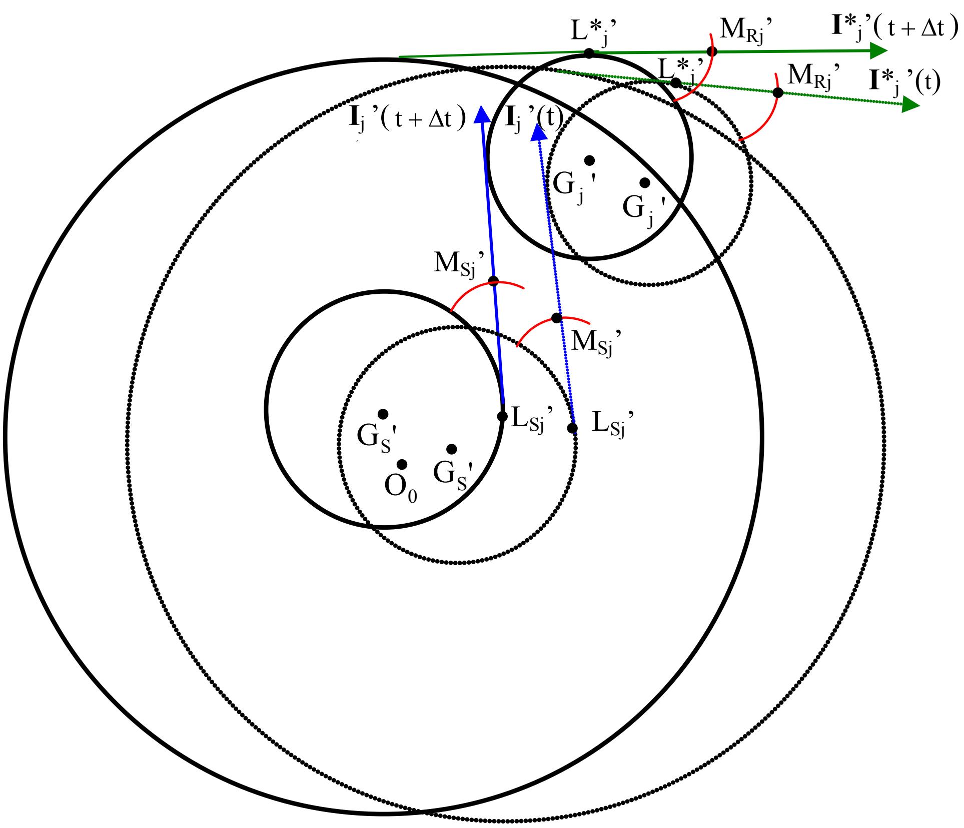

Figure 12 – Instantaneous positions of potential contact points

b) Ring-gear/ planet #j

Using similar developments, the following expression is obtained which gives the positions at $t+\Delta t$:

$$\begin{aligned}\left|\mathbf{L}_j^*{}'\mathbf{M}_{Rj}{}'\right|^{t+\Delta t} &= \left|\mathbf{L}_j^*{}'\mathbf{M}_{Rj}{}'\right|^{t} + \frac{d^{\Im}}{dt}\left(\mathbf{O}_0\mathbf{M}_{Rj}{}'\right)^t \cdot \left(\mathbf{I}_j^*{}'\right)^t - \frac{d^{\Im}}{dt}\left(\mathbf{O}_0\mathbf{L}_j^*{}'\right)^t \cdot \left(\mathbf{I}_j^*{}'\right)^t \\ &= \left|\mathbf{L}_j^*{}'\mathbf{M}_{Rj}{}'\right|^{t} + \left[-\varepsilon_S\Omega_j Rb_j + \varepsilon_S Rb_j\left(\varepsilon_S\dot{\alpha}_{Rj}{}' + \dot{\Phi}_{Rj}{}'\right)\right]^t dt\end{aligned} \tag{42}$$

Finally, the time-derivatives of the planet spacing angles $\Phi_{gj}{}'$, of the centre-distances of sun (ring)-gear/planets $R_{gj}{}'$ and pressure angles of sun (ring)-gear/planets α_{gj} read:

$$\dot{\Phi}_{gj}{}' = \left\{\dot{x}_g\sin\Phi_j - \dot{y}_g\cos\Phi_j - e_g\left(\Omega_{g0}\right)\cos\left(\Phi_j - \psi_g\right) + \dot{y}_j + \Omega_{j0}e_j\cos\left(-\psi_j\right)\right\}/R_C \tag{43-a}$$

$$\dot{R}_{gj}{}' = -\dot{x}_g\cos\Phi_j - \dot{y}_g\sin\Phi_j - e_g\Omega_{g0}\sin(\Phi_j - \psi_g) + \dot{x}_j + e_j\Omega_{j0}\sin\left(-\psi_j\right) \tag{43-b}$$

$$\dot{\alpha}_{gj}{}' \approx \frac{\dot{R}_{gj}{}'}{R_C \cdot tg\alpha_{gj}} \tag{43-c}$$

5.5 – Length of mesh lines in contact zone

Under the hypothesis that, at every time step, the mesh parameters are constant, the length of one contact line l in the contact zone is given as:

a) for spur gear $l = b$ where *b* is the tooth width

b) and for helical gears (Figure 13), $l = |A_a A_b|$ where $|A_a A_b|$ is the distance between the two intersecting points between the inclined contact line and the limits of the mesh zone in the base plane.

At any time t, the position of first contact line in the contact zone on the sun (ring)-gear/planet #j base plane is given by $\mathbf{L}_{gj}'\mathbf{M}_1$ is:

$$\mathbf{L}_{gj}'\mathbf{M}_1' = \left\| \frac{\left|\mathbf{L}_{gj}'\mathbf{M}_{gj}'\right|^{t+\Delta t}}{pb_a} \right\| \tag{44}$$

whereas, the other contact lines are deduced from:

$$\mathbf{L}_{gj}'\mathbf{M}_i' = \mathbf{L}_{gj}'\mathbf{M}_1' + (i-1)\cdot \mathrm{p}_{\mathrm{ba}} \qquad i=1,\ 2,\ 3... \tag{45}$$

$$\mathrm{L}_{\mathrm{gj}}'\mathrm{S}_{\mathrm{gj}}' \le \mathrm{L}_{\mathrm{gj}}'\mathrm{M}_i' \le \mathrm{L}_{\mathrm{gj}}'\mathrm{B}_{\mathrm{j}}'$$

where p_{ba} is the apparent base pitch

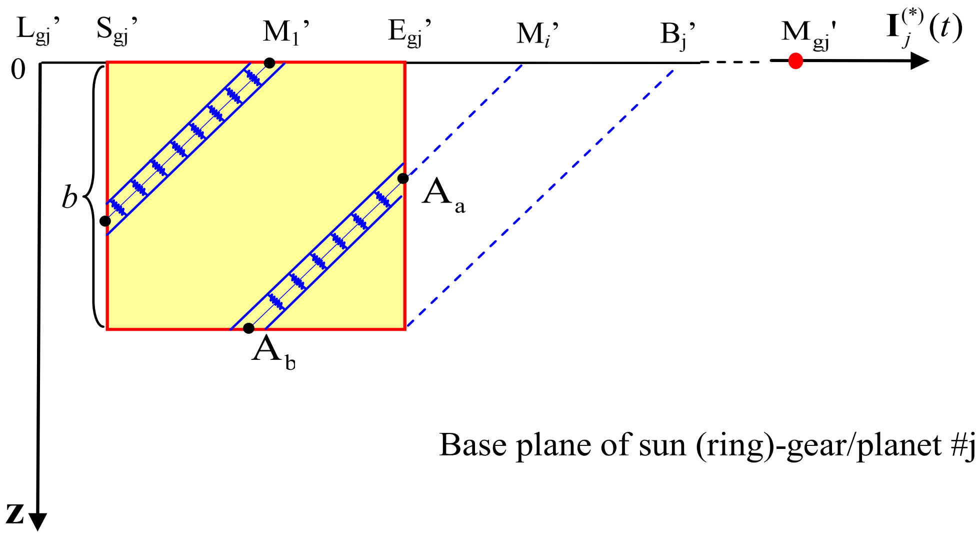

Figure 13 – Length of contact lines in meshing area

At time t, the sum of all contact lines in a contact zone is expressed as:

$$L\left(t+\Delta t,\mathbf{X}\right)=\sum_{i=1}^{i} l\left(M_i{}'\right) \tag{46}$$

The deformable part of the sun (ring)-gear/planet mesh pair is assimilated to a Winckler type foundation formed by a series of lumped stiffness elements distributed along the potential lines of contact on the theoretical base planes, each of them being related to a cell of the contact line discretization (thin-slice approach). Mesh stiffness per unit of contact length k_0 can be determined by various methods (finite elements, Weber-Banaschek formulae [8], ISO/DIS 6336 formula [16] …).

Finally, the mesh stiffness functions are derived by assuming that they are proportional to the instant contact lengths.

$$\hat{k}(t+\Delta t,\mathbf{X}) = k_0 \cdot L\left(t+\Delta t,\mathbf{X}\right) \tag{47}$$

5.6 – Some examples of mesh stiffness functions

Example 1– Mesh stiffness function of planetary gear with planet position errors

Considering a planetary gear (see Table 1, case 2) with a tangential error of $e_{y1} = 10^{-4} m$ on planet #1 and a tangential position error on planet #2 of $e_{y2} = -7 \cdot 10^{-5} m$, (anti-clockwise planet distribution), the sun-gear / planet mesh stiffness evolutions versus the dimensionless time are shown in Figure 14. The planets are in phase and equally spaced around the carrier. The black solid line is the mesh stiffness function for the errorless situation whereas the other curves correspond to the contributions of the planet errors. It can be noticed that the mesh stiffness functions are modified because of the influence of time-varying speeds (leading to frequency modulations), time-varying contact ratios (giving rise to amplitude modulations) and the natural contact length time-variations associated with the meshing process.

Table 1 – Planetary gear sets

	Sun-gear	Planet	Ring-gear
Tooth number			
case 1 (experiments)	73	26	125
case 2 (numerical analyses)	72	26	124

Normal module [mm]	1.81		1.81		1.81
Helix angle [°]		20		20	
Pressure angle [°]		23.04		23.04	
Addendum diameter [mm]	139.7		51.6		-
Dedendum diameter [mm]	-		-		229.4
Centre distance [mm]			92.12		
Active face width [mm]		25		25	

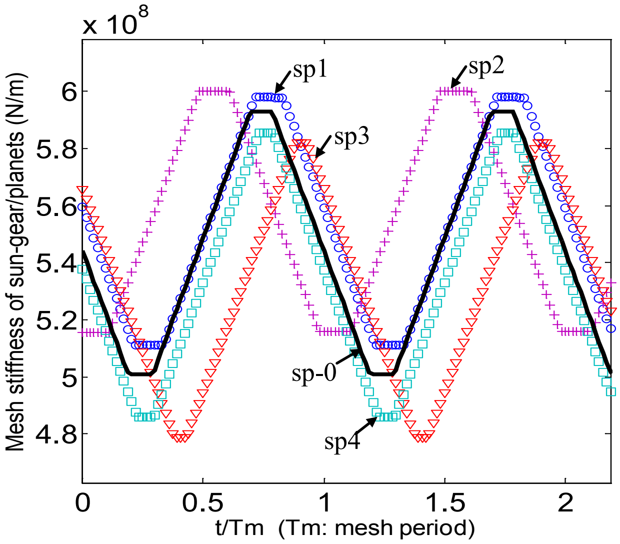

Figure 14-a – Example of sun-gear/planet mesh stiffness functions

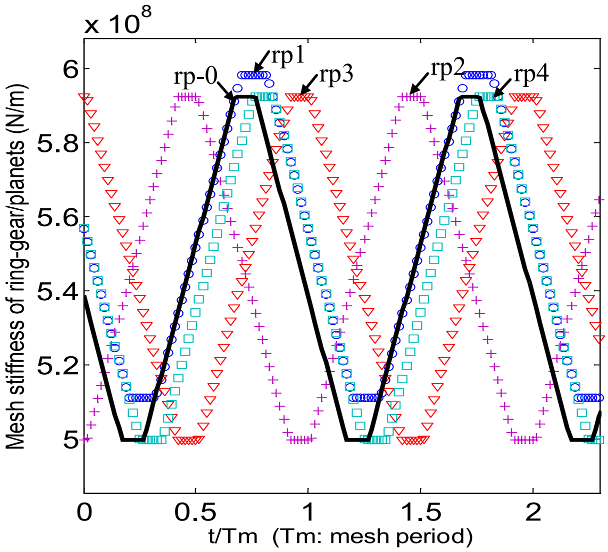

Figure 14-b – Example of ring-gear/planet mesh stiffness functions

Keys:

Errorless: — s/rp-0 *sun(ring)-gear/planets*

With error: ○ s/rp1 *sun(ring)-gear/planet #1* + s/rp2 *sun(ring)-gear/planet #2*

▽ s/rp3 *sun(ring)-gear/planet #3* □ s/rp4 *sun(ring)-gear/planet #4*

Example 2–Mesh stiffness function of planetary gear with an eccentricity on sun-gear

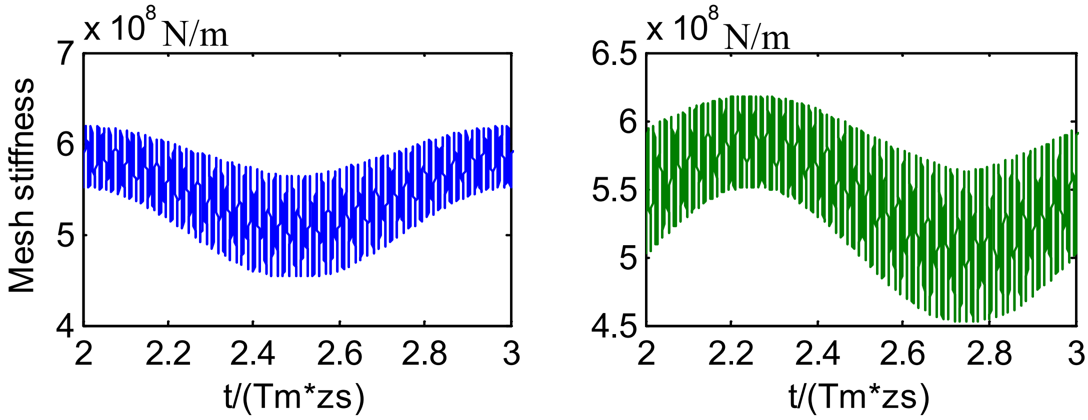

(a) sun-gear/planet #1 (b) sun-gear/planet #2

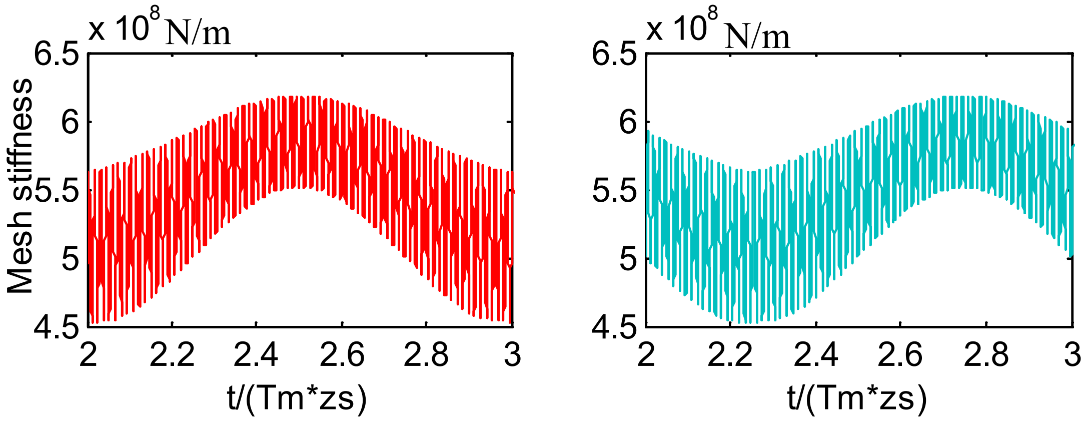

(c) sun-gear/planet #3 (d) sun-gear/planet #4

Figure 15 – Mesh stiffness functions of sun-gear/planets
ring-gear rotating, an eccentricity error $es = 200\ \mu m$ on sun-gear

Figure 15 shows an example of sun-gear / planet mesh stiffness versus time for the same 4-planet gear set but with an eccentricity error of es =200 μm on the sun-gear. Because of the presence of eccentricity on the sun-gear, mesh stiffness functions are modulated by the sun-gear rotational period and a sequential phase delay appears between the stiffness for each sun-gear / planet mesh.

6 – Planetary gear dynamic model

A simplified lumped parameter model with one rotational DOF (torsion) and two perpendicular translational DOFs (bending) per member has been set up (Figure 16). In this model, a wide range of practical situations (rotating carrier, input speed, sun-gear motion, floating members, etc.) can be covered, while remaining sufficiently light in terms of modelling effort and computational times.

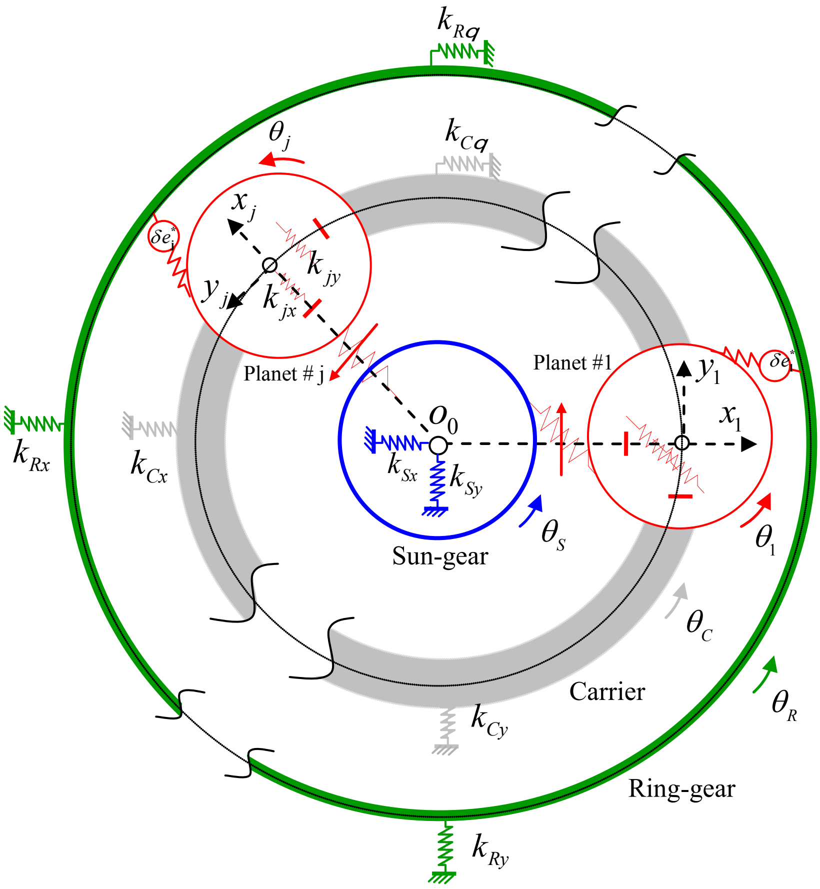

Figure 16 – Degree of freedom definition – Lumped parameter model

6.1 – Degree-of-freedom (DOF) definition

For planetary gears with rotating carriers, the base planes are fixed to the frame attached to the carrier which is rotating with respect to the inertial coordinate system. The contact length and mesh stiffness evolutions are defined with respect to these base planes and complex modulations may arise with regard to an observer fixed to the inertial frame. In these conditions, it is interesting to define the degree-of-freedom vector in the coordinate system attached to the carrier with the drawback of generating gyroscopic and centrifugal effects. Depending on the nature of the elements, two different configurations are considered:

a) For central members (sun-gear, ring-gear and carrier), the translational DOFs are described via screws of infinitesimal generalized displacements attributed to rigid solid reference frame $\left\{S^{\wp 1}\right\}$ attached to the sun-gear/planet #1 centre line direction (under the ideal planetary structure without errors) and its perpendicular direction (Figure 17) such that:

$$\left\{S_k^{\wp 1}\right\}\begin{cases}\mathbf{u}_k^{\wp 1}\left(O_k\right)=\mathbf{O}_0\mathbf{O}_k=x_k\mathbf{x}_1+y_k\mathbf{y}_1\\ \boldsymbol{\omega}_k^{\wp 1}=\theta_k\,\mathbf{z}_0\end{cases}\qquad k=S,R,C \qquad (48)$$

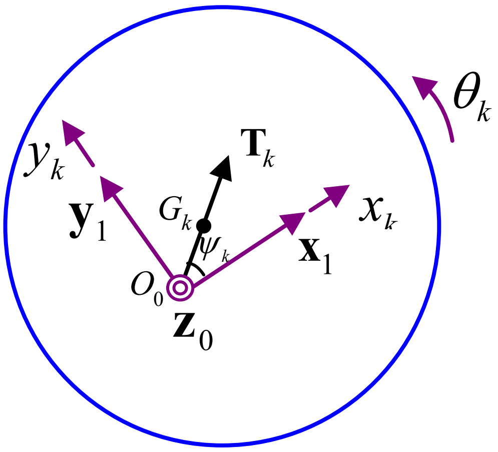

Figure 17 – Definition of sun-gear, ring-gear and carrier degrees of freedom

b) For planets, the translational DOFs in the screws of infinitesimal generalized displacements are attached to the sun-gear/planet #j centre line direction and its perpendicular direction (for a rigid system) (Figure 18) as:

$$\left\{S_j^{\wp j}\right\}\begin{cases}\mathbf{u}_j^{\wp j}\left(O_j\right)=\mathbf{O}_{j0}\mathbf{O}_j=x_j\mathbf{x}_j+y_j\mathbf{y}_j\\ \boldsymbol{\omega}_j^{\wp j}=\theta_j\,\mathbf{z}_0\end{cases}\qquad \text{planet \#j, j=1,…,N} \qquad (49)$$

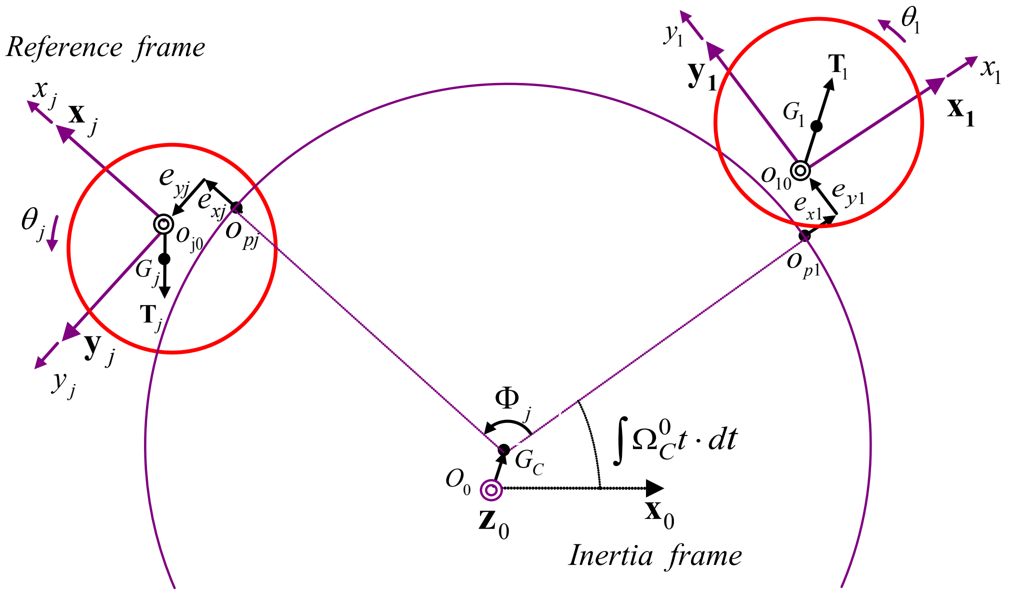

Figure 18 – Definition of planet degrees of freedom

The corresponding change of coordinate system diagrams between frames $\{S^{\wp 1}\}$, $\{S^{\wp j}\}$ and the inertial frame are shown in Figure 19.

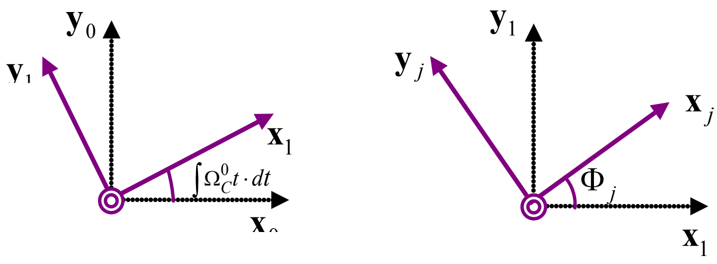

Figure 19 – Change of basis diagrams

6.2 – Equations of motion

6.2.1 – Mass matrix, combined with gyroscopic matrix, centrifugal matrix and forcing term vectors due to error and carrier rotation

a) Dynamic sum and moment for central members (Sun, Ring, Carrier, k=S, R, C) (Figure 20)

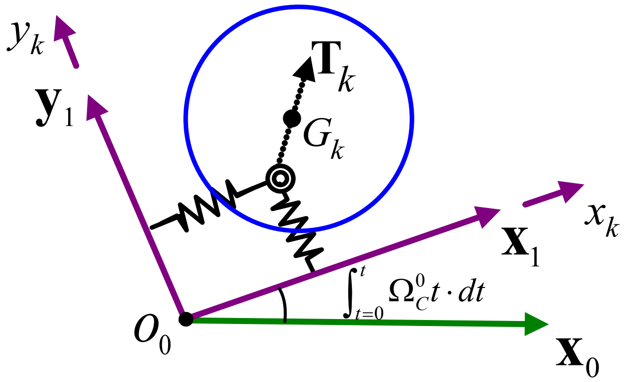

Figure 20 – Instantaneous position of sun-gear, ring-gear and carrier

Considering any central member *k* of the planetary gear set, the position of its centre of mass is defined by:

$$\mathbf{O}_0\mathbf{G}_k = x_k \mathbf{x}_1 + y_k \mathbf{y}_1 + e_k \mathbf{T}_k \tag{50}$$

from which, the velocity vector at the centre of mass are derived as:

$$\mathbf{V}_k^0\left(G_k\right) = \frac{d^0\left(\mathbf{O}_0\mathbf{G}_k\right)}{dt} = \left(\dot{x}_k - \Omega_C^0 y_k\right)\mathbf{x}_1 + \left(\dot{y}_k + \Omega_C^0 x_k\right)\mathbf{y}_1 + \Omega_C^0 e_k \mathbf{N}_k \tag{51}$$

The acceleration vector at the centre of mass is derived as:

$$\mathbf{J}_k^0\left(G_k\right) = \frac{d^0\left(\mathbf{V}_k^0\left(G_k\right)\right)}{dt} = \ddot{x}_k\mathbf{x}_1 + \ddot{y}_k\mathbf{y}_1 + 2\Omega_C^0\left(\dot{x}_k\mathbf{y}_1 - \dot{y}_k\mathbf{x}_1\right) - \left(\Omega_C^0\right)^2\left(x_k\mathbf{x}_1 + y_k\mathbf{y}_1\right) - \dot{\Omega}_C^0 y_k\mathbf{x}_1 + \dot{\Omega}_C^0 x_k\mathbf{y}_1 + \dot{\Omega}_C^0 e_k\mathbf{N}_k - \left(\Omega_C^0\right)^2 e_k\mathbf{T}_k \tag{52-a}$$

Noticing that the terms $-\dot{\Omega}_C^0 y_k\mathbf{x}_1 + \dot{\Omega}_C^0 x_k\mathbf{y}_1 + \dot{\Omega}_C^0 e_k\mathbf{N}_k$ can be neglected compared with the other terms in the acceleration, the following approximate expression can be obtained:

$$\mathbf{J}_k^0\left(G_k\right) = \frac{d^0\left(\mathbf{V}_k^0\left(G_k\right)\right)}{dt} \cong \ddot{x}_k\mathbf{x}_1 + \ddot{y}_k\mathbf{y}_1 + 2\Omega_C^0\left(\dot{x}_k\mathbf{y}_1 - \dot{y}_k\mathbf{x}_1\right) - \left(\Omega_C^0\right)^2\left(x_k\mathbf{x}_1 + y_k\mathbf{y}_1\right) - \left(\Omega_C^0\right)^2 e_k\mathbf{T}_k \tag{52-b}$$

The dynamic sum and moment at the centre of rotation are deduced as:

$$\mathbf{\Sigma}_k^0 = m_k \cdot \mathbf{J}_k^0\left(G_k\right) \tag{53}$$

$$\begin{aligned} \boldsymbol{\delta}_k^0(\mathrm{O}_k) &= \boldsymbol{\delta}_k^0(\mathrm{G}_k) + \mathbf{O}_k\mathbf{G}_k \times \Sigma_k^0 \\ &\cong \mathbf{I}_{G_k} \cdot \left(\ddot{\theta}_k + \dot{\Omega}_k^0\right)\mathbf{z}_{0,1} + m_k e_k\left(\cos\psi_k \cdot \ddot{y}_k - \sin\psi_k \cdot \ddot{x}_k\right)\mathbf{z}_{0,1} \quad k = C, S, R \end{aligned} \tag{54}$$

which can be rewritten in a matrix form as:

$$\begin{bmatrix} \Sigma_k^0 \\ \delta_k^0(O_k) \end{bmatrix} = \begin{bmatrix} m_k & & \\ & m_k & \\ -m_k e_k \sin\psi_k & m_k e_k \cos\psi_k & \mathrm{I}_{G_k} \end{bmatrix} \begin{Bmatrix} \ddot{x}_k \\ \ddot{y}_k \\ \ddot{\theta}_k \end{Bmatrix} + 2\Omega_C^0 \begin{bmatrix} 0 & -m_k & \\ m_k & 0 & \\ & & 0 \end{bmatrix} \begin{Bmatrix} \dot{x}_k \\ \dot{y}_k \\ \dot{\theta}_k \end{Bmatrix} - \left(\Omega_C^0\right)^2 \begin{bmatrix} m_k & & \\ & m_k & \\ & & 0 \end{bmatrix} \begin{Bmatrix} x_k \\ y_k \\ \theta_k \end{Bmatrix} - \begin{Bmatrix} m_k e_k \left(\Omega_C^0\right)^2 \cos\psi_k \\ m_k e_k \left(\Omega_C^0\right)^2 \sin\psi_k \\ -\mathbf{I}_{G_k} \cdot \dot{\Omega}_k^0 \end{Bmatrix} \tag{55}$$

with:

G_k : centre of mass of member k

$\mathbf{\Sigma}_k^0$: dynamic sum for member k

$\boldsymbol{\delta}_k^0(O_k)$: dynamic moment at point O_k for member k

m_k : mass of member k

$\mathbf{I}_{\mathrm{G}_k}$: polar moment of inertia of member k, $\mathbf{I}_{G_k} = \dfrac{m_k Rb_k^2}{2} \cdot \mathbf{z}_0$

b) Dynamic sum and moment for planets (Figure 21)

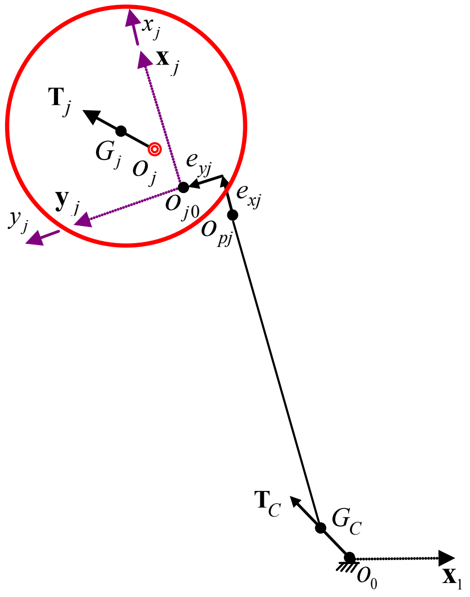

Figure 21 – Instantaneous position of planet #j

For planet #j, the instantaneous position of its centre of mass $\mathbf{G}_j$ is:

$$\begin{aligned} \mathbf{O}_0\mathbf{G}_j &= \mathbf{O}_0\mathbf{G}_C + \mathbf{G}_C\mathbf{O}_{pj} + \mathbf{O}_{pj}\mathbf{O}_{j0} + \mathbf{O}_{j0}\mathbf{O}_j + \mathbf{O}_j\mathbf{G}_j \\ &= e_C\mathbf{T}_C + R_C\mathbf{x}_j + e_{xj}\mathbf{x}_j + e_{yj}\mathbf{y}_j + x_j\mathbf{x}_j + y_j\mathbf{y}_j + e_j\mathbf{T}_j \end{aligned} \tag{56}$$

The velocity vector with respect to the inertial frame read:

$$\begin{aligned}\mathbf{V}_j^0\left(G_j\right) &= \frac{d^0\left(\mathbf{O}_0\mathbf{G}_j\right)}{dt} \\ &= \dot{x}_j\mathbf{x}_j + \Omega_C^0 x_j\mathbf{y}_j + \dot{y}_j\mathbf{y}_j - \Omega_C^0 y_j\mathbf{x}_j + \Omega_C^0 e_j\mathbf{N}_j + \Omega_C^0 e_C\mathbf{N}_C - \Omega_C^0 e_{yj}\mathbf{x}_j + \Omega_C^0\left(R_C + e_{xj}\right)\mathbf{y}_j\end{aligned} \tag{57}$$

The acceleration vector at the centre of mass is derived as:

$$\begin{aligned}\mathbf{J}_j^0\left(G_j\right) &= \frac{d^0\left(\mathbf{V}_j^0\left(G_j\right)\right)}{dt} \\ &= \ddot{x}_j\mathbf{x}_j + \ddot{y}_j\mathbf{y}_j + 2\Omega_C^0\left(\dot{x}_j\mathbf{y}_j - \dot{y}_j\mathbf{x}_j\right) + \dot{\Omega}_C^0\left(x_j\mathbf{y}_j - y_j\mathbf{x}_j - e_{yj}\mathbf{x}_j - \left(R_C + e_{xj}\right)\mathbf{y}_j + e_j\mathbf{N}_j + e_C\mathbf{N}_C\right) \\ &\quad - \left(\Omega_C^0\right)^2\left(x_j\mathbf{x}_j + y_j\mathbf{y}_j\right) - \left(\Omega_C^0\right)^2\left(e_j\mathbf{T}_j + e_C\mathbf{T}_C + e_{yj}\mathbf{y}_j + \left(R_C + e_{xj}\right)\mathbf{x}_j\right)\end{aligned}$$

(58-a)

As for the central members, the term $\dot{\Omega}_C^0\left(x_j\mathbf{y}_j - y_j\mathbf{x}_j - e_{yj}\mathbf{x}_j - e_{xj}\mathbf{y}_j + e_j\mathbf{N}_j + e_C\mathbf{N}_C\right)$ can be neglected compared with the other terms hence leading to:

$$\begin{aligned}\mathbf{J}_j^0\left(G_j\right) = \frac{d^0\left(\mathbf{V}_j^0\left(G_j\right)\right)}{dt} &\cong \ddot{x}_j\mathbf{x}_j + \ddot{y}_j\mathbf{y}_j + 2\Omega_C^0\left(\dot{x}_j\mathbf{y}_j - \dot{y}_j\mathbf{x}_j\right) - \dot{\Omega}_C^0 R_C\mathbf{y}_j - \left(\Omega_C^0\right)^2\left(x_j\mathbf{x}_j + y_j\mathbf{y}_j\right) \\ &\quad - \left(\Omega_C^0\right)^2\left(e_j\mathbf{T}_j + e_C\mathbf{T}_C + e_{yj}\mathbf{y}_j + \left(R_C + e_{xj}\right)\mathbf{x}_j\right)\end{aligned}$$

(58-b)

The dynamic sum and moment for planet #j are deduced as:

$$\boldsymbol{\Sigma}_j^0 = m_j \cdot \mathbf{J}_j^0\left(G_j\right) \tag{59}$$

$$\begin{aligned}\boldsymbol{\delta}_j^0(\mathrm{O}_j) &= \boldsymbol{\delta}_j^0(\mathrm{G}_j) + \mathbf{O}_j\mathbf{G}\boldsymbol{\Sigma}_j \times {}^{0}_{j} \\ &= \mathbf{I}_{\mathrm{G}_j} \cdot \left(\ddot{\theta}_j + \dot{\Omega}_j^0\right)\mathbf{z}_{0,j} + m_j e_j\left(\cos\psi_j \cdot \ddot{y}_j + \sin\psi_j R_C \cdot \left(\Omega_C^0\right)^2 - \sin\psi_j \ddot{x}_j\right)\mathbf{z}_{0,j}\end{aligned} \tag{60}$$

or in a matrix form:

$$\begin{bmatrix}\Sigma_j^0 \\ \delta_j^0(O_j)\end{bmatrix} = \begin{bmatrix} m_j & & \\ & m_j & \\ -m_j e_j \sin\psi_j & m_j e_j \cos\psi_j & \mathrm{I}_{G_j}\end{bmatrix}\begin{Bmatrix}\ddot{x}_j \\ \ddot{y}_j \\ \ddot{\theta}_j\end{Bmatrix} + 2\Omega_C^0\begin{bmatrix}0 & -m_j & \\ m_j & 0 & \\ & & 0\end{bmatrix}\begin{Bmatrix}\dot{x}_j \\ \dot{y}_j \\ \dot{\theta}_j\end{Bmatrix} - \left(\Omega_C^0\right)^2\begin{bmatrix}m_j & & \\ & m_j & \\ & & 0\end{bmatrix}\begin{Bmatrix}x_j \\ y_j \\ \theta_j\end{Bmatrix}$$

$$-\left\{\begin{array}{l} m_j\left(\Omega_C^0\right)^2\left(e_C\cos(\psi_C-\varepsilon_S\Phi_j)+R_C+e_{xj}+e_j\cos\psi_j\right) \\ m_j\left(\Omega_C^0\right)^2\left(e_C\sin(\psi_C-\varepsilon_S\Phi_j)+e_{yj}+e_j\sin\psi_j\right)+m_jR_C\cdot\dot{\Omega}_C^0 \\ -\mathbf{I}_{G_j}\cdot\dot{\Omega}_j^0-m_je_j\sin\psi_jR_C\cdot\left(\Omega_C^0\right)^2 \end{array}\right\} \tag{61}$$

with:

G_j : centre of mass of member j

$\mathbf{\Sigma}_j^0$: dynamic sum for member j

$\boldsymbol{\delta}_j^0(O_j)$: dynamic moment at point O_j for member j

m_j : mass of member j

$\mathbf{I}_{G_j}$: polar moment of inertia of member j, $\mathbf{I}_{G_j}=\dfrac{m_jRb_j^2}{2}\cdot\mathbf{z}_0$

6.2.2 Mesh stiffness matrix

a) Tooth deflections

The following hypotheses have been used:

- The gears (including the ring-gear) are assimilated to rigid cylinders connected by an elastic link.
- Deflections are small quantities.
- Off-line-of-action contacts between non conjugated profiles are not considered.
- The contact are fully lubricated so that friction forces can be neglected compared with the normal forces on the tooth contacts.

In such conditions, the displacements of each member can be described via screws $\left\{S^{\wp}\right\}$ of infinitesimal generalized displacements from which the deflections at the potential points of contact can be derived by using the shifting property of screw moments. Using a rigid-body model, the normal approach at every potential point of contact reads (Figure 22):

for sun-gear / planet #j at the potential point of contact M_{Sj}'

$$\begin{aligned}
\delta(M_{Sj}') &= \mathbf{u}_j^S\left(M_{Sj}'\right)\cdot\mathbf{n}_j' \\
&= \left(\mathbf{u}_S^{\wp 1}\left(O_S\right)+\boldsymbol{\omega}_S^{\wp 1}\times\mathbf{O}_S\mathbf{M}_{Sj}\right)\cdot\mathbf{n}_j' - \left(\mathbf{u}_j^{\wp j}\left(O_j\right)+\boldsymbol{\omega}_j^{\wp j}\times\mathbf{O}_j\mathbf{M}_{Sj}\right)\cdot\mathbf{n}_j' \\
&= \begin{bmatrix} \begin{Bmatrix} \mathbf{n}_j' \\ \mathbf{O}_S\mathbf{M}_{Sj}\times\mathbf{n}_j' \end{Bmatrix} \\ \begin{Bmatrix} -\mathbf{n}_j' \\ -\mathbf{O}_j\mathbf{M}_{Sj}\times\mathbf{n}_j' \end{Bmatrix} \end{bmatrix} \cdot \begin{bmatrix} \begin{Bmatrix} \mathbf{u}_S^{\wp 1}\left(O_S\right) \\ \boldsymbol{\omega}_S^{\wp 1} \end{Bmatrix} \\ \begin{Bmatrix} \mathbf{u}_j^{\wp j}\left(O_j\right) \\ \boldsymbol{\omega}_j^{\wp j} \end{Bmatrix} \end{bmatrix} = \mathbf{V}_{Sj}\left(M_{Sj}'\right)^T\mathbf{X}_{Sj}
\end{aligned} \tag{62-a}$$

for ring-gear / planet #j at the potential point of contact M_{Rj}'*:*

$$\begin{aligned}
\delta(M_{Rj}') &= \mathbf{u}_j^R\left(M_{Rj}'\right)\cdot\mathbf{n}_j^{*}{}' \\
&= \left(\mathbf{u}_j^{\wp j}\left(O_j\right)+\boldsymbol{\omega}_j^{\wp j}\times\mathbf{n}_j\mathrm{M}_{Rj}\right)\cdot\mathbf{n}_j^{*}{}' - \left(\mathbf{u}_R^{\wp 1}\left(O_R\right)+\boldsymbol{\omega}_R^{\wp 1}\times\mathbf{n}_R\mathrm{M}_{Rj}\right)\cdot\mathbf{n}_j^{*}{}' \\
&= \mathbf{V}_{Rj}\left(M_{Rj}'\right)^T\mathbf{X}_{Rj}
\end{aligned} \tag{62-b}$$

where $\mathbf{n}_j^{(*)}{}'$ represents the outward unit normal vector relative to sun-gear tooth flank and planet #j tooth flank respectively,

$$\mathbf{V}(M_{Sj}') = \cos\beta_b \begin{bmatrix} \begin{Bmatrix} \sin\rho_S' \\ \varepsilon_S\cos\rho_S' \\ \varepsilon_S e_S\cos\sigma_S' + \varepsilon_S Rb_S \end{Bmatrix}_{(\mathbf{x}_1,\mathbf{y}_1,\mathbf{z}_0)} \\ \begin{Bmatrix} -\sin\alpha_{Sj}' \\ -\varepsilon_S\cos\alpha_{Sj}' \\ -\varepsilon_S e_j\cos\sigma_j' + \varepsilon_S Rb_j \end{Bmatrix}_{(\mathbf{x}_j,\mathbf{y}_j,\mathbf{z}_0)} \end{bmatrix} \qquad \mathbf{X}_{Sj} = \begin{bmatrix} \begin{Bmatrix} x_S \\ y_S \\ \theta_S \end{Bmatrix}_{(\mathbf{x}_1,\mathbf{y}_1,\mathbf{z}_0)} \\ \begin{Bmatrix} x_j \\ y_j \\ \theta_j \end{Bmatrix}_{(\mathbf{x}_j,\mathbf{y}_j,\mathbf{z}_0)} \end{bmatrix} \tag{63-a}$$

$$\rho_S' = \alpha_{Sj}' - \varepsilon_S\Phi_{Sj}'; \quad \sigma_S' = \alpha_{Sj}' - \varepsilon_S\Phi_{Sj}' + \varepsilon_S\psi_S; \quad \sigma_j = \alpha_{Sj} + \varepsilon_S\psi_j$$

$$\mathbf{V}(M_{Rj}') = \cos\beta_b \begin{bmatrix} \begin{Bmatrix} -\sin\rho_R' \\ \varepsilon_S\cos\rho_R' \\ \varepsilon_S e_R\cos\sigma_R' + \varepsilon_S Rb_R \end{Bmatrix}_{(\mathbf{x}_1,\mathbf{y}_1,\mathbf{z}_0)} \\ \begin{Bmatrix} \sin\alpha_{Rj}' \\ -\varepsilon_S\cos\alpha_{Rj}' \\ -\varepsilon_S e_j\cos\sigma_j^{*}{}' - \varepsilon_S Rb_j \end{Bmatrix}_{(\mathbf{x}_j,\mathbf{y}_j,\mathbf{z}_0)} \end{bmatrix} \qquad \mathbf{X}_{Rj} = \begin{bmatrix} \begin{Bmatrix} x_R \\ y_R \\ \theta_R \end{Bmatrix}_{(\mathbf{x}_1,\mathbf{y}_1,\mathbf{z}_0)} \\ \begin{Bmatrix} x_j \\ y_j \\ \theta_j \end{Bmatrix}_{(\mathbf{x}_j,\mathbf{y}_j,\mathbf{z}_0)} \end{bmatrix} \tag{63-b}$$

$$\rho_R' = \alpha_{Rj}' + \varepsilon_S\Phi_{Rj}' \quad \sigma_R' = \alpha_{Rj}' + \varepsilon_S\Phi_{Rj}' - \varepsilon_S\psi_R \quad \sigma_j^{*} = \alpha_{Rj} - \varepsilon_S\psi_j$$

with:

β_b : base helix angle

p_{ba} : apparent base pitch

b : face width of tooth

$\varepsilon_S = 1 \; or \; -1$: depending on the sense of rotation of the sun-gear (+1: counter-clockwise, -1: clockwise)

NB: It is to be noted that the structural vectors $\mathbf{V}(M_{gj}')$ *are dependent on the degrees-of-freedom* $\mathbf{X}_{gj}$ *and on time.*

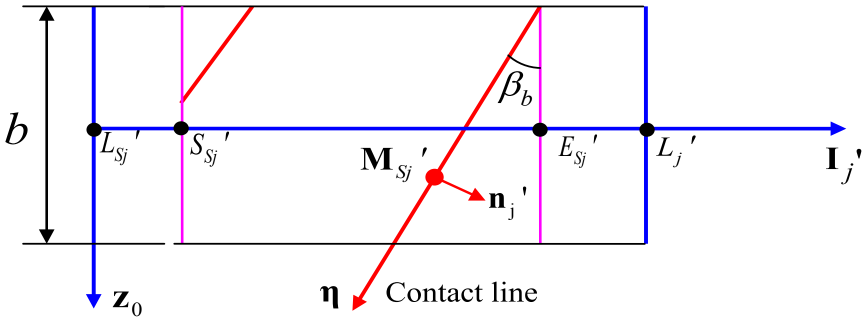

Figure 22-a – Tangential plane of sun-gear/planet #j mesh

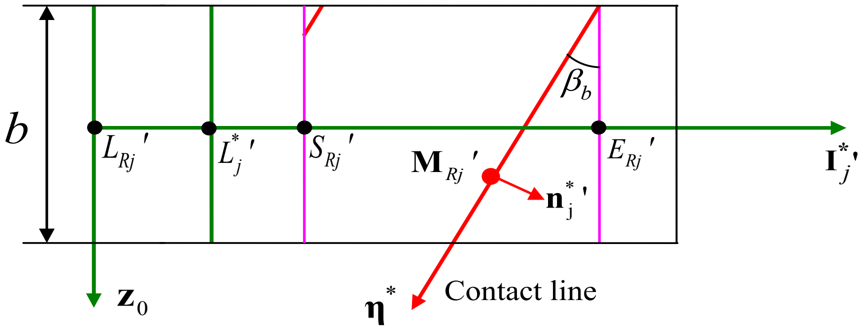

Figure 22-b – Tangential plane of planet #j/ring-gear mesh

Figure 22 – Parameter definition in tangent planes for sun(ring)-gear/planet #j meshes($\boldsymbol{\eta}, \boldsymbol{\eta}^*$: *direction of contact lines)*

The contact deflection at every potential point of contact is therefore deduced as the interpenetration of the parts, i. e., the normal approach with respect to rigid-body positions

$\delta(M_{Sj}')$ or $\delta(M_{Rj}')$ minus the initial gap (possibly generated by errors or tooth shape modifications) denoted $\delta e(M_{gj}')$ thus leading to the formula:

$$\Delta(M_{gj}') = \delta(M_{gj}') - \delta e(M_{gj}') \tag{64}$$

b) Mesh stiffness matrix and forcing terms caused by initial separations

Contact losses between the teeth may appear due to large dynamic displacements (of the same order of magnitude as static displacements) and assembly errors which imply, from a mathematical viewpoint, that the contact deflection becomes negative and that the local mesh stiffness drops to zero. This nonlinearity is formally incorporated in the mesh stiffness definition via the Heaviside step function under the form:

$$k_{gj}(t,\mathbf{X}) = H(\Delta(M_{gj}')) \cdot \hat{k}_{gj}(t,\mathbf{X}) \tag{65}$$

$$\text{where } H(\Delta(M_{gj}')) = \begin{cases} 1\,, \Delta(M_{gj}') > 0 \\ 0\,, \Delta(M_{gj}') < 0 \end{cases}$$

and $\hat{k}(t,\mathbf{X}_{gj})$ is the nonlinear time-varying mesh stiffness function calculated as described in the second part of this chapter.

Neglecting viscous force contributions, the mesh force vector for sun-gear / planet #j at the potential point of contact M_{Sj}' is expressed as:

$$\begin{aligned} \{F_{S/j}\} &\begin{cases} \mathbf{F}_{S/j} = k_{Sj}(t,\mathbf{X})\Delta(M_{Sj}')\cdot\mathbf{n}_j' \\ \mathbf{M}_{S/j}(O_S) = k_{Sj}(t,\mathbf{X})\Delta(M_{Sj}')\mathbf{O}_S\mathbf{M}_{Sj}'\times\mathbf{n}_j' \end{cases} \\ \{F_{j/S}\} &\begin{cases} \mathbf{F}_{j/g} = -k_{Sj}(t,\mathbf{X})\Delta(M_{Sj}')\cdot\mathbf{n}_j' \\ \mathbf{M}_{j/S}(O_j) = -k_{Sj}(t,\mathbf{X})\Delta(M_{Sj}')\mathbf{O}_j\mathbf{M}_{Sj}'\times\mathbf{n}_j' \end{cases} \end{aligned} \tag{66}$$

Using similar developments for ring-gear / planet #*j*, and finally, the following expression is obtained:

$$\begin{aligned}\begin{bmatrix}\left\{F_{g/j}\right\}\\ \left\{F_{j/g}\right\}\end{bmatrix} &= k_{gj}\left(t,\mathbf{X}\right)\Delta\left(M_{gj}'\right)\mathbf{V}\left(M_{gj}'\right)\\ &= k_{gj}\left(t,\mathbf{X}\right)\mathbf{V}\left(M_{gj}'\right)\mathbf{V}\left(M_{gj}'\right)^{T}\mathbf{X}_{gj} - k_{gj}\left(t,\mathbf{X}\right)\delta e\left(M_{gj}'\right)\mathbf{V}\left(M_{gj}'\right)\\ &= \begin{bmatrix}\mathbf{K}_{g/j} & \mathbf{K}_{g\&j}\\ sym & \mathbf{K}_{j/g}\end{bmatrix}\begin{bmatrix}\mathbf{X}_{g}\\ \mathbf{X}_{j}\end{bmatrix} - \begin{bmatrix}\mathbf{fe}_{g/j}\\ \mathbf{fe}_{j/g}\end{bmatrix} \quad g=S,R\end{aligned} \tag{67}$$

leading to the following global stiffness matrix and forcing term vector:

$$\mathbf{K_G}\left(\mathrm{t},\mathbf{X}\right)=\begin{bmatrix}\sum_{\mathrm{j=1}}^{\mathrm{N}}\mathrm{K}_{\mathrm{S/j}} & 0 & \mathrm{K}_{\mathrm{S\&1}} & \cdots & \mathrm{K}_{\mathrm{S\&N}}\\ & \sum_{\mathrm{j=1}}^{\mathrm{N}}\mathrm{K}_{\mathrm{R/j}} & \mathrm{K}_{\mathrm{R\&1}} & \cdots & \mathrm{K}_{\mathrm{R\&N}}\\ & & \sum_{\mathrm{g=S,R}}\mathrm{K}_{\mathrm{1/g}} & \cdots & 0\\ \mathrm{symmetry} & & & \ddots & 0\\ & & & & \sum_{\mathrm{g=S,R}}\mathrm{K}_{\mathrm{N/g}}\end{bmatrix},\ \mathbf{F_{KE}}\left(\mathrm{t},\mathbf{X}\right)=\begin{bmatrix}\sum_{\mathrm{j=1}}^{\mathrm{N}}\mathrm{fe}_{\mathrm{S/j}}\\ \sum_{\mathrm{j=1}}^{\mathrm{N}}\mathrm{fe}_{\mathrm{R/j}}\\ \sum_{\mathrm{g=S,R}}\mathrm{fe}_{\mathrm{1/g}}\\ \cdots\\ \sum_{\mathrm{g=S,R}}\mathrm{fe}_{\mathrm{N/g}}\end{bmatrix} \tag{68}$$

with:

$\mathbf{X}_{gj}=\left\{x_g,y_g,\theta_g,x_j,y_j,\theta_j\right\}^T$ $g=S,R$: DOFs of sun (ring)-gear and planet j

$\mathbf{K_G}\left(\mathrm{t},\mathbf{X}\right)$: time-varying non-linear mesh stiffness matrix

$\mathbf{F_{KE}}\left(\mathrm{t},\mathbf{X}\right)$: time-varying non-linear internal excited force due to eccentricity and position errors.

6.2.3 – Bearing stiffness matrices

a) Bearing stiffness matrix for central members (carrier, sun-gear and ring-gear)

A simplified expression is used by keeping direct stiffness components only so that the bearing stiffness matrix for the central members (sun-gear, ring-gear and carrier) reduces to:

$$\left[\mathbf{K}_{k\,b}\right]=\mathrm{diag}\ (k_{kx},k_{ky},Rb_k{}^2\cdot k_{k\theta})\ \text{, k=C, S, R} \tag{69}$$

with:

$k_{kx},k_{ky},k_{k\theta}$: bearing stiffness in two translational directions and one rotational direction (torsion).

b) Bearing stiffness matrix for carrier pin-planet (Figure 23)

For the sake of simplicity, the carrier pin-planet assembly is supposed to be isotropic. Using a rigid-body model, the normal approach at point O_j in $\mathbf{x}_j$ direction and in $\mathbf{y}_j$ direction read (Figure 23):

$$\begin{aligned}\delta(O_j)_{\mathbf{x}_j} &= \mathbf{u}_1^C\left(O_j\right)\cdot\mathbf{x}_j = \left(\mathbf{u}_C^{\wp 1}\left(O_C\right)+\boldsymbol{\omega}_C^{\wp 1}\times\mathbf{O}_C\mathbf{O}_j-\mathbf{u}_j^{\wp j}\left(O_j\right)\right)\cdot\mathbf{x}_j = \mathbf{V}_{Cjx}\left(O_j\right)^T\mathbf{X}_{Cj}\\ \delta(O_j)_{\mathbf{y}_j} &= \mathbf{u}_1^C\left(O_j\right)\cdot\mathbf{y}_j = \left(\mathbf{u}_C^{\wp 1}\left(O_C\right)+\boldsymbol{\omega}_C^{\wp 1}\times\mathbf{O}_C\mathbf{O}_j-\mathbf{u}_j^{\wp j}\left(O_j\right)\right)\cdot\mathbf{y}_j = \mathbf{V}_{Cjy}\left(O_j\right)^T\mathbf{X}_{Cj}\end{aligned} \tag{70}$$

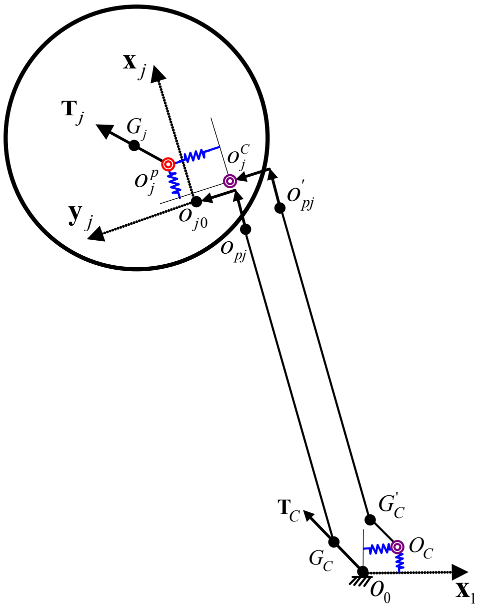

Figure 23 – Deflections of carrier pin/planet #j

(Point O_j^p corresponding to point O_j on planet #j, O_j^C corresponding to point O_j on the carrier)

Neglecting viscous force contributions, the corresponding restoring force for carrier-planet #*j* is expressed as:

$$\begin{aligned}\begin{bmatrix}\left\{F_{C/j}\right\}\\ \left\{F_{j/C}\right\}\end{bmatrix}_{\mathbf{x}_j} &= k_{bp}\delta(O_j)_{\mathbf{x}_j}\mathbf{V}_{Cjx}\left(O_j\right) = k_{bp}\mathbf{V}_{Cjx}\left(O_j\right)\mathbf{V}_{Cjx}\left(O_j\right)^T\mathbf{X}_{Cj}\\ \begin{bmatrix}\left\{F_{C/j}\right\}\\ \left\{F_{j/C}\right\}\end{bmatrix}_{\mathbf{y}_j} &= k_{bp}\delta(O_j)_{\mathbf{y}_j}\mathbf{V}_{Cjx}\left(O_j\right) = k_{bp}\mathbf{V}_{Cjy}\left(O_j\right)\mathbf{V}_{Cjy}\left(O_j\right)^T\mathbf{X}_{Cj}\\ \begin{bmatrix}\left\{F_{C/j}\right\}\\ \left\{F_{j/C}\right\}\end{bmatrix}_{\mathbf{x}_j} &+ \begin{bmatrix}\left\{F_{C/j}\right\}\\ \left\{F_{j/C}\right\}\end{bmatrix}_{\mathbf{y}_j} = \left[\mathbf{K}_{Cj}\right]\mathbf{X}_{Cj}\end{aligned} \tag{71}$$

Developing $\left[\mathbf{K}_{Cj}\right]$ leads to:

$$\left[\mathbf{K}_{Cj}\right]=\begin{bmatrix} \mathrm{K}_{C/j} & \mathrm{K}_{C\&j} \\ sym & \mathrm{K}_{j/C} \end{bmatrix}=k_{bp}\begin{bmatrix} 1 & 0 & -R_C\sin\Phi_j & -\cos\Phi_j & \sin\Phi_j & 0 \\ & 1 & R_C\cos\Phi_j & -\sin\Phi_j & -\cos\Phi_j & 0 \\ & & {R_C}^2 & 0 & -R_C & 0 \\ & & & 1 & 0 & 0 \\ & & sym & & 1 & 0 \\ & & & & & 0 \end{bmatrix} \tag{72}$$

with:

$\mathbf{u}_C^{\wp 1}\left(O_j\right),\mathbf{u}_j^{\wp j}\left(O_j\right)$: infinitesimal translations of point O_j on carrier pin and on planet #j

$\mathbf{V}_{Cjx}\left(O_j\right)=\left\{\cos\Phi_j,\sin\Phi_j,0,-1,0,0\right\}^T$: bearing structural vector in $\mathbf{x}_j$ direction

$\mathbf{V}_{Cjy}\left(O_j\right)=\left\{-\sin\Phi_j,\cos\Phi_j,R_C,0,-1,0\right\}^T$: bearing structural vector in $\mathbf{y}_j$ direction

$\mathbf{X}_{Cj}=\left\{x_C,y_C,\theta_C,x_j,y_j,\theta_j\right\}^T$: DOFs of carrier and planet j

$\left[\mathbf{K}_{Cj}\right]$: bearing stiffness matrix between carrier pin and planet #j

The total bearing stiffness matrix $\left[\mathbf{K}_\mathrm{b}(\mathrm{t},\mathrm{x})\right]$ comprises all the bearing stiffness matrices of all central members Eq. (69), and the bearing stiffness matrices associated with all the carrier pin-planet supports Eq. (72). It can be expressed as:

$$\left[\mathbf{K}_\mathrm{b}(\mathrm{t},\mathrm{x})\right]\begin{bmatrix} \mathbf{K}_\mathrm{Cb}+\sum_{\mathrm{j=1}}^{\mathrm{N}}\mathrm{K}_{\mathrm{C/j}} & 0 & 0 & \mathrm{K}_{\mathrm{C\&1}} & \cdots\ \mathrm{K}_{\mathrm{C\&j}} & \cdots & \mathrm{K}_{\mathrm{C\&N}} \\ & \mathbf{K}_\mathrm{Sb} & 0 & 0 & \cdots\ 0 & \cdots & 0 \\ & & \mathbf{K}_\mathrm{Rb} & 0 & \cdots\ 0 & \cdots & 0 \\ \mathrm{sym} & & & \mathrm{K}_{\mathrm{1/C}} & \cdots\ 0 & \cdots & 0 \\ & & & & \ddots\ 0 & \cdots & 0 \\ & & & & \mathrm{K}_{\mathrm{j/C}} & \cdots & 0 \\ & & & & & \ddots & 0 \\ & & & & & & \mathrm{K}_{\mathrm{N/C}} \end{bmatrix} \tag{73}$$

6.2.4 – Damping matrix

The mechanisms controlling the energy dissipation in geared systems are complex and the quantification of damping remains a challenging issue. For the sake of simplicity, the classic method known as Rayleigh's damping have been used in this work. A viscous damping matrix is therefore sought as a linear combination of the mass and time-averaged stiffness matrices of the form:

$$[C] = \alpha[\mathbf{M}] + \beta[\bar{\mathbf{K}}] \tag{74}$$

with:

$[\mathrm{M}]$, $[\bar{\mathbf{K}}]$: mass matrix and average stiffness matrix

α , β : Rayleigh's damping coefficients

The two coefficients are unknown but they can be identified if the damping factors at two different eigenfrequencies are given (measured) since it is possible to write in the (pseudo)-modal basis:

$$\alpha \cdot m_{\Phi i} + \beta \cdot k_{\Phi i} = 2\varepsilon_{\Phi i} m_{\Phi i} \omega_{\Phi i} \tag{75}$$

with:

$m_{\Phi i} = \Phi_i^T \left[\mathbf{M}\right] \Phi_i$, modal mass

$k_{\Phi i} = \Phi_i^T \left[\mathbf{K}\right] \Phi_i$, modal stiffness

As far as gears are concerned and based on the results in the literature, a damping factor ranging between 0.03 and 0.07 seems representative of the actual dissipation levels and has been introduced for the eigenfrequencies with the largest and smallest percentages of modal strain energy stored in the tooth meshes.

For any mode-shape $\{\Phi_i\}$, the percentage of modal strain energy stored in the j^{th} mesh teeth pair is:

$$\rho_{ij} = \frac{\{\Phi_i\}^T \cdot \left[\bar{K}_j\right] \cdot \{\Phi_i\}}{\{\Phi_i\}^T \cdot \left[\bar{K}\right] \cdot \{\Phi_i\}} \quad for\ i = 1, \ldots, n \tag{76}$$

with:

$\{\Phi_i\}$: the i^{th} modal vector

$\{\bar{K}\}$: average stiffness matrix

$\{\bar{K}_j\}$: stiffness matrix for the j^{th} mesh

6.2.5 – Equations of motion of planetary gear sets

The assembly of all the elementary matrices leads to the following equations of motion which point to a parametrically excited, possibly non-linear, differential system with gyroscopic and centrifugal terms in the case of a rotating carrier:

$$\mathbf{M}\ddot{\mathbf{X}}+\left(2\Omega_C\mathbf{D}+\mathbf{C}\right)\dot{\mathbf{X}}+\left(\mathbf{K_b}+\mathbf{K_G}\left(t,\mathbf{X}\right)+\Omega_C^2\mathbf{L}\right)\mathbf{X}=\mathbf{F_0}+\mathbf{F}_{\dot{\boldsymbol{\Omega}}}\left(t\right)+\mathbf{F_{KE}}\left(t,X\right) \qquad (77)$$

with:

- $\mathbf{X}=\left\{x_C,y_C,\theta_C,x_R,y_R,\theta_R,x_S,y_S,\theta_S,x_1,y_1,\theta_1,...,x_N,y_N,\theta_N\right\}^T$ is the total DOF vector ($3N+9$ components, N is the number of planets)
- $\mathbf{M},\mathbf{C},\mathbf{K_b}$ are the global (constant) mass, damping (proportional damping is assumed) and bearing-shaft stiffness matrices
- $2\Omega_C\mathbf{D},\Omega_C^2\mathbf{L}$ represent the gyroscopic matrix and centrifugal stiffness matrix result from carrier rotation
- $\mathbf{K_G}\left(t,\mathbf{X}\right)$ accounts for all the simultaneous mesh stiffness for all the meshes, the matrix is time-varying on account of the contact length evolutions during the rotation of the gears and possibly non-linear because of the dynamic contact conditions
- $\mathbf{F_0},\mathbf{F}_{\dot{\boldsymbol{\Omega}}}\left(t\right),\mathbf{F_{KE}}\left(t,X\right)$ are the static load vector (torques), the inertial forcing terms due to unsteady rotational speeds and the elastic contributions caused by initial gaps between the teeth.

The corresponding matrices are:

$$\mathbf{M}_i=\begin{bmatrix} m_i & & \\ & m_i & \\ -m_ie_i\sin\psi_i & m_ie_i\cos\psi_i & \mathrm{I}_{G_i}\end{bmatrix};\ \mathbf{D}_i=\begin{bmatrix} 0 & -m_i & \\ m_i & 0 & \\ & & 0\end{bmatrix};\ \mathbf{L}_i=\begin{bmatrix} m_i & & \\ & m_i & \\ & & 0\end{bmatrix};$$

$$\mathbf{F}_{0i}=\begin{Bmatrix}0\\0\\T_i\end{Bmatrix},T_C=T_R=T_1=,...,T_N=0;T_S=const\ ;\ i=C,R,S,1...N$$

$$\mathbf{F}_{\dot{\Omega}\mathrm{k}}\left(\mathrm{t}\right)=\begin{Bmatrix} m_ke_k\left(\Omega_k^0\right)^2\cos\psi_k\\ m_ke_k\left(\Omega_k^0\right)^2\sin\psi_k\\ -\mathbf{I}_{G_k}\cdot\dot{\Omega}_k^0\end{Bmatrix};\ \mathbf{F}_{\dot{\Omega}\mathrm{j}}\left(\mathrm{t}\right)=\begin{Bmatrix} m_j\left(\Omega_C^0\right)^2\left(e_C\cos\left(\psi_C-\varepsilon_S\Phi_j\right)+R_C+e_{xj}\right)+m_je_j\left(\Omega_j^0\right)^2\cos\psi_j\\ m_j\left(\Omega_C^0\right)^2\left(e_C\sin\left(\psi_C-\varepsilon_S\Phi_j\right)+e_{yj}\right)+m_je_j\left(\Omega_j^0\right)^2\sin\psi_j+m_jR_C\cdot\dot{\Omega}_C^0\\ -\mathbf{I}_{G_j}\cdot\dot{\Omega}_j^0-m_je_j\sin\psi_jR_C\cdot\left(\Omega_C^0\right)^2\end{Bmatrix}$$

$$k=C,R,S\ ;\ j=1,...,N$$

$$\mathrm{M}=\mathrm{diag}([\mathbf{M}_{\mathrm{C}},\mathbf{M}_{\mathrm{R}},\mathbf{M}_{\mathrm{S}},\mathbf{M}_{1},\ldots,\mathbf{M}_{\mathrm{N}}]);\ \mathrm{D}=\mathrm{diag}([\mathbf{D}_{\mathrm{C}},\mathbf{D}_{\mathrm{R}},\mathbf{D}_{\mathrm{S}},\mathbf{D}_{1},\ldots,\mathbf{D}_{\mathrm{N}}]);\ \mathrm{L}=\mathrm{diag}([\mathbf{L}_{\mathrm{C}},\mathbf{L}_{\mathrm{R}},\mathbf{L}_{\mathrm{S}},\mathbf{L}_{1},\ldots,\mathbf{L}_{\mathrm{N}}]);$$

$$\mathbf{F}_0=\left\{\mathbf{F}_{0\mathrm{C}},\mathbf{F}_{0\mathrm{R}},\mathbf{F}_{0\mathrm{S}},\mathbf{F}_{01},\ldots,\mathbf{F}_{0\mathrm{N}}\right\}^T;\ \mathbf{F}_{\dot{\Omega}}(\mathrm{t})=\left\{\mathbf{F}_{\dot{\Omega}\mathrm{C}}(\mathrm{t}),\mathbf{F}_{\dot{\Omega}\mathrm{R}}(\mathrm{t}),\mathbf{F}_{\dot{\Omega}\mathrm{S}}(\mathrm{t}),\mathbf{F}_{\dot{\Omega}1}(\mathrm{t}),\ldots,\mathbf{F}_{\dot{\Omega}\mathrm{N}}(\mathrm{t})\right\}^T\ ;$$

$$\mathbf{K}_{\mathrm{G}}(\mathrm{t},\mathbf{X})=\begin{bmatrix}\sum_{j=1}^{N}\mathrm{K}_{\mathrm{S/j}} & 0 & \mathrm{K}_{\mathrm{S\&1}} & \cdots & \mathrm{K}_{\mathrm{S\&N}}\\ & \sum_{j=1}^{N}\mathrm{K}_{\mathrm{R/j}} & \mathrm{K}_{\mathrm{R\&1}} & \cdots & \mathrm{K}_{\mathrm{R\&N}}\\ & & \sum_{g=S,R}\mathrm{K}_{1/g} & \cdots & 0\\ \text{symmetry} & & & \ddots & 0\\ & & & & \sum_{g=S,R}\mathrm{K}_{\mathrm{N/g}}\end{bmatrix},\ \mathbf{F}_{\mathrm{KE}}(\mathrm{t})=\begin{bmatrix}\sum_{j=1}^{N}\mathrm{fe}_{\mathrm{S/j}}\\ \sum_{j=1}^{N}\mathrm{fe}_{\mathrm{R/j}}\\ \sum_{g=S,R}\mathrm{fe}_{1/g}\\ \cdots\\ \sum_{g=S,R}\mathrm{fe}_{\mathrm{N/g}}\end{bmatrix}$$

$$\mathbf{K}_{\mathrm{b}}(\mathrm{t},\mathrm{x})=\begin{bmatrix}\mathbf{K}_{\mathrm{Cb}}+\sum_{j=1}^{N}\mathrm{K}_{\mathrm{C/j}} & 0 & 0 & \mathrm{K}_{\mathrm{C\&1}} & \cdots\ \mathrm{K}_{\mathrm{C\&j}} & \cdots & \mathrm{K}_{\mathrm{C\&N}}\\ & \mathbf{K}_{\mathrm{Sb}} & 0 & 0 & \cdots\ 0 & \cdots & 0\\ & & \mathbf{K}_{\mathrm{Rb}} & 0 & \cdots\ 0 & \cdots & 0\\ & \text{sym} & & \mathrm{K}_{1/\mathrm{C}} & \cdots\ 0 & \cdots & 0\\ & & & & \ddots\ 0 & \cdots & 0\\ & & & & \mathrm{K}_{\mathrm{j/C}} & \cdots & 0\\ & & & & & \ddots & 0\\ & & & & & & \mathrm{K}_{\mathrm{N/C}}\end{bmatrix};$$

$$\mathrm{K}_{\mathrm{C/j}}=\begin{bmatrix}1 & 0 & -R_C\sin\Phi_j\\ & 1 & R_C\cos\Phi_j\\ & & R_C^{\ 2}\end{bmatrix};\mathrm{K}_{\mathrm{C\&j}}=\begin{bmatrix}-\cos\Phi_j & \sin\Phi_j & 0\\ -\sin\Phi_j & -\cos\Phi_j & 0\\ 0 & -R_C & 0\end{bmatrix};\mathrm{K}_{\mathrm{j/C}}=\begin{bmatrix}1 & 0 & 0\\ & 1 & 0\\ & & 1\end{bmatrix};\mathbf{K}_{\mathrm{kb}}=\begin{bmatrix}k_{kx} & & \\ & k_{ky} & \\ & & Rb_k^{\ 2}\cdot k_{k\theta}\end{bmatrix}\tag{78}$$

6.3 – Numerical solution

The links between the DOFs, errors, mesh geometry and stiffness generate non-linearities superimposed on the parametric excitations caused by the (naturally) time-varying mesh stiffness and the possible contact losses and shocks. Moreover, the frequency and amplitude modulations lead to longer characteristic periods which necessitate a large number of time steps in order to be accurate on both the low- and high-frequency phenomena. The equations of motion are solved by using: i) the unconditionally stable and convergent Newmark's time-step integration scheme (Appendix 1), ii) a fixed-point method with relaxation in order to update geometry and mesh characteristics in a controlled way along with iii) a unilateral contact algorithm (mesh stiffness is set to zero if the contact deformation is negative or nil).

The corresponding numerical simulation process is represented in the following flow chart.

Table 2 – Simulation flow chart

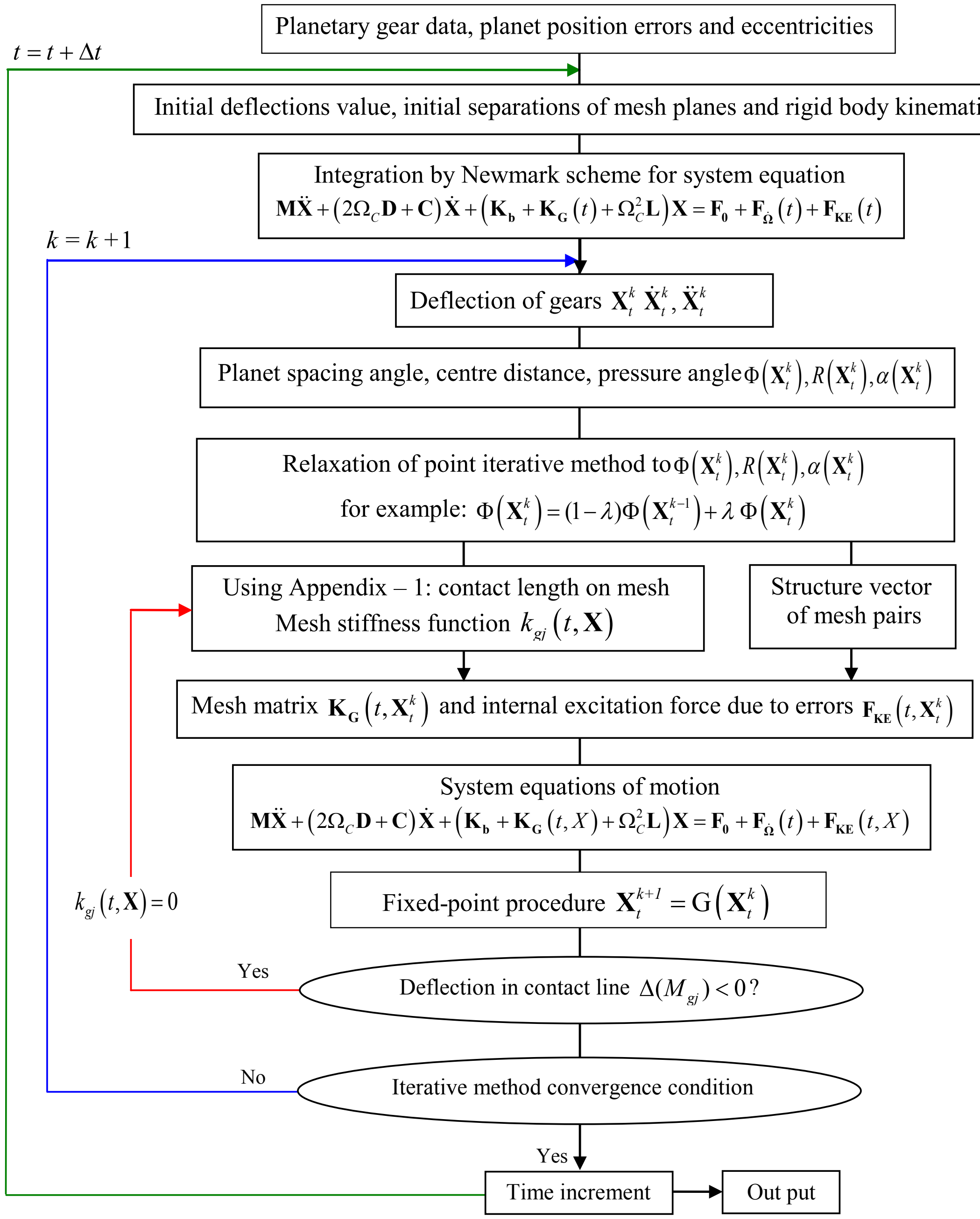

7 – Conclusion

A classic lumped parameter model of planetary gear with two translational and one torsional DOF has been extended to account for planet position errors and determine quasi-static and dynamic load sharing amongst the various meshes. Rigid-body rotations define the reference from which the degrees-of-freedom are defined and a specific procedure has been presented which makes it possible to solve for the motion transfer in the presence of errors and gives the initial separations between the teeth. A unique feature of the proposed approach is that mesh properties, errors and deflections are coupled. At each time step, the actual pressure angles, contact ratios, positions of base planes, meshing areas and consequently mesh phases are re-evaluated accordingly thus leading to a set of non-linear parametrically differential equations. However, the individual mesh stiffness model has been kept simple with the hypothesis of mesh stiffness functions directly proportional to the instantaneous contact lengths and, in this memoir, tooth profile and lead modifications have not been considered.

CHAPTER III

ELEMENTS OF VALIDATION

1 – Introduction

Prior to analyzing the dynamic performance of planetary gears in a systematic way, it is necessary to assess, as far as possible, the modeling quality and precision. This chapter is therefore aimed at presenting elements of validation based on comparisons with benchmark results from the literature.

In the first section, a number of quasi-static experimental and analytical results are confronted with the simulation results delivered by the model obtained for low-speeds. Several PTG architectures are considered which comprise from 4 to 6 planets, floating sun or floating planets, with planet errors. Experimental dynamic results in the literature are sparse and the comparisons are restricted to the measured and simulated acceleration spectra in the presence of planet eccentricity obtained by Inalpolat et al. [99].

Throughout this chapter, comparisons and tests will be performed by using the following gear data (Table 1).

Table 1 – Planetary gear sets (after [100] and [101])

	Sun-gear	Planet	Ring-gear
Tooth number			
case 1 (experiments)	73	26	125
case 2 (numerical analyses)	72	26	124
Normal module [mm]	1.81	1.81	1.81
Helix angle [°]	20	20	
Pressure angle [°]	23.04	23.04	
Addendum diameter [mm]	139.7	51.6	-
Dedendum diameter [mm]	-	-	229.4
Centre distance [mm]		92.12	
Active face width [mm]	25	25	

2 – Quasi-static load sharing amongst the planets

A number of quasi-static experimental (and also analytical) results have been presented by Singh [50], Kaharaman et al. [100] for a variety of planet numbers and planet position errors. The corresponding gear data is presented in Table 1 (case 1). One of the major findings by these authors was that radial position errors do not affect load sharing in contrast with tangential errors which were found to be highly influential on planet loading. The experimental conditions in [100] have been simulated by using the dynamic model presented in Chapter 2 for low-speeds so that dynamic effects can be ignored. The corresponding numerical load distributions have been confronted with the measurements in [100] when the sun-gear and carrier are chosen as the input and output, respectively. In what follows, planet load sharing is characterised by calculating the fraction of the total load supported by one planet j as:

$$L_j = \frac{mean\left(\left(\mathrm{F}_{\mathrm{Mesh}}(\mathrm{t},\mathbf{X})\right)_{\mathrm{j}}\right)}{T_{input} / Rb_S} \tag{1}$$

with:

$\left(\mathrm{F}_{\mathrm{Mesh}}(\mathrm{t},\mathbf{X})\right)_{\mathrm{j}} = k_j(\mathrm{t},\mathbf{X})\Delta_j$: total force at mesh j, where k_j is the total mesh stiffness and Δ_j, the total mesh deflection

Rb_S : base radius of sun-gear

T_{input} : input torque of sun-gear

Using the gear data for the 4-planet gear in Table 1 (case 1), the results in Figure 1 show the planet load sharing evolutions versus the sun-gear input torque for a floating sun-gear arrangement with a tangential error of 70 µm on planet #1, *i*) as measured by Ligata et al. [100] and *ii)* as calculated by using the proposed dynamic model at very low speed. It can be observed that, with a floating sun-gear, only two planets (planets #1 and 3) are loaded at low torque and that, as the sun-gear torque increases, all the planets come progressively into mesh. In agreement with the experimental evidence of [100], it is confirmed that diametrically opposed planets share the same load regardless of the error amplitude and input torque. It is also observed that load sharing is improved for the larger torque. For this example, an excellent agreement is obtained with the measurements and also the analytical model of [100] which validates the contact model in the presence of planet position errors.

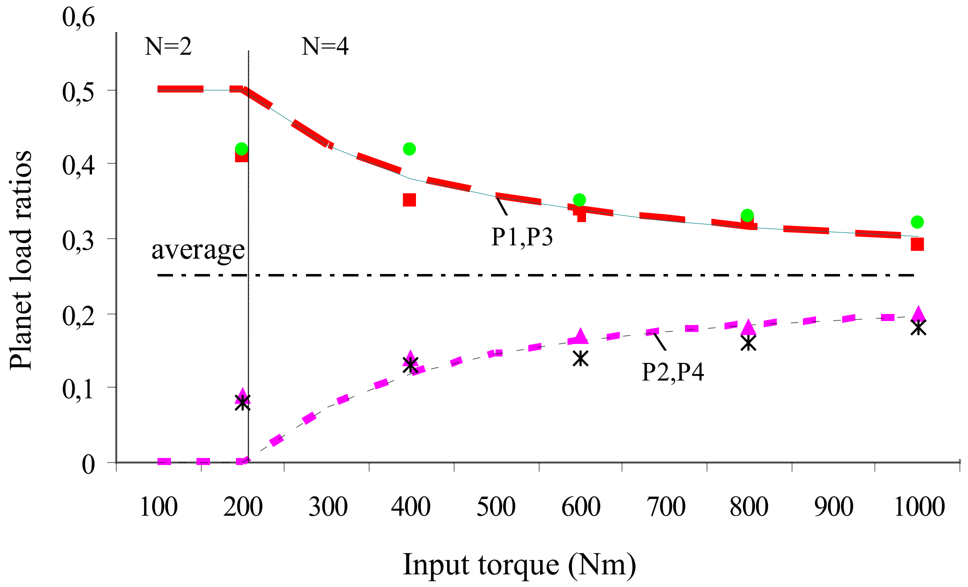

Figure 1 – 4-planet load ratios versus the input torque on the sun-gear

(Tangential position error ey1=70 µm on planet #1, sun gear rotational speed: 500rpm, N: planet number, Pj refers to planet #j, rotating carrier, planetary gear data: Table 1)

Theoretical results: ▬ ▬ ▪ ▪ ▪ —— ·- - *Experimental results:* ■ ▲ ● ⁎

Comparisons have been extended to PTGs with different planet numbers (5 and 6 respectively) while keeping the same tangential error of 70 µm on planet #1. The corresponding load sharing diagrams are shown in Figures 2 & 3. Here again, an excellent agreement is observed between the measurements and the numerical predictions. In these two cases, the planet with the position error is severely overloaded as it carries between 45 and 33% of the total load whereas two planets are free of load at the lowest torques. Increasing the input torque leads to a better sharing between the planets although substantial differences still exist.

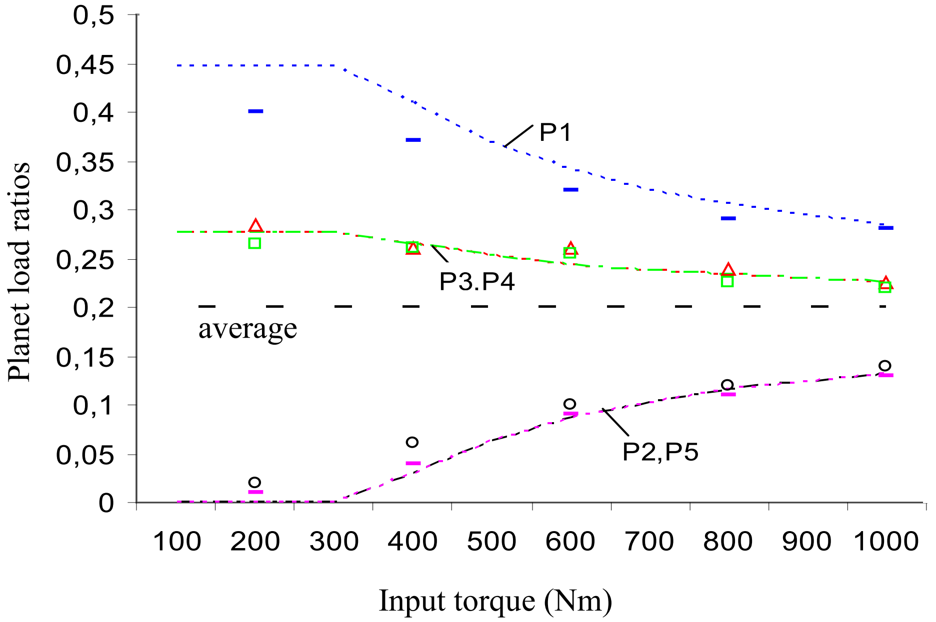

Figure 2 – 5-planet load ratios versus the input torque on the sun-gear

(Tangential position error ey1=70 µm on planet #1, sun gear rotational speed: 500rpm, N: planet number, Pj refers to planet #j, rotating carrier, planetary gear data: Table 1)

Theoretical results:

Experimental results: ▬ ○ △ □ ▬

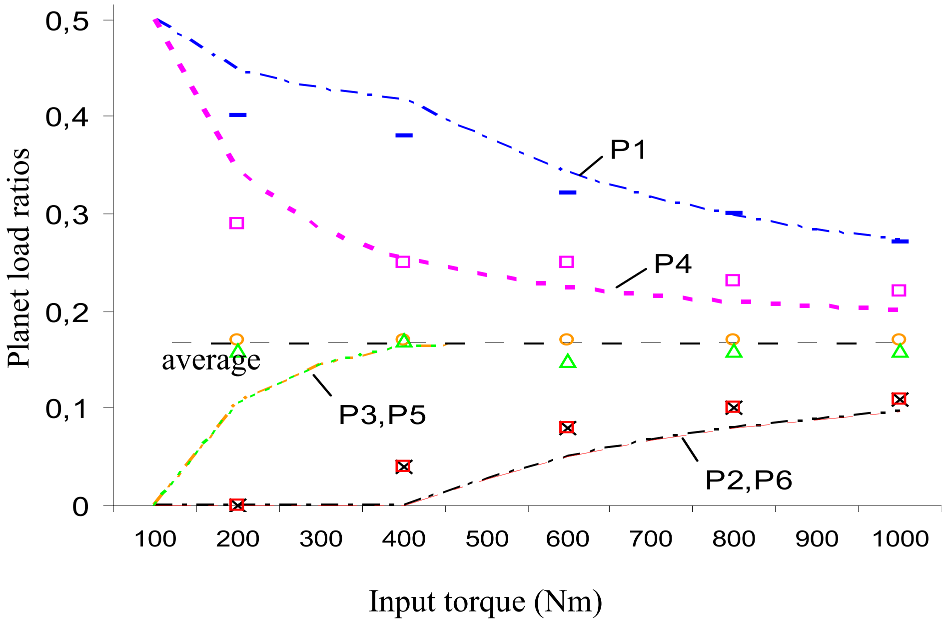

Figure 3 – 6-planet load ratios versus the input torque on the sun-gear

(Tangential position error ey1=70 µm on planet #1, sun gear rotational speed: 500rpm, N: planet number, Pj refers to planet #j, rotating carrier, planetary gear data: Table 1)

Theoretical results:

Experimental results: ▬ × ○ □ △ □

In this second series of comparisons, the experimental measurements have been conducted by keeping the input torque constant and varying the tangential position error amplitude on planet # 1. Three PTGs with respectively 4, 5 and 6 planets have been tested by the authors. The corresponding results are given in Figures 4, 5 and 6 along with the numerical predictions delivered by the dynamic model for low-speeds. For the whole range of experimental conditions, it can be noticed that the numerical tooth load ratios are in very good agreement with the experimental evidence thus confirming that the contact model is sound. Finally, it is worth mentioning that, even if it is assumed that all planets are in contact with the sun-gear in the state of reference, the model actually captures the contact losses caused by errors (for example, in Figure 1, only 2 planets withstand the load at the lower torque amplitudes).

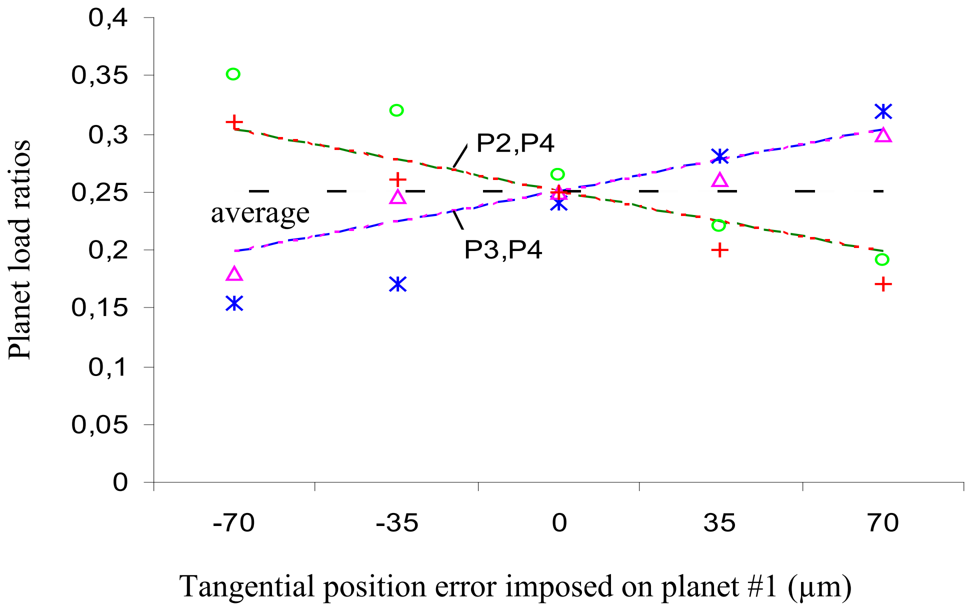

Figure 4 – 4-planet load ratios versus tangential position error on planet #1

(input torque on the sun-gear: 1000 Nm; sun-gear rotational speed: 200rpm, rotating carrier)

Theoretical results: - - - - - - - - ······· ······· *Experimental results:* ✳ ○ △ +

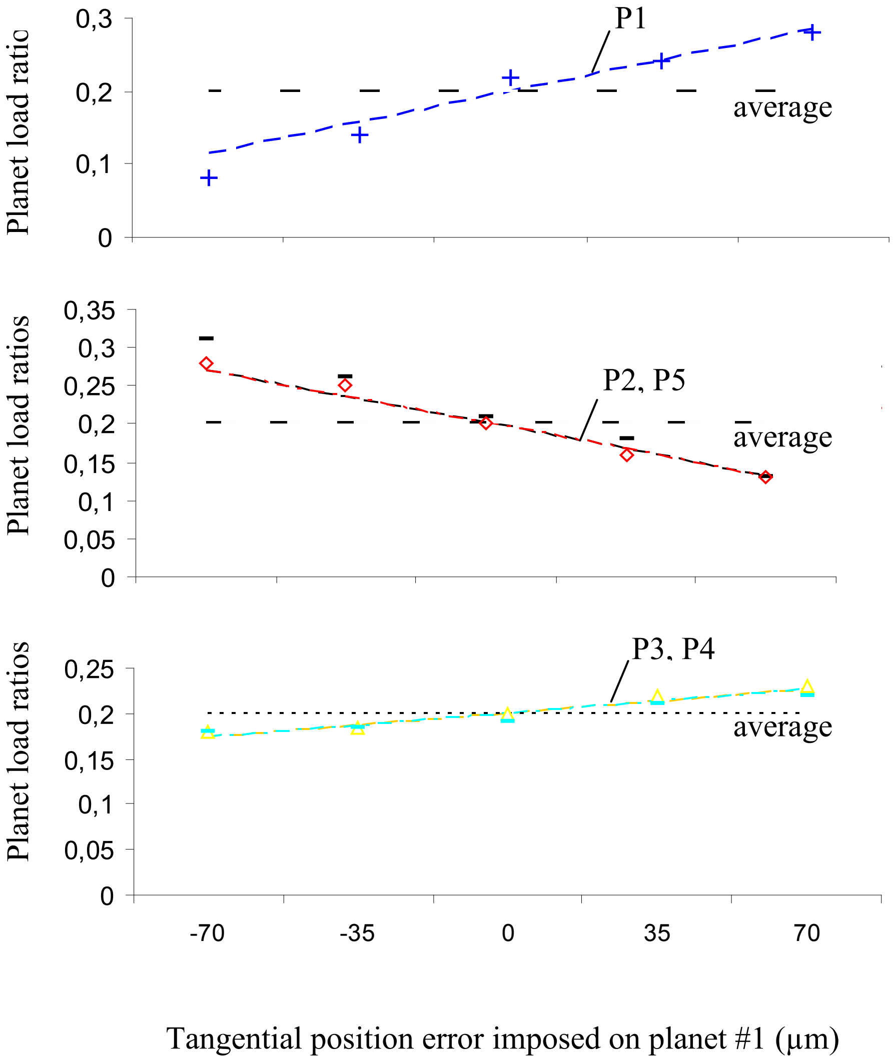

Figure 5 – 5-planet load ratios versus tangential position error on planet #1

(input torque on the sun-gear: 1000 Nm; sun-gear rotational speed: 200rpm, rotating carrier)

Theoretical results: – – – – · - - - - - - - - — · — — · —

Experimental results: + – △ – ◇

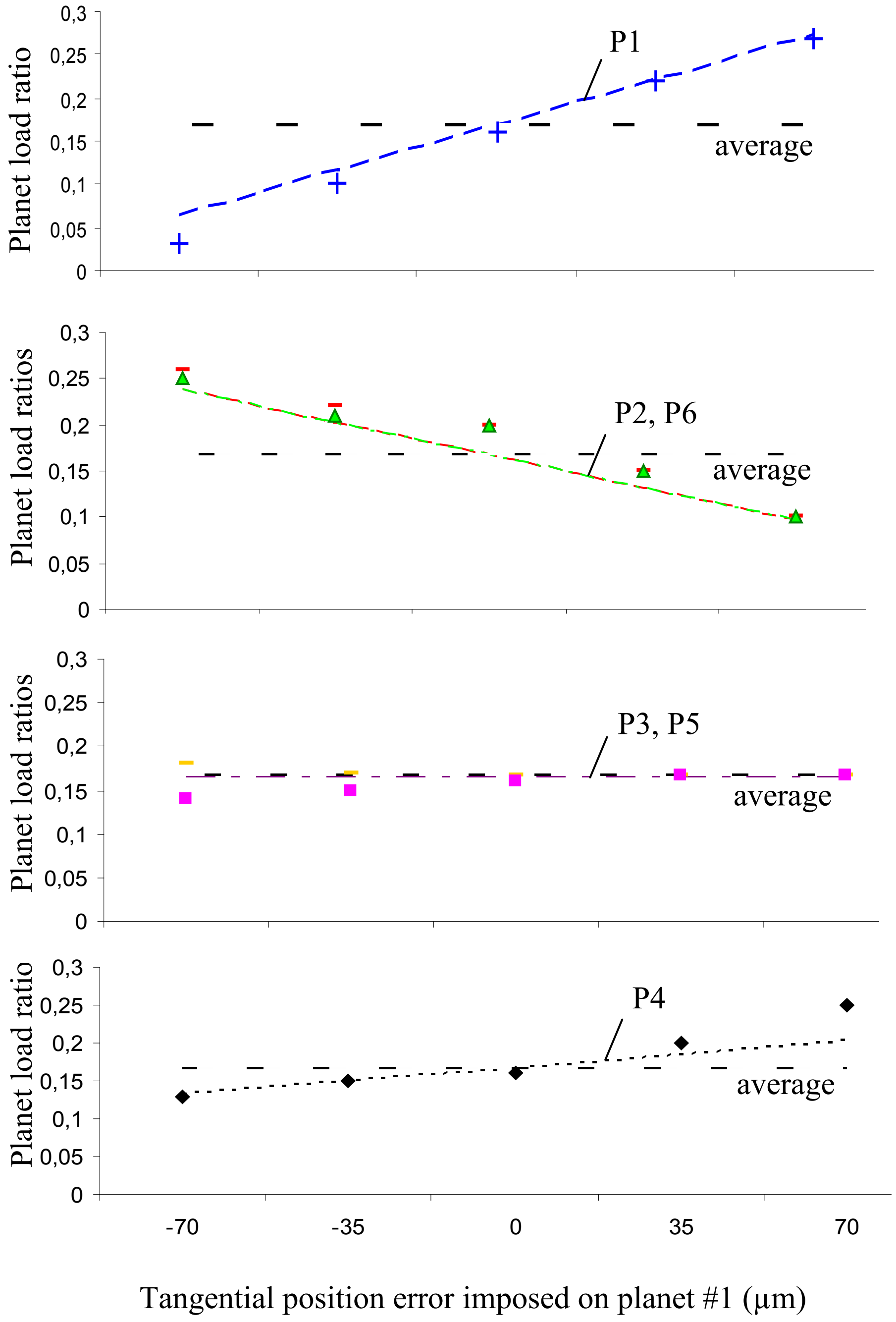

Figure 6 – 6-planet load ratios versus tangential position error on planet #1

(input torque on sun-gear: 1000 Nm; sun-gear rotational speed: 200rpm, rotating carrier)

Theoretical results: - - - - - - — - · ▬ ▬ — · — ——

Experimental results: + – – ◆ ■ ▲

3 – Influence of floating planets on quasi-static load sharing

The use of floating sun-gears to improve the load sharing amongst the planets is quite common and has already been thoroughly investigated but mostly for quasi-static conditions. However, it has been demonstrated that the elasticity of the planet shafts can also be highly influential [33], [44], [54], leading to improved load sharing compared with that obtained with floating sun-gears. The versatility of the proposed model is first illustrated for quasi-static conditions by comparing the results obtained at low speed and those given by Singh's formulae [50], [102], where the load ratio is determined in terms of the so-called neutralizing ratio X_e defined as:

$$\mathrm{X}_e = -\frac{K_{eff}\, e_{yj}}{2T_S / Rb_S} \tag{2}$$

with:

$K_{eff} = \dfrac{1}{\dfrac{1}{k_b} + \dfrac{1}{(k_s + k_r)}}$: effective stiffness of the sun-planet-ring-bearing system in the tangential direction. k_b is the bearing radial stiffness of planets, k_s, the sun-gear/planet average mesh stiffness and k_r, the planet/ring-gear average mesh stiffness

e_{yj} : planet position error in the tangential direction

For positive errors:

Load ratio on planet #1: $L_1 = [1 - (n - 1)]Xe / n$; on other planets: $L_{2,3,\dots,n} = [1 + Xe] / n$.

For negative errors:

Load ratio on planet #1: $L_1 = [1 + (n - 1)]Xe / n$; on other planets: $L_{2,3,\dots,n} = [1 - Xe] / n$.

Two sets of results for the 4-planet gear set defined in Table 1 (case 2) with isotropic flexible planet supports (1E6 N/m in two perpendicular directions) are presented. In Figures 7, 8 and 9, a constant tangential error of 0.2mm on planet #1 is considered and the sun-gear torque is varied between 100 and 1000 Nm whereas, in Figures 10, 11 and 12, the torque is kept constant (1000 Nm) and the tangential error varies between -0.5 and +0.5 mm. For every configuration, the load factor calculated by the dynamic model and the results from [50], have been superimposed. The main conclusions are: i) the static planet loads calculated by Singh's formulae and by the dynamic model at low speeds are similar and ii) it is confirmed that floating planets are interesting solutions for planet load sharing superior to the configuration with a floating sun-gear (compare with the results in Figure 1 which are worse even if the position error is smaller).

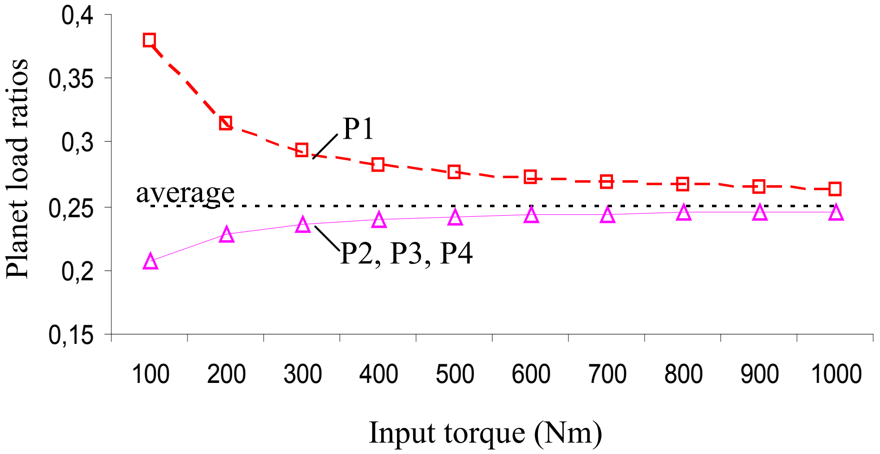

Figure 7 – 4-planet load ratios versus the input torque on the sun-gear

(Tangential position error ey1=0.0002m on planet #1, sun-gear rotational speed: 200rpm, rotating ring-gear, planetary gear data: Table 1 – case 2)

Proposed model: – – ——— *Formulae in [50]:* □ △

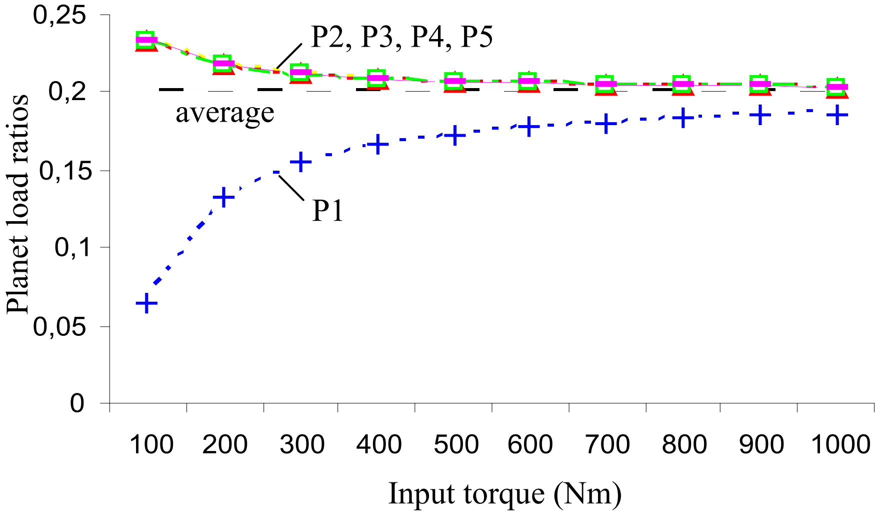

Figure 8 – 5-planet load ratios versus the input torque on the sun-gear

(Tangential position error ey1=0.0002m on planet #1, sun-gear rotational speed: 200rpm, rotating ring-gear, planetary gear data: Table 1 – case 2)

Proposed model: ········ - - - - | —— -·-·- -·-·- *Formulae in [50]:* + ○ △ □ –

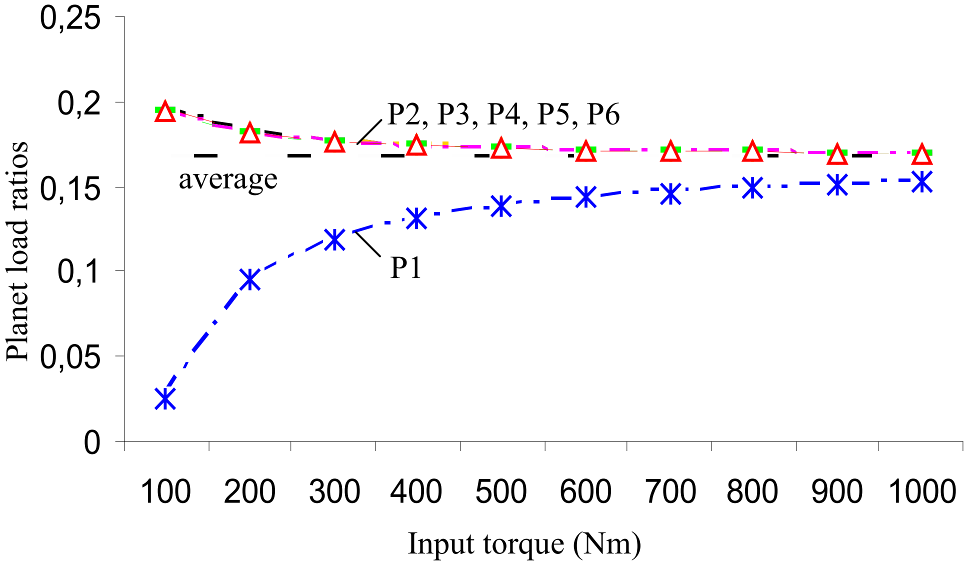

Figure 9 – 6-planet load ratios versus the input torque on the sun-gear

(Tangential position error ey1=0.0002m on planet #1, sun-gear rotational speed: 200rpm, rotating ring-gear, planetary gear data: Table 1 – case 2)

Proposed model: — — — — — —

Formulae in [50]: * ○ + △ – –

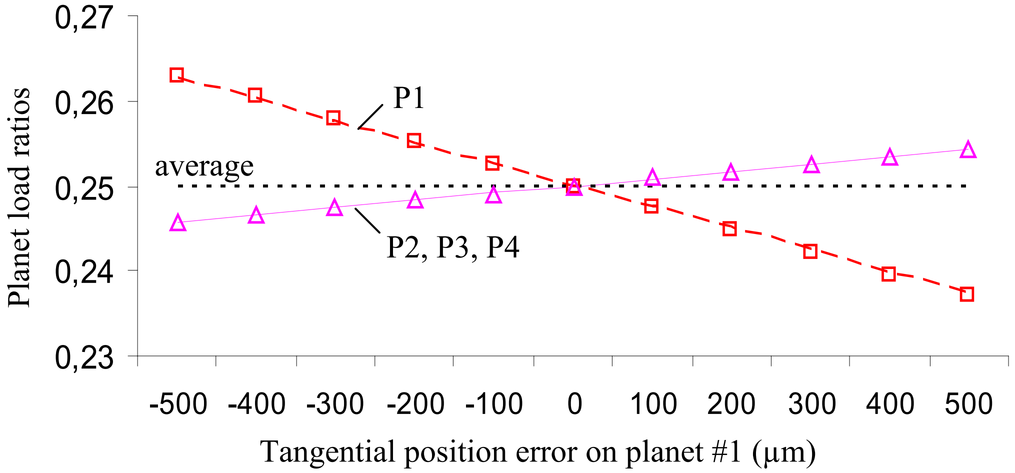

Figure 10 – 4-planet load ratios versus tangential position error on planet #1

(input torque on sun-gear: 1000 Nm; sun-gear rotational speed: 200rpm, rotating ring-gear)

Proposed model: – – — *Formulae in [50]:* □ △

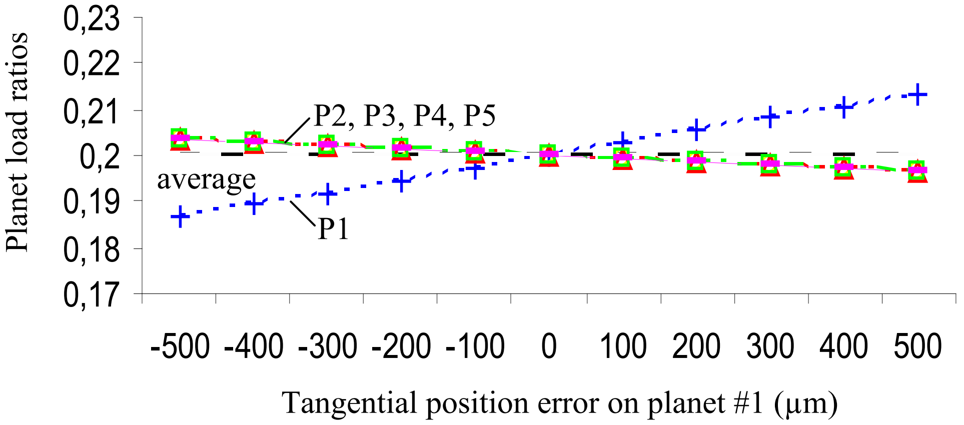

Figure 11 – 5-planet load ratios versus tangential position error on planet #1

(input torque on sun-gear: 1000 Nm; sun-gear rotational speed: 200rpm, rotating ring-gear)

Proposed model: ⋯ — ⋯ -·- -··-

Formulae in [50]: + ○ △ □ –

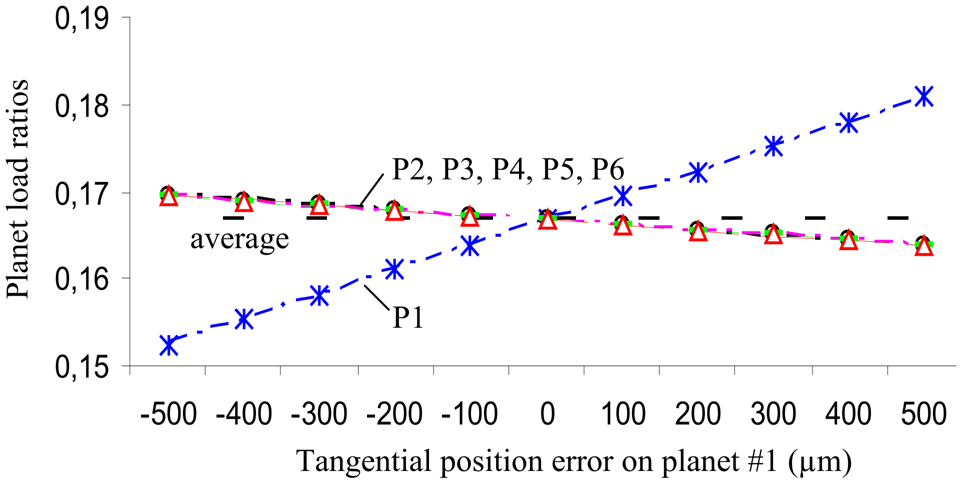

Figure 12 – 6-planet load ratios versus tangential position error on planet #1

(input torque on sun-gear: 1000 Nm; sun-gear rotational speed: 200rpm, rotating ring-gear)

Proposed model: ⋯ — — ⋯ -·- -··-

Formulae in [50]: ✱ ○ + △ – –

4 – Acceleration spectrum analysis in the presence of eccentricity on one planet

4.1 – Introduction

In this section, the PTG arrangement is such that the sun-gear is the input and the planet carrier the output member whereas the ring-gear is the stationary (reaction) member. An accelerometer was fixed to the stationary member by M. Inalpolat et al [101] in an effort to characterize the modulation sidebands induced by eccentricities as illustrated in Figure 13. The measurements are clearly impacted by the carrier revolution and the passage of the planets which modulates the acceleration measurements on this fixed part.

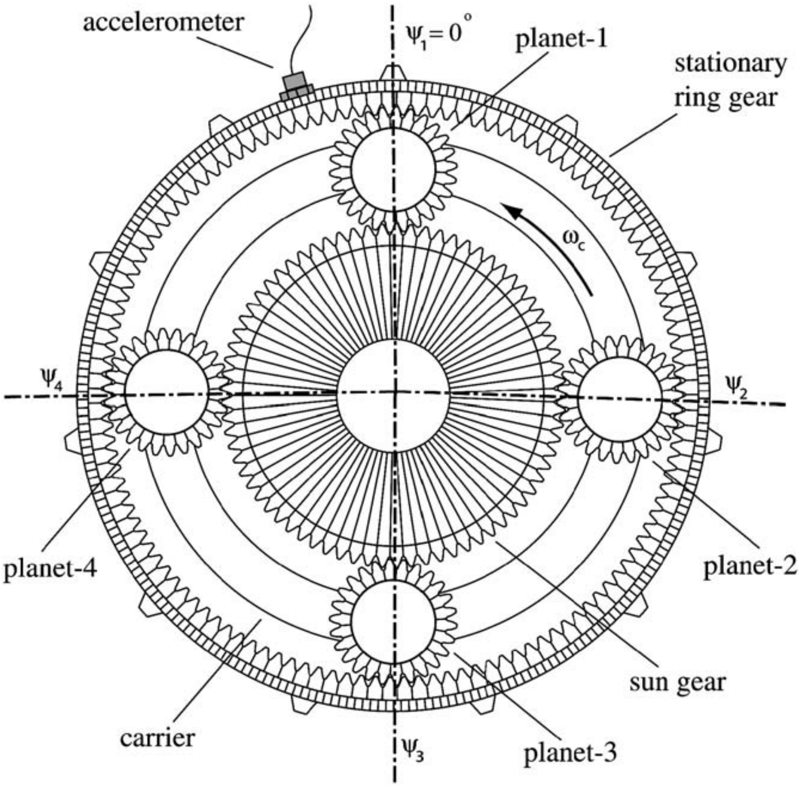

Figure 13 – A schematic showing the components of a 4-planet PTG with an accelerometer mounted on the ring-gear [101]

The comparisons between the measurements on the ring-gear outer surface and the predictions by our model are not direct because of the aforementioned modulations due to the fact that the individual mesh force lines of actions are fixed in the rotating frame attached to the carrier. For one revolution of the carrier, the accelerometer will therefore experience disturbances from all the planets in sequence. Following [101], it is assumed that:

a) the individual contribution of one given planet will last over the time interval Tc/N where Tc is the rotational period of the carrier, N is the number of planets

b) after a progressive increase, the influence of this given planet is maximum when the planet is at the same angular position as that of the accelerometer and then progressively vanishes as the planet moves away from the location of the transducer.

From a mathematical viewpoint, a Hanning windowing function (smoothening the entry and exit of the disturbance) combined with Heaviside unit functions can conveniently simulate the progressive evolutions and the passage of the planet in front of the accelerometer as described above. The acceleration on the ring gear outer surface will then be expressed as:

$$a(t)=\sum_{j=1}^{N} C w_j(t) F_j(t) \tag{3}$$

where

a) $w_j(t)=W_j w\left(t-\dfrac{\Phi_j}{\omega_C}\right)U_j(t)$

$w(t)=\dfrac{1}{2}-\dfrac{1}{2}\left[\cos\left(N\cdot\omega_C\cdot t\right)\right]$, Hanning windowing function; ω_C : angular velocity of the carrier with respective to the inertial frame; N : number of planets; Φ_j : angular position location of planet #j around the carrier.

$U_j(t)$: windowing function simulating the passage of planet j in front of the transducer such that $U_j(t)=\sum_{n=1}^{\infty}\left\{H\left[t-\left(\dfrac{(n-1)N+j-1}{N}\right)T_C\right]-H\left[t-\left(\dfrac{(n-1)N+j}{N}\right)T_C\right]\right\}$

where T_C is the revolution period of the carrier, $H(x)$ is the Heaviside unit step function ($H(x)=1 \quad if\ x>0$ or $H(x)=0$ otherwise).

b) $F_j(t)$ is the total mesh force at the j^{th} planet /ring-gear interface as calculated by the dynamic model.

c) C is a constant relating the acceleration to the dynamic mesh force (intrinsic property of the ring–gear).

4.2 – Example 1: Acceleration spectra for an errorless PTG

The case of reference corresponds to the planetary gear data in Table 1 (case 1) in the absence of errors. The objective is to verify that the mesh phasing is correctly reproduced in the numerical simulations for this particular type of PTG where planet phasing is arbitrary (neither in-phase nor sequentially phased, that is $\frac{Z_R \Phi_{\mathrm{j}}}{2\pi} \neq n$ and $\sum_{j=1}^{N} Z_R \Phi_{\mathrm{j}} \neq m\pi$, n and m are integer). Figure 14 represents the dimensionless acceleration spectra centered on the 125th carrier order frequency (which corresponds to the mesh frequency) as measured and simulated by Inalpolat et al. [101] along with the results provided by the model presented in chapter 2. The peak positions and their relative amplitudes are in very good agreement and all the spectra exhibit comparable asymmetric modulation sidebands. The sidebands at even integer orders $H_m \pm n$ ($H_m = Z_R = 125$, n: integer) such as 120, 122, 124, 126, 128 and 130, etc., can be attributed to the amplitude modulations due to the carrier rotation, which are always asymmetrically distributed about the mesh orders H_m. The most dominant harmonic order with the maximum amplitude is H=126. However, the experimental spectrum comprises also harmonics at odd integer orders which are attributed to the influence of the ring-gear deflections (not taken into account in our model) and inevitable errors in a real mechanism.

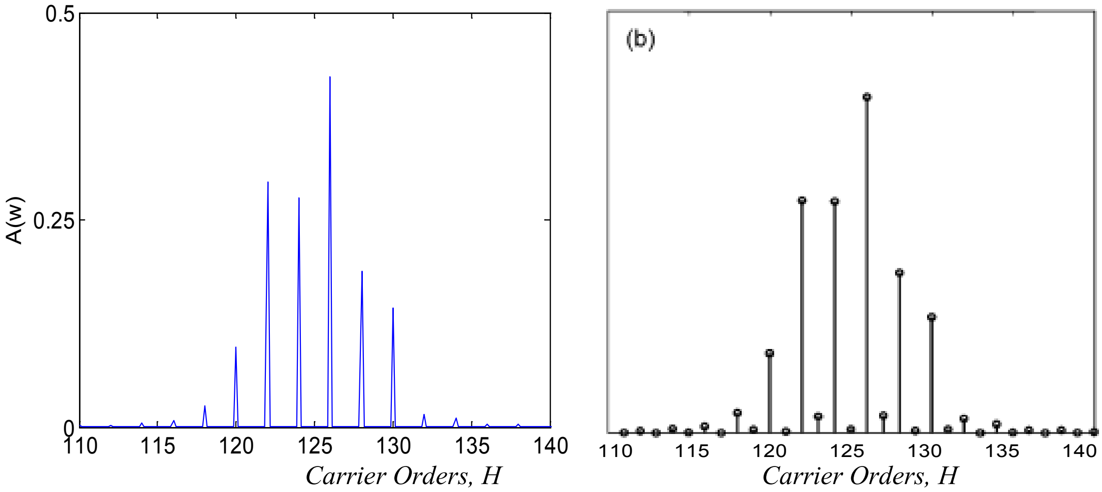

(a) Numerical analysis (b) Numerical analysis by Inalpolat [101]

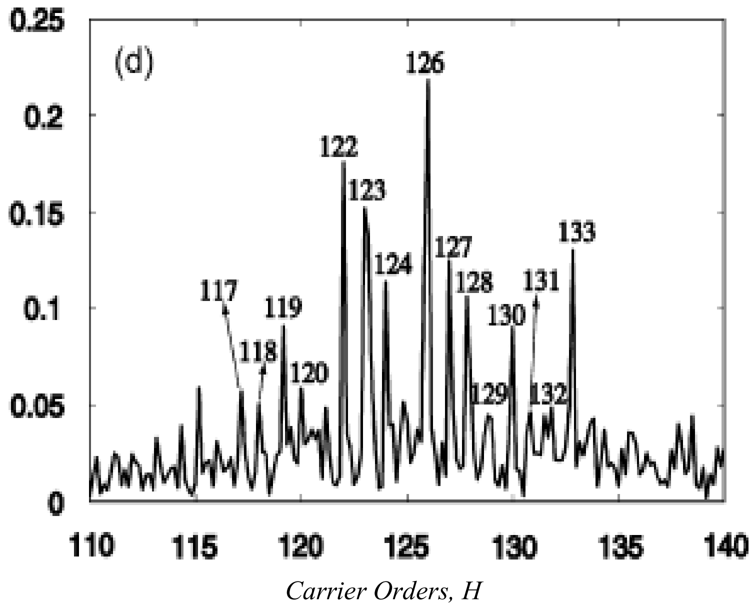

(c) Measured results by Inalpolat [101]

(Input torque on sun-gear: 1000Nm, sun-gear rotational speed: 200rpm)

Figure 14 – Acceleration spectra on the ring-gear

4.3 – Example 2: Acceleration spectra in the presence of eccentricity on one planet

Figure 15 (a) shows an example of acceleration spectra measured on the same PTG as in 4.2 but with an eccentricity of amplitude 200 μm on one planet for a sun-gear torque of 400 Nm and a sun-gear rotational speed of 500 rpm. The dynamic model accounts for time-varying mesh stiffness functions, the influence of errors and DOFs on the instantaneous positions of the base planes and the associated amplitude and frequency modulations. The simulated acceleration spectrum in Figure 15 (b) compare reasonably well with the experimental one although the latter exhibits a more complex sideband structure within a wider frequency range around the fundamental gear mesh frequency. The sidebands at even integer orders $H_m \pm n$ ($H_m = Z_R = 125$, n: integer) such as 120, 122, 124, 126, 128 and 130 can be attributed to the modulations due to the carrier rotation while those at $H = H_m \pm n \pm H_{p/C}$, $H_{p/C} = Z_R / Z_p = 125/26 = 4.8077$, at orders such as 118.19, 119.19, 122.19, 126.81, 127.81, 128.81, 130.81, 131.81 can be considered as a direct modulation associated with the planet eccentricity. It is to be noted that the amplitudes have been normalised with respect to the maximum peak amplitude since the actual transfer function in the test rig is unknown and depends, among other things, of the damping. However, it is believed that the modelling of eccentricities is basically sound and that extensions towards dynamic regimes are possible.

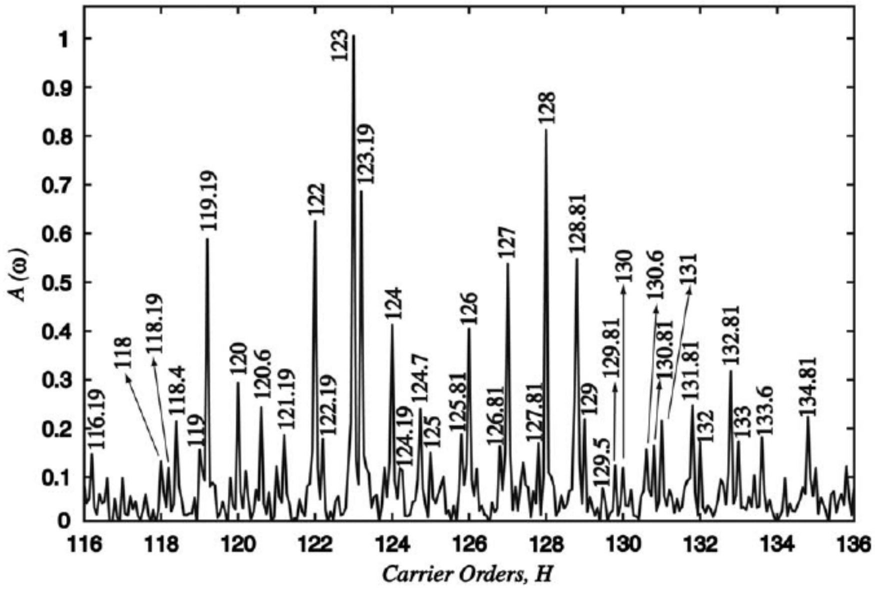

(a) Measured results by Inalpolat et al. [99]

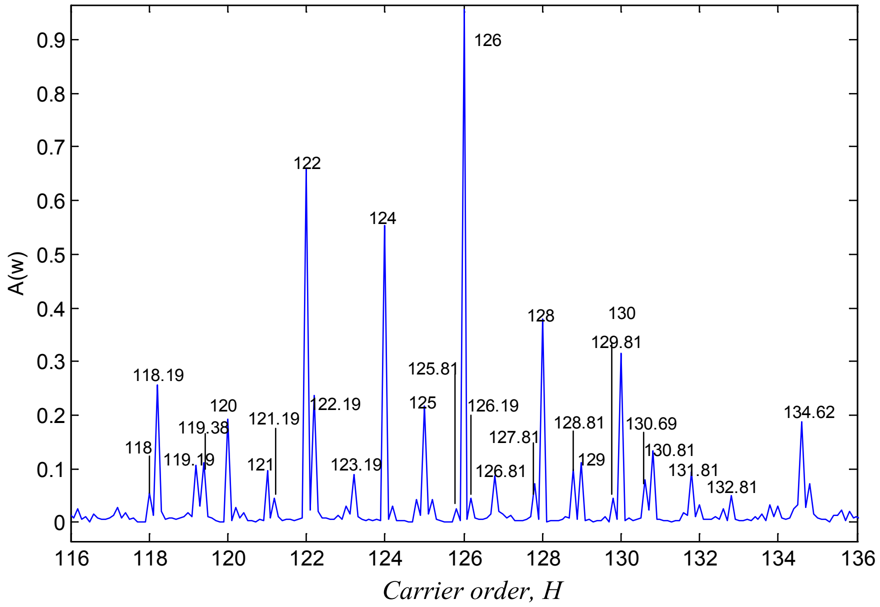

(b) Numerical analysis results

Figure 15 – Acceleration spectrum of a 4-planet planetary gear set with an eccentricity on planet #1

5 – Conclusion

Based on a series of comparisons with experimental results from the literature, it can be concluded that the contact simulations in the PTG dynamic model are sound. Several position errors over a broad range of torque have been tested leading to severe overloads on certain elements which are correctly reproduced by the proposed approach. As far as eccentricities are concerned, it has been possible to compare with some measurements performed on a stationary ring-gear for a rotating carrier. The corresponding spectrum in the vicinity of the fundamental of the mesh frequency agrees well with the experimental findings and it found, in particular, that the maximum peak does not correspond to the mesh frequency (125th carrier order) but is at the 126th carrier order. The experimental spectrum exhibits broader side-bands than the simulation results which can be explained by i) the influence of the ring-gear deformability not taken into account here, and ii) other inevitable faults which were not included in the model.

CHAPTER IV

INFLUENCE OF PLANET POSITION ERRORS AND ECCENTRICITIES

1 – Introduction
2 – Dynamic behaviour without error
3 – Dynamic behaviour with planet position error
4 – Influence of sun-gear eccentricity
5 – Conclusion

1 – Introduction

One of the main advantages of planetary gears is the possibility to split the power path into several branches which are consequently less loaded than the equivalent fixed-axis gear set would be. These redundant paths of motion are also a drawback in the sense that the system may become very sensitive to errors of all sorts which can lead to severe overloads on certain members and ultimately failures. In this chapter, the static and dynamic performance of PTGs is investigated for two common and influential errors, i.e., planet position errors and eccentricities for several input/output combinations (fixed carrier or ring-gear, floating or rigid mounts). Particular emphasis is placed on the contributions of floating members as it is well-known that they can compensate for some geometrical errors such as run-out, non uniform diameters, tooth spacing, etc. and improve the load sharing amongst the planets. In this chapter, three configurations are considered: i) rigid mounts such that the radial bearing stiffness of sun-gear, planets and ring-gear/carrier (output) is $10^8\,\mathrm{N/m}$, ii) floating sun-gear with a radial bearing stiffness of $10^4\,\mathrm{N/m}$ and finally, iii) floating planets whose radial bearing stiffness is $10^6\,\mathrm{N/m}$. The results presented in this chapter mostly concern a) the dynamic load sharing amongst the planets and, b) the trajectories of several members for a range of rotational speeds.

Table 1 – Planetary gear sets (after [100] and [101])

	Sun-gear		Planet		Ring-gear
Tooth number					
case 1 (experiments: arbitrary phase)	73		26		125
case 2 (numerical analyses: in phase)	72		26		124
Normal module [mm]	1.81		1.81		1.81
Helix angle [°]		20		20	
Pressure angle [°]		23.04		23.04	
Addendum diameter [mm]	139.7		51.6		-
Dedendum diameter [mm]	-		-		229.4
Centre distance [mm]			92.12		
Active face width [mm]		25		25	

2 – Dynamic behaviour without error

In this section, the classic model relying on constant geometry and mesh characteristics is confronted with the proposed approach where updated error and DOF-dependent tooth contact conditions are considered. The comparisons have been carried out by considering the 4-planet planetary gear defined in Table 1 (case 2) without errors.

The maximum or minimum load ratio of all sun (ring)-gear/planet meshes for a given rotational speed of sun-gear is calculated by the following formula:

$$R_{\max/\min} = \frac{N \cdot \max/\min\left(F_{Mesh}(t, \mathbf{X})\right)}{T_{input} / Rb_S} \tag{1}$$

with:

N : number of planets

$F_{Mesh}(t, \mathbf{X})$: Steady-state mesh forces of all sun (ring)-gear/planet meshes

As long as fixed carriers are considered, it has been found that the two models generally give very similar dynamic tooth loads and no obvious differences have been reported. However, for a rotating carrier (epicyclic gear set), the results in Figure 1 show that different dynamic tooth load curves are obtained depending on the modelling hypotheses. This effect is particularly marked in the high-speed supercritical zone where the dynamic forces on the meshes are modified compared with the classic findings. These deviations can be related to the variations in mesh geometry caused by the centrifugal effects on the planets. In order to illustrate this phenomenon, the evolutions of the average contact ratios for the sun-gear/planet and planet/ring-gear meshes have been plotted in Figure 2. It can be observed that, starting from approximately the same value of 1.6 at low-speeds, the external and internal mesh geometries progressively diverge as the carrier speed increases. Interestingly, the areas where the models give different dynamic results are also characterised by a certain degree of sensitivity to the initial conditions used in the numerical process as illustrated by the set of response curves in Figure 1. It is to be noted that this slightly chaotic behaviour is not caused by contact losses and shocks since the minimum dynamic tooth loads remain positive over the speed range (Figure 1).

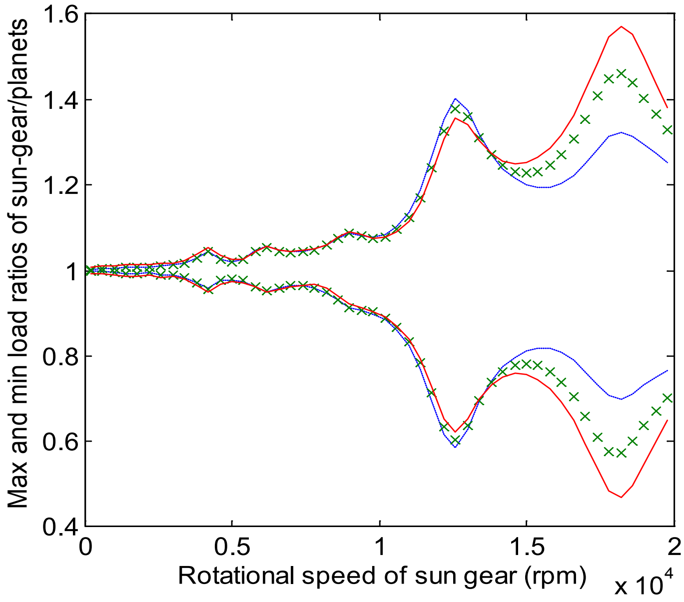

(a) Sun-gear/planet

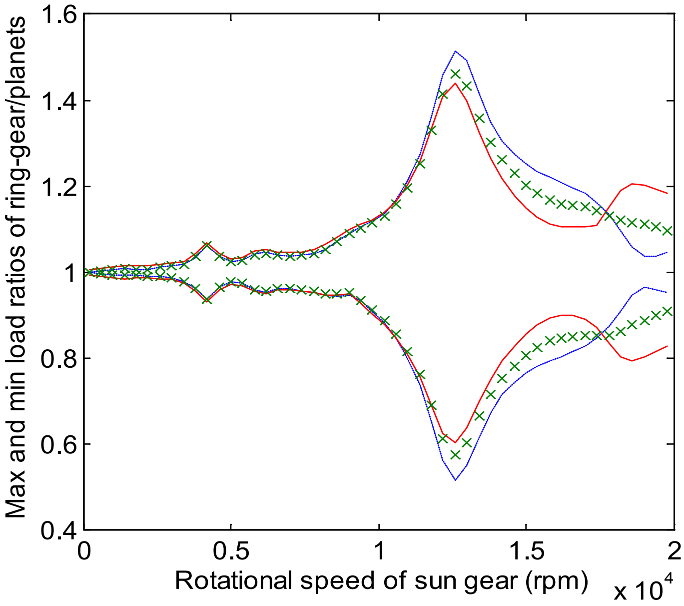

(b) Ring-gear/planet

Figure 1 – Maximum load ratios of sun-gear/planet meshes versus sun-gear rotational speed, carrier is allowed to rotate *(Planetary gear data: Table 1 – case 2)*

Keys:

Constant geometry: independent on initial condition —

Varying geometry: initial conditon1 fork line: static solution with averages stiffness —

initial condition2 dotted line: steady-state response at previous speed ×

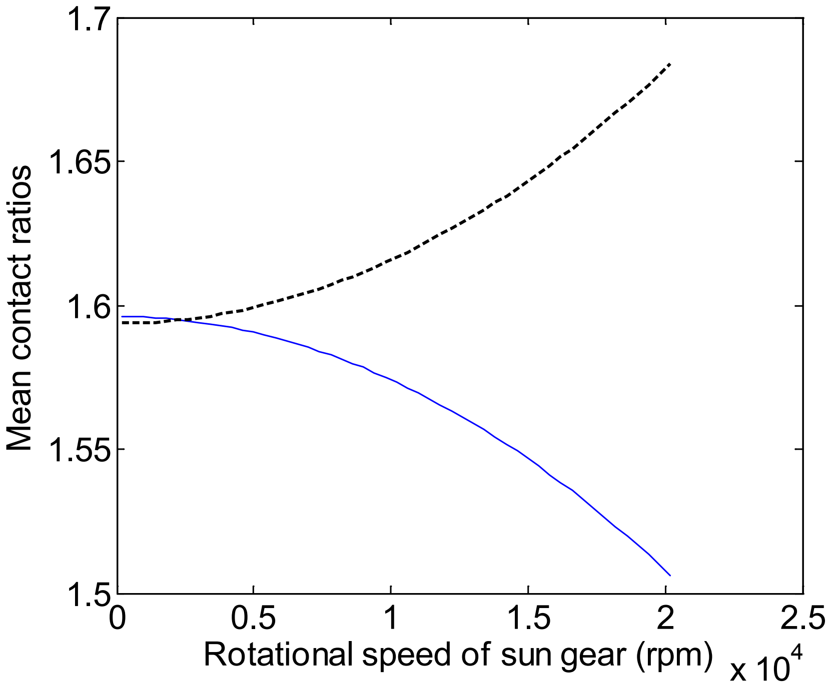

Figure 2 – Mean contact ratios of sun(ring)-gear/planet meshes versus sun-gear rotational speed

Keys:
Sun-gear/planet meshes ——— *Ring-gear/planet meshes* - - - -

3 – Dynamic behaviour with planet position error

3.1 – Planet position errors with a rotating carrier

The gear geometry is that defined in Table 1 with a fixed ring-gear, a floating sun-gear and position errors on planet #1 (conventional). Considering, first, a negative tangential error of -0.2mm, the deviations in terms of dynamic forces are limited as shown in Figure 3 (a) and most of the tooth load differences between the planets are already present at very low speeds. A slight variation in the response peak amplitudes can be observed between the classic (with constant geometry) and the error/DOF-dependent (with varying geometry) models. These trends are more marked when a larger error of -0.5 mm is introduced and the second tooth critical frequency is shifted towards the higher speeds (Figure 3 (b)). Compared with the errorless dynamic responses, the average level of the maximum tooth loads on diametrically opposed planets are identical; higher on planets #1 (with the errors) & #3 and lower on planets #2 & #4 as is the case in quasi-static conditions.

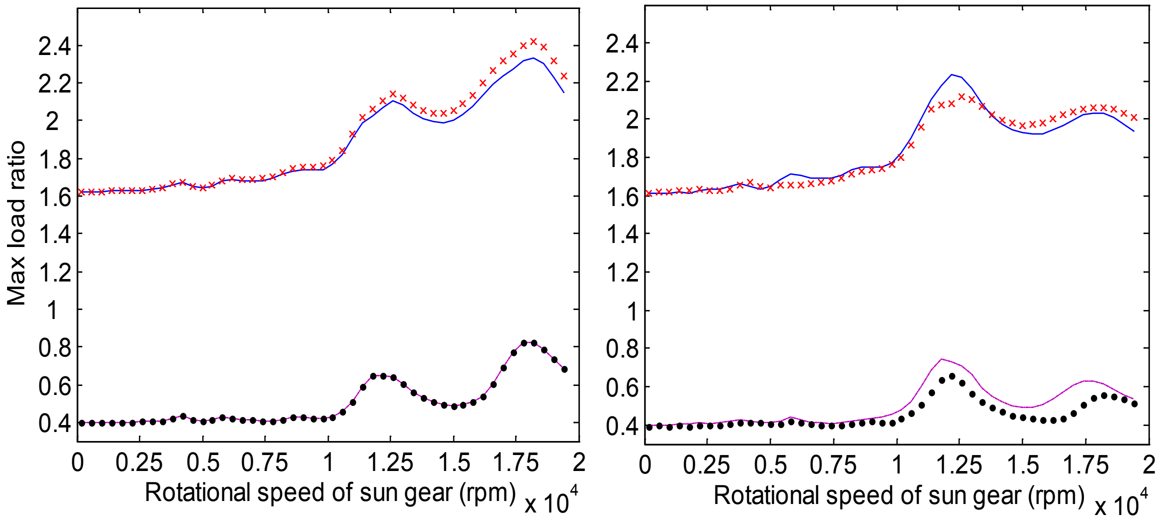

Constant parameters

Varying parameters

(a) Tangential position error ey1= -0.2 mm on planet #1

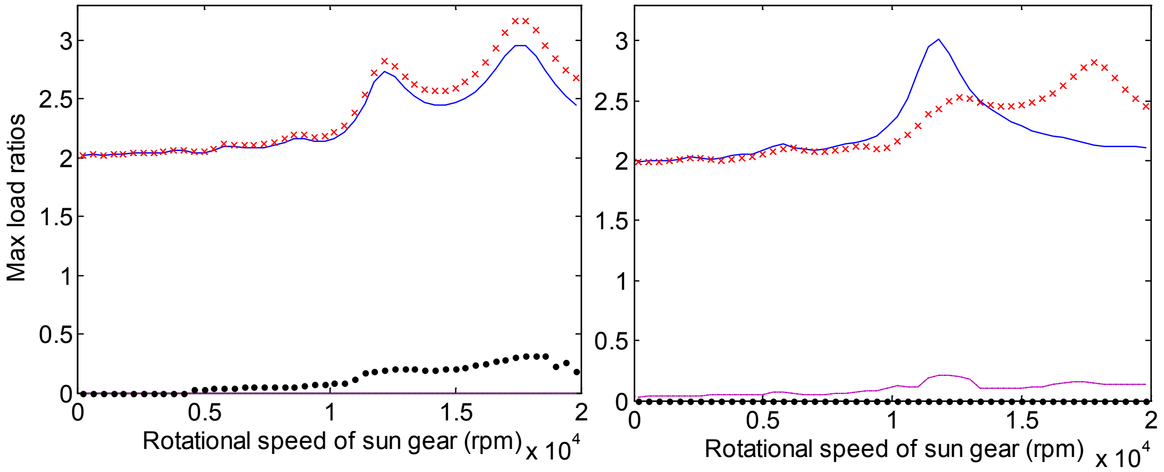

Constant geometry

Varying geometry

(b) Tangential position error ey1= -0.5 mm on planet #1

Figure 3 – Maximum dynamic load ratios of sun-gear/planet meshes versus sun-gear rotational speed *(rotating carrier, Planetary gear data: Table 1 – case 2)*

Keys:

sun-gear/planet #1 —— *sun-gear/planet #2* ····· *sun-gear/planet #3* × *sun-gear/planet #4* ●

The results presented above for one specific error can be generalised over a range of tangential errors on one planet as illustrated in Figure 4 where the maximum dynamic factor is represented in terms of both the sun-gear rotational speed and the error amplitude (positive and negative). The results at low speeds compare very well with those obtained analytically by Singh [50], [102] using the so-called neutralising ratio and the effective sun-planet-ring-bearing tangential stiffness. At higher speeds, tooth load peaks (no shocks) emerge whose positions and amplitudes differ depending on the modelling hypotheses (constant or error/DOF-dependent solution). It is observed that, even for helical gears, significant tooth load amplifications can be found in the presence of planet position errors. These dynamic effects exacerbate the consequences of the quasi-static uneven loading on the planets potentially leading to tooth failures.

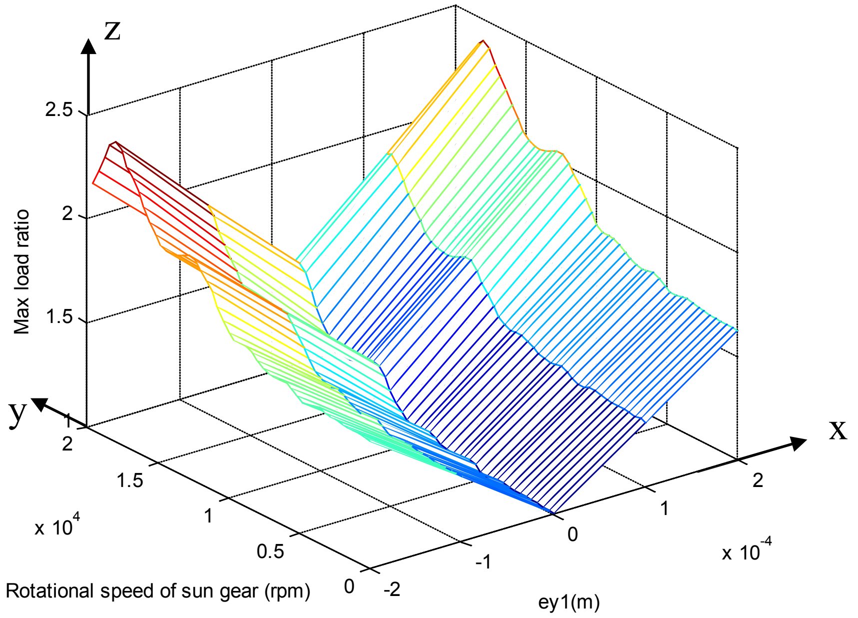

Constant geometry

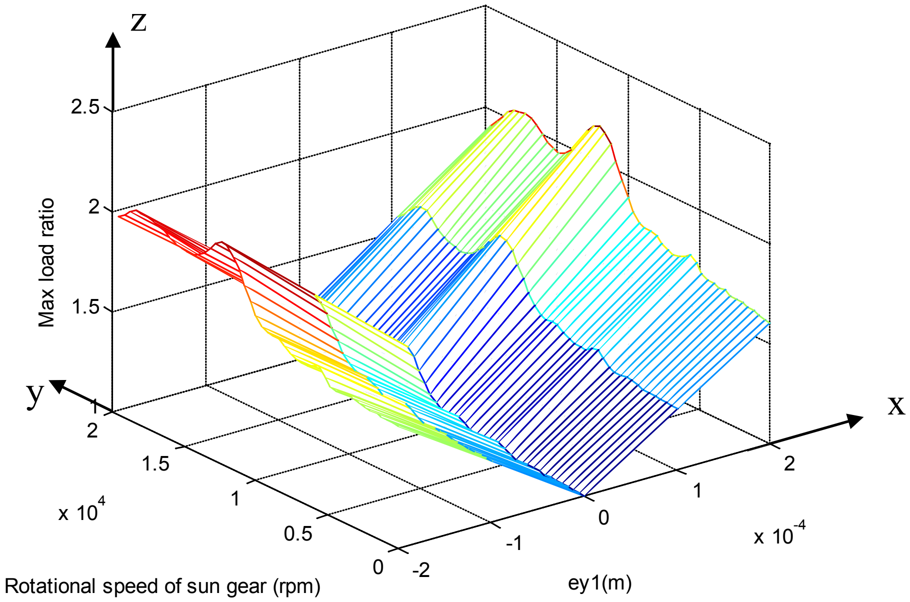

(a) Varying geometry

Figure 4 – Maximum dynamic load ratios of sun-gear/planet meshes versus sun-gear rotational speed and tangential error amplitude

(rotating carrier, planetary gear data: Table 1 – case 2)

3.2 – Planet position error and rotating ring-gear

In this section, the carrier is considered as stationary (reaction member) and the output is on the rotating ring-gear. A negative tangential error of -0.2 mm on planet #1 is simulated and the consequences in terms of mesh stiffness function for every sun-gear/planet contact at high-speed (11800 rpm on the sun-gear) are illustrated in Figure 5. Imposing a constant geometry, the mesh stiffness functions of sun-gear/planets represented by the solid lines are all identical since all the planets are in phase. With varying geometry, however, every mesh is found to possess a particular level of average stiffness along with different time evolutions or parametric excitations suggesting that, as opposed to the errorless case, each mesh may experience a different dynamic behaviour. Moreover, some degree of amplitude and phase modulations can be observed in the mesh stiffness functions.

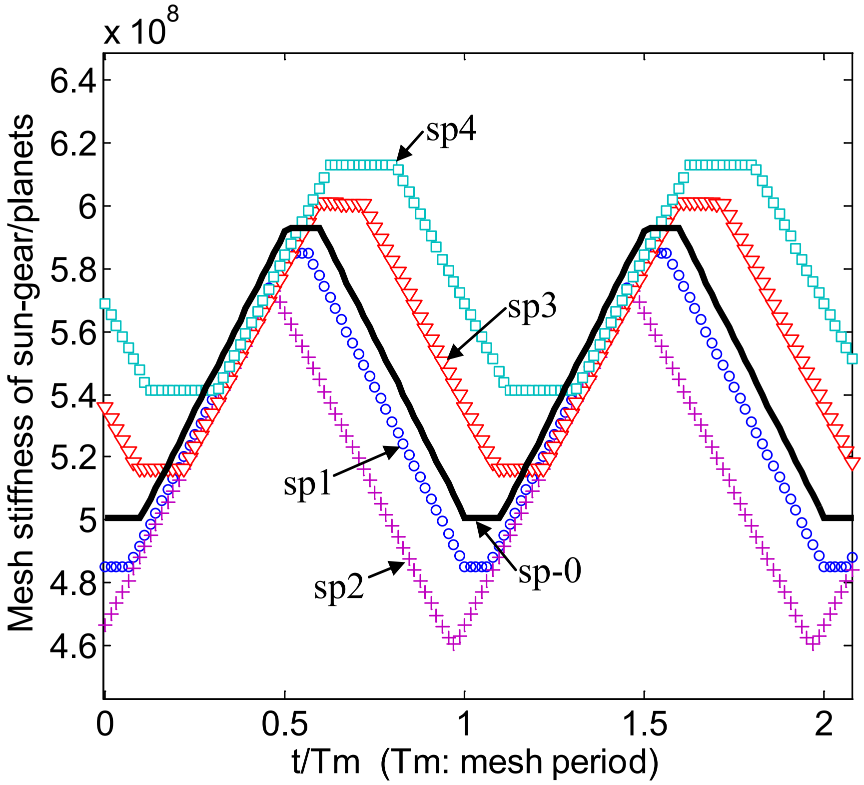

Figure 5 – Mesh stiffness function with a tangential position error ey1= -0. 2mm on planet #1 *(sun-gear speed* Ω_S=11800 rpm*, rotating ring-gear)*

Keys:

<u>constant geometry:</u> sun-gear/planets without errors —

<u>varying geometry:</u> sun-gear/planet #1, #2, #3, #4 ○ + ▽ □

For a floating sun-gear arrangement, a stationary carrier and a tangential position error $e_{y1} = -0.2\text{mm}$ on planet #1, Figure 6 shows the evolutions of the maximum planet load ratio of every planet versus the sun-gear speed considering constant and error & DOF-dependent mesh geometries. It can be observed that diametrically opposed planets share the same dynamic load as long as geometry is supposed to be constant whereas, above a certain speed, every planet experiences its own dynamic loading when the influence of errors and deflections is included. This observation can be generalised as illustrated in Figure 7 where the maximum load ratio is plotted versus sun-gear speed and planet #1 error amplitudes.

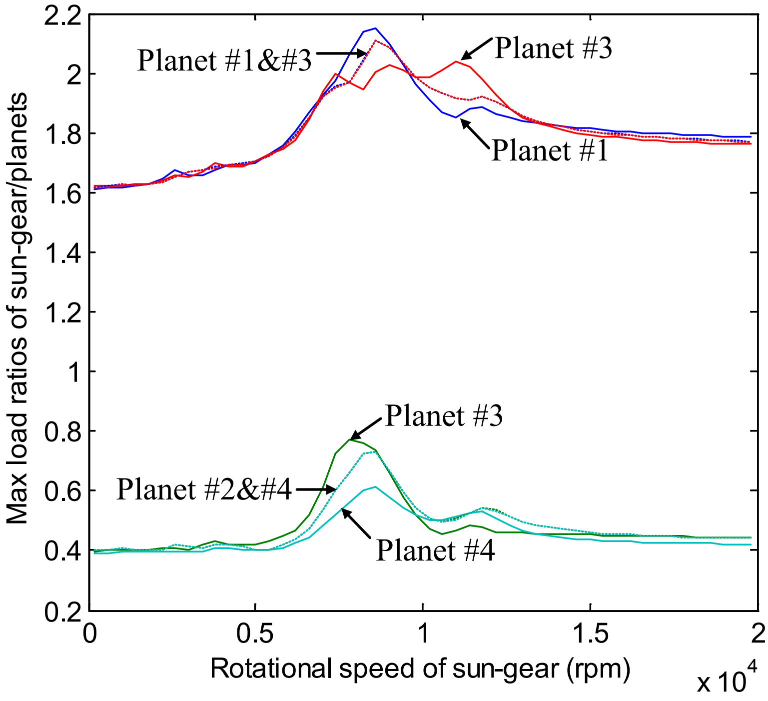

Figure 6 – Maximum dynamic load ratios of sun-gear/planet meshes versus sun-gear rotational speed

Keys:

constant geometry: ······· *varying geometry:* ——

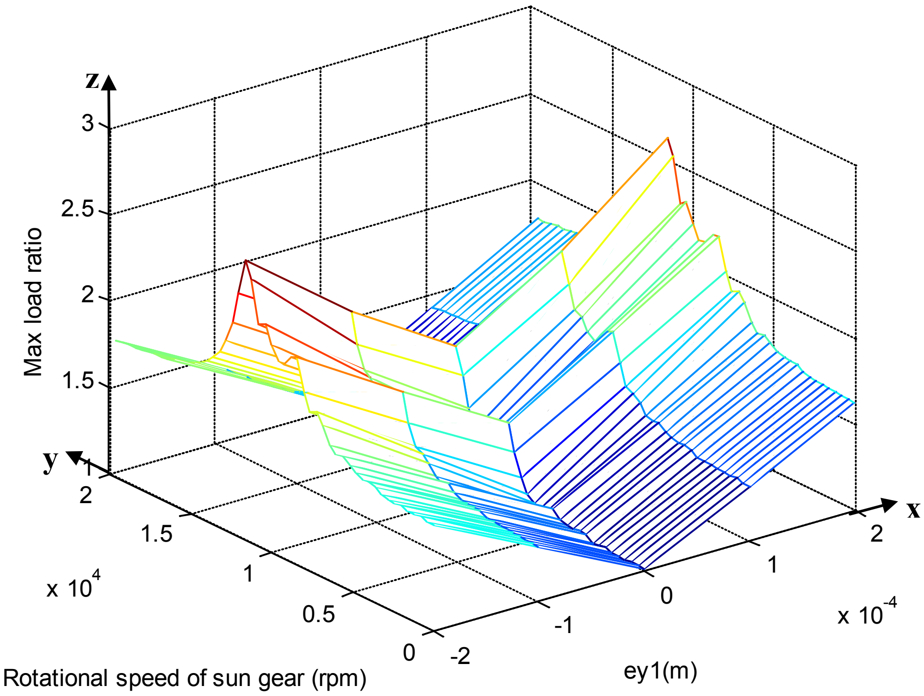

a. Constant geometry

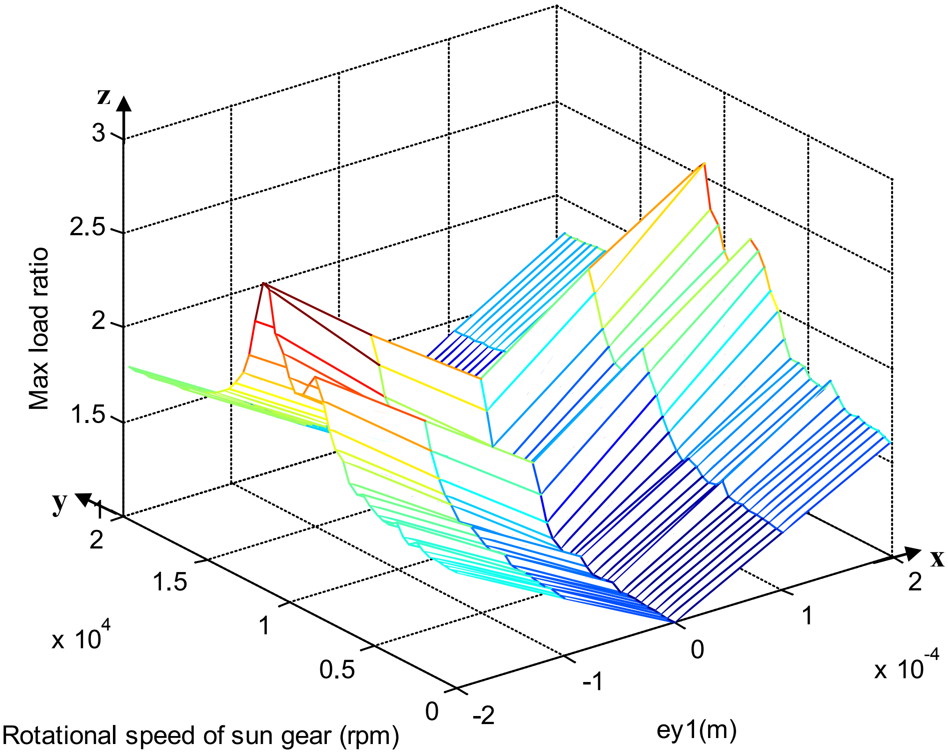

(b) Varying geometry

Figure 7 – Maximum dynamic load ratios of sun-gear/planet meshes versus sun-gear rotational speed and tangential error amplitude *(rotating ring-gear, planetary gear data: Table 1 – case 2)*

Finally, considering trajectories, the two models lead to somewhat different sun-gear and planet trajectories depending if the carrier is fixed or rotating as illustrated in Figure 8.

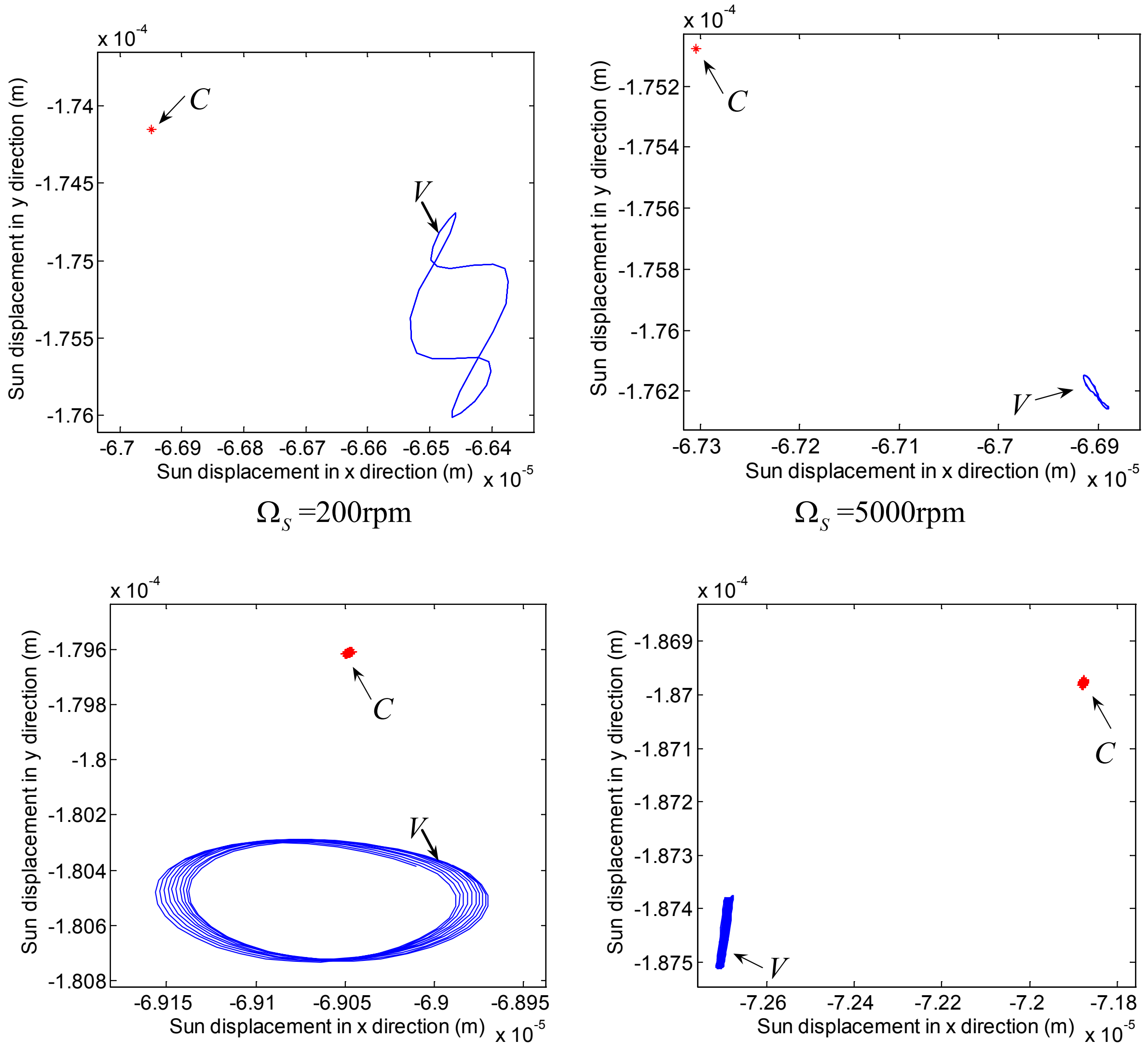

Ω_S =200rpm

Ω_S =5000rpm

Ω_S =12000rpm

Ω_S =18000rpm

Figure 8-a – Trajectory of sun-gear at various speeds (rotating carrier, tangential position error ey1= -0.0002m on planet #1)

Keys:
varying geometry: V ——   *constant geometry: C* —*—

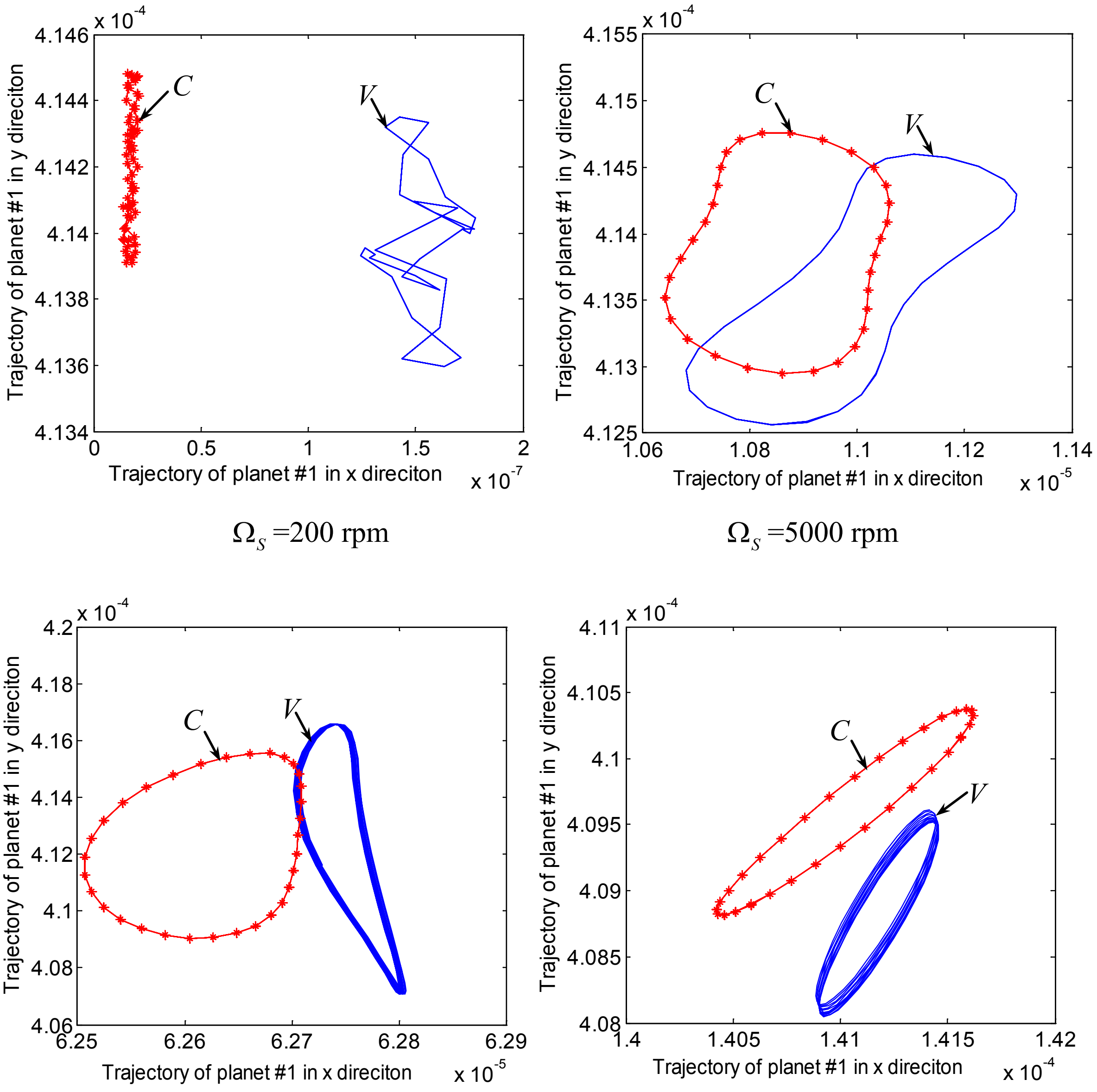

Ω_S =200 rpm

Ω_S =5000 rpm

Ω_S =12000 rpm

Ω_S =18000 rpm

Figure 8-b – Trajectory of planet #1 at various speeds (rotating carrier, tangential position error ey1= -0.0002m on planet #1)

Keys:

varying geometry: V —— *constant geometry: C* —*—

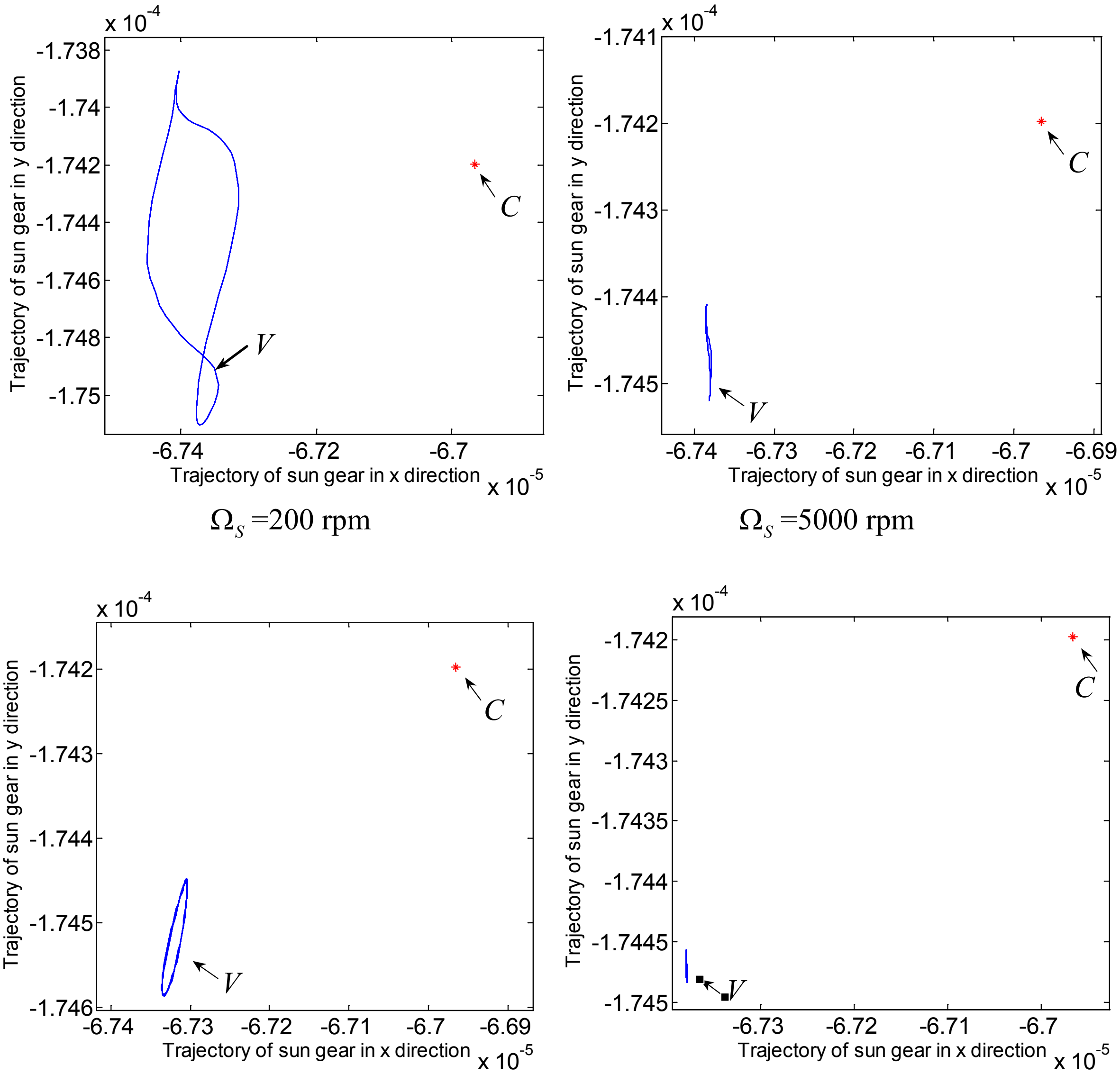

Ω_S =200 rpm Ω_S =5000 rpm

Ω_S =12000 rpm Ω_S =18000 rpm

Figure 8-c – Trajectory of sun-gear at various speeds (fixed carrier, tangential position error ey1= -0.0002m on planet #1)

Keys:

varying geometry: V —— *constant geometry: C* —✱—

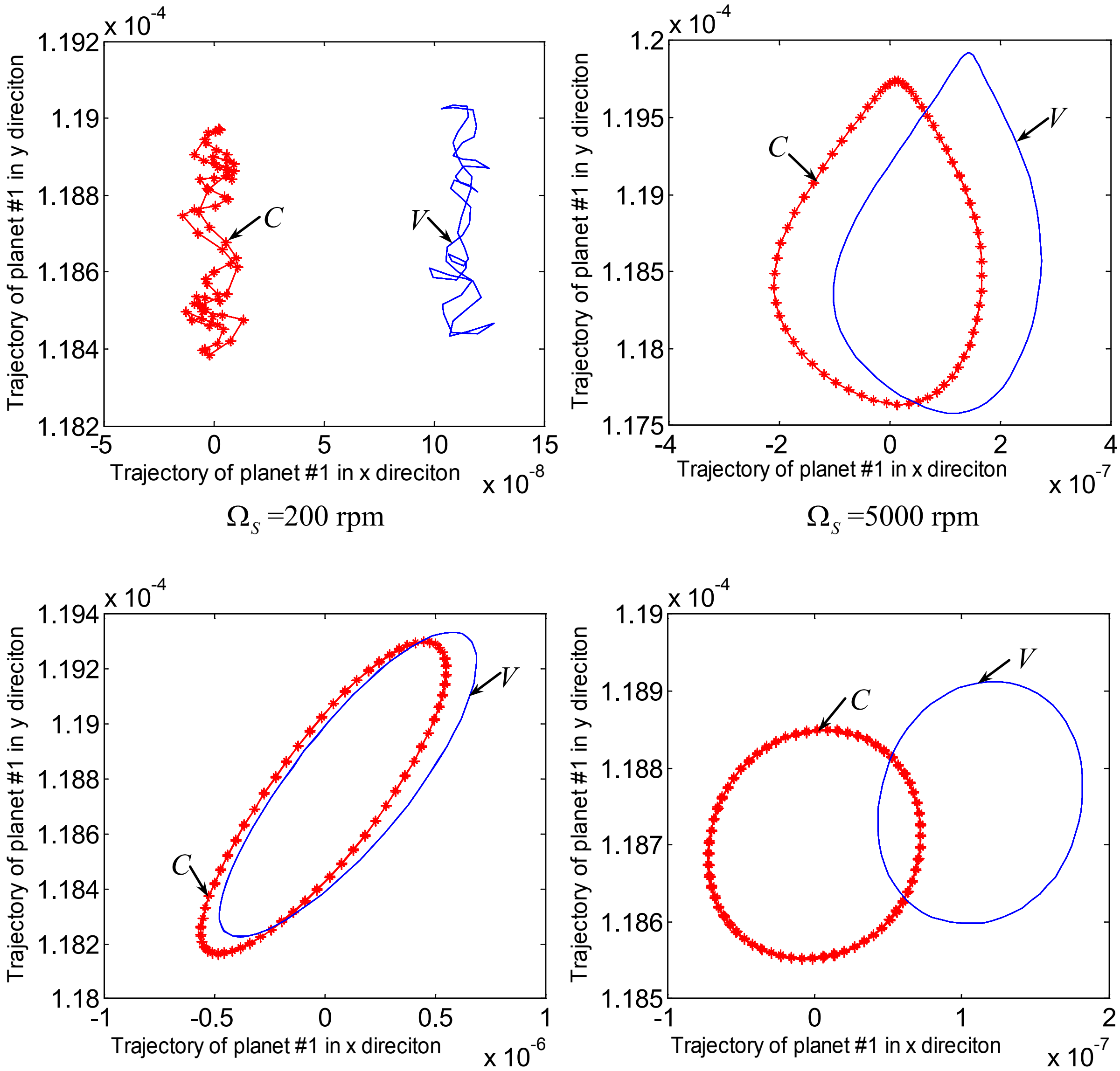

Ω_S =200 rpm

Ω_S =5000 rpm

Ω_S =12000 rpm

Ω_S =18000 rpm

Figure 8-d – Trajectory of planet #1 at various speeds (fixed carrier, tangential position error ey1= -0.0002m on planet #1)

Keys:

varying geometry: V ——   *constant geometry: C* —*—

3.3 – Planet position errors and floating members

The observations about the static behaviour in chapter 3 are partly confirmed for dynamic regimes in Figure 9 which, for a tangential error of -0.2 mm on one planet, show the evolutions of the dynamic load factors versus speed. For a fixed carrier (Figure 9-a), floating planets appears as more interesting over the entire speed range since every planet mesh experiences nearly the same dynamic load. However, the curves in Figure 9-b reveal that floating planets are not as favourable in the case of a rotating carrier since, above a certain speed threshold, significant dynamic overloads are observed. This effect is caused by the combination of the centrifugal forces on the planets and the flexibility of the planet pins leading to a reduction in the sun-gear/planet contact ratios (while ring-gear/planet contact ratios are increased) below the admissible values for continuous motion transfer. Finally, it is to be noted that the positions of the tooth critical speeds are largely independent of the sun-gear and/or planet support stiffness.

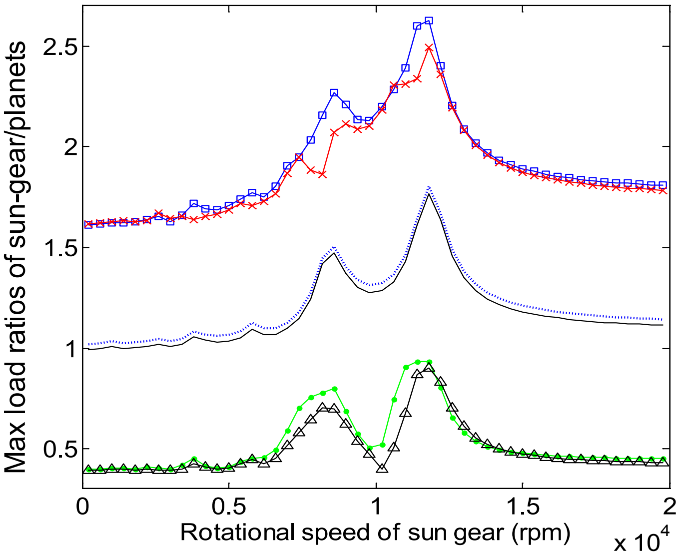

(a) Rotating ring-gear

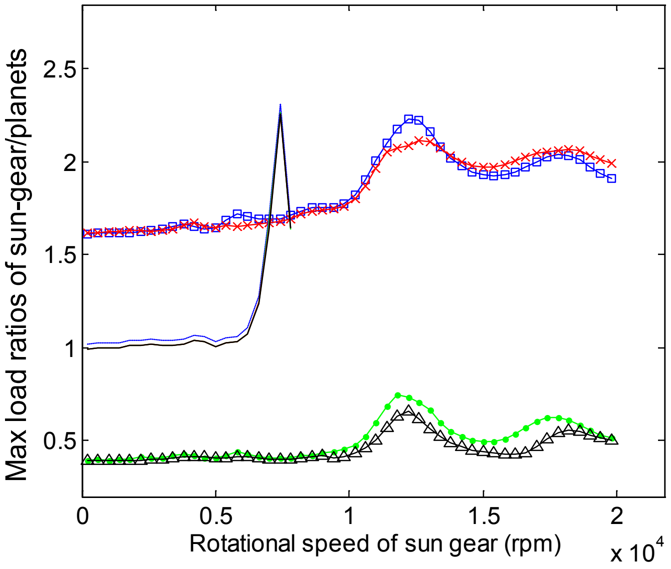

(b) Rotating carrier

Figure 9 – Maximum dynamic load ratios of sun gear/planet meshes versus sun-gear rotational speed - comparisons between floating sun-gear and floating planet arrangements *(tangential position error -0.0002m on planet #1; planetary gear data: Table 3.1 – case 2)*

Keys:

Floating sun-gear: sun-gear/planet #1, #2, #3, #4 —□— —●— —×— —△—

Floating planets: *sun-gear/planet #1* ┈┈┈ *sun-gear/planet #2,3,4* ——

4 – Influence of sun-gear eccentricity

4.1 – Static behaviour

Figure 10-a shows the quasi-static load sharing variations over one revolution of the sun-gear which exhibits an eccentricity of 0.2 mm. In this case where no central member is allowed to float, sun-gear eccentricity is highly influential leading to overloads as large as 1.6 times the nominal load. Each planet sequentially withstands the maximum mesh force in accordance with the angular positions successively taken by the eccentricity vector (following the sun-gear rotation).

The mesh frequency is also visible on the load signals and it can be noticed that it is modulated by the once-per-revolution frequency associated with the sun-gear eccentricity (Figure 10-b). The introduction of either a floating sun-gear or floating planets (Figures 11-a & b) dramatically improve the load sharing amongst the planets and, even if some slight fluctuations are still visible, the corresponding amplitudes are minimal.

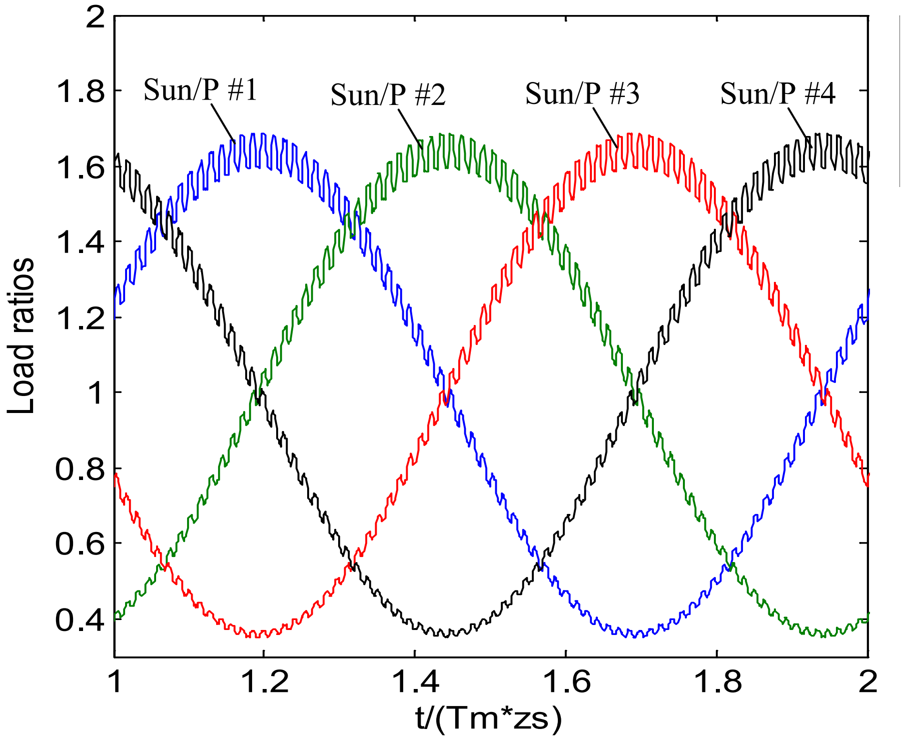

(a) Load ratios on sun-gear/planet meshes *(rigid mounts)*

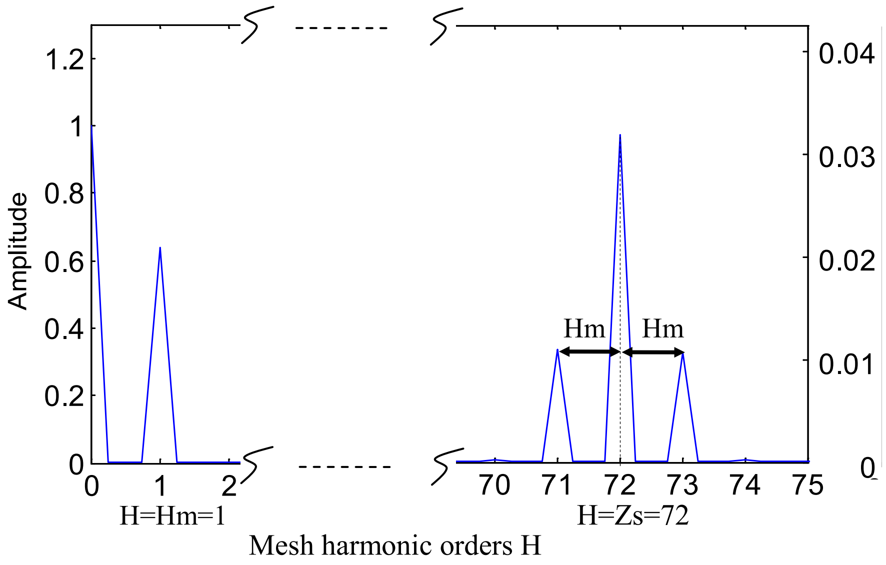

(b) Spectrum of the load ratio function for sun-gear/planet #1

Figure 10 – Tooth loads on sun-gear/planets and load spectrum *(rigid mounts)*

(rotating ring-gear, an eccentricity es = 0.0002m on sun-gear,

Zs: tooth number of sun-gear, sun-gear rotational speed $\Omega_S^0 = 200\ rpm$ *)*

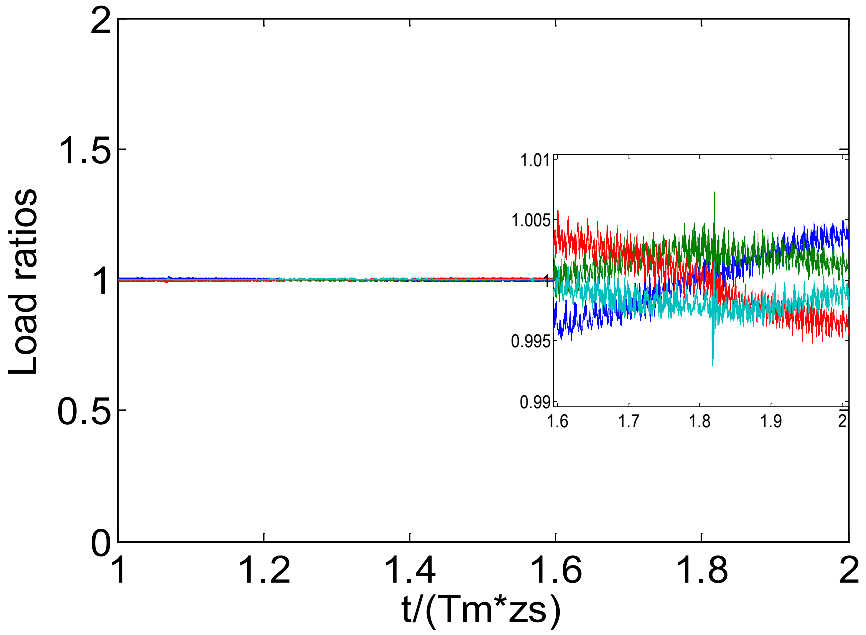

(a) Floating sun-gear

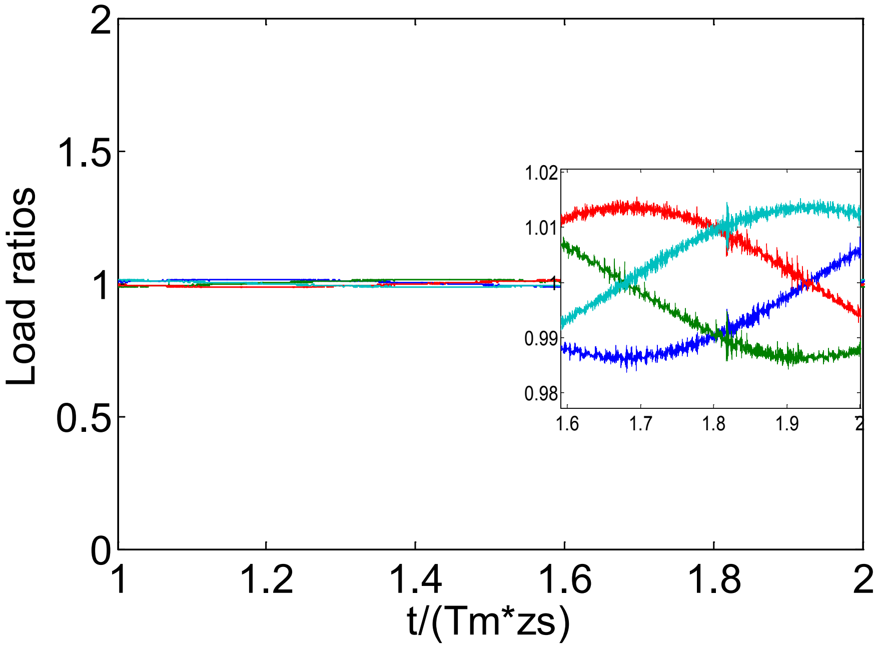

(b) Floating planets

Figure 11 – Tooth loads of sun-gear/planets*(*floating sun-gear and planets*, rotating ring-gear, an eccentricity es : 0.0002m on sun-gear, sun-gear rotational speed: 200 rpm)*

4.2 – Dynamic behaviour

The previous quasi-static results are now extended by considering a range of speeds on the sun-gear for a PTG with a fixed carrier. Figures 12 & 13 show the maximum and minimum tooth load ratios versus speed for a variety of conditions: a) errorless gears, b) with a 0.2 mm eccentricity on the sun-gear with floating and rigid members. It can be noticed that a sun-gear eccentricity combined with rigid mounts (Figure 10-a) strongly affects tooth load amplitudes: the maxima are about 50% higher whereas the minima drop to zero around 10000 rpm indicating that tooth contacts can be momentary lost at some stage. However, the positions of the tooth critical frequencies are unchanged compared with the errorless case and only the amplitudes are affected. The interest of a floating sun-gear or floating planets is clearly illustrated in Figure 13 where the maximum and minimum tooth loads are much closer to those with errorless gears with the exception of the supercritical area where the amplitudes increase with speed as opposed to what is found in the absence of eccentricities. It seems that, near the tooth critical speeds, floating planets seem more effective than a floating sun-gear. The influence of eccentricity amplitude can be observed in Figure 14 which gives the maximum tooth load ratio versus speed for sun-gear eccentricities of 0.1, 0.2 and 0.3 mm respectively. The two major response peaks remain at the same speed but with higher amplitudes for larger eccentricities. Here again, the supercritical speed area appears as more sensitive to eccentricities since higher dynamic loads are found for larger eccentricity amplitudes. The response curves obtained for a particular PTG with integral contact ratios have been superimposed in the same figure in order to try to separate what is dependent on mesh excitations (which should be largely cancelled when the contact ratios are integer) and what is induced by eccentricity. It can be observed that the dynamic response amplitudes increase over the range of speeds (with a steeper slope at high-speeds) whereas the previously found tooth critical speeds are far less visible but still present suggesting that some energy is transferred between the eccentricity and the mesh excitations.

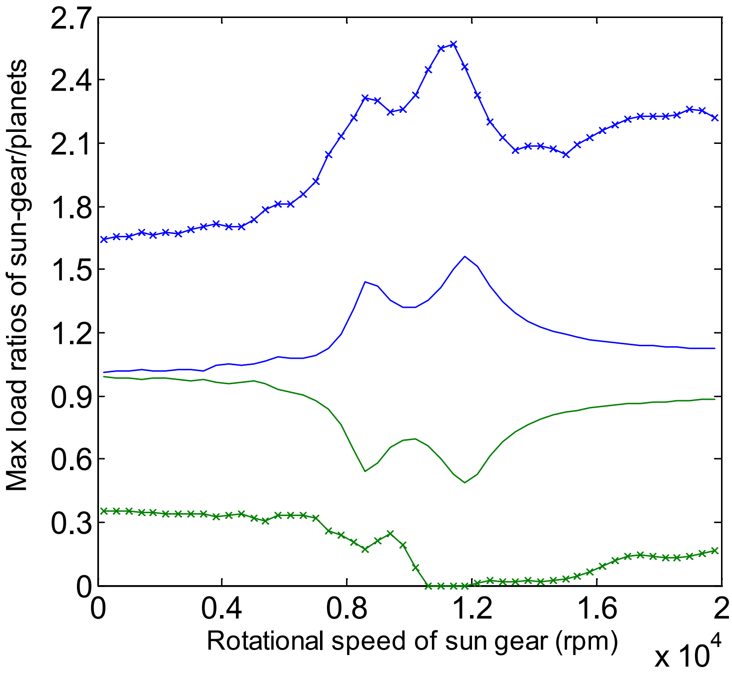

Figure 12 – Maximum dynamic load ratio of sun-gear/planet #1 mesh versus sun-gear rotational speed *(rotating ring-gear, an eccentricity es: 0.0002m on sun-gear)*

Keys:

Configurations without error ——

Configurations with eccentricity error on sun-gear: Rigid mounts —×—

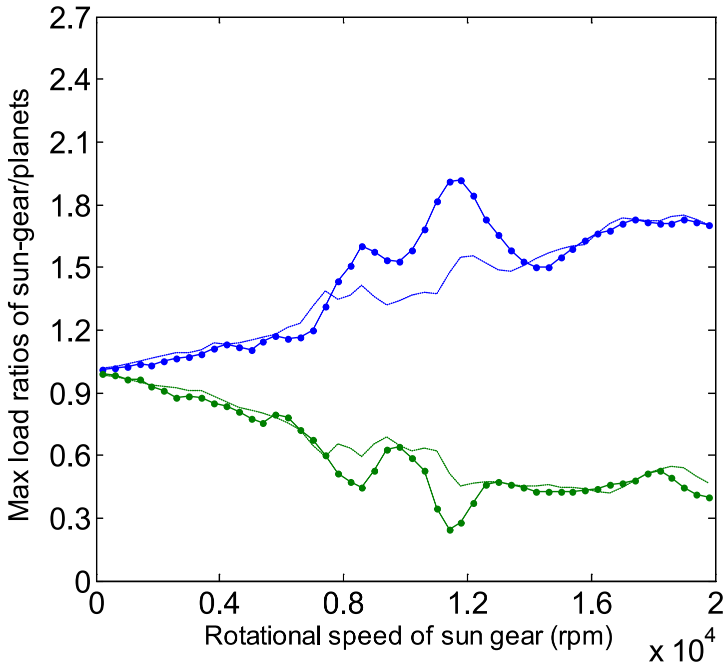

Figure 13 – Influence of floating members on the dynamic tooth load ratio of sun-gear/planet #1 mesh *(rotating ring-gear, an eccentricity es: 0.0002m on sun-gear)*

Keys:

1) floating sun-gear —●— *2) floating planets* ··········

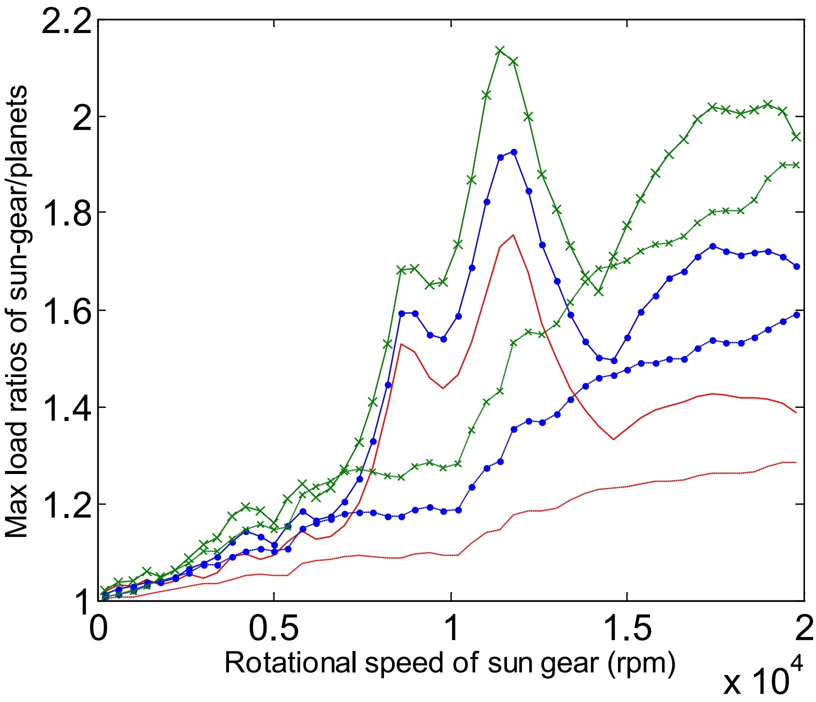

Figure 14 – Maximum tooth load ratio of sun-gear/planet #1 mesh versus sun-gear rotational speed *(floating sun-gear, rotating ring-gear, sun-gear eccentricity is es)*

Keys:

Varying mesh stiffness : es = 0.0001m —; *es = 0.0002m* —•— ; *es = 0.0003m* —×— ;

Constant mesh stiffness : es = 0.0001m —; *es = 0.0002m* —•— ; *es = 0.0003m* —×— ;

Based on the previous findings for PTGs with fixed carriers, floating planets seem advantageous in terms of load sharing amongst the planets but, for a rotating carrier, Figure 15 reveals that, above a certain speed threshold, the dynamic behaviour is strongly deteriorated whereas the use of a floating sun-gear remains interesting. This is explained by the combined influence of the centrifugal effects and pin flexibility which increases the sun-gear/planet centre-distances beyond the limit of continuous meshing (contact ratio larger than one) thus giving rise to contact losses and shocks.

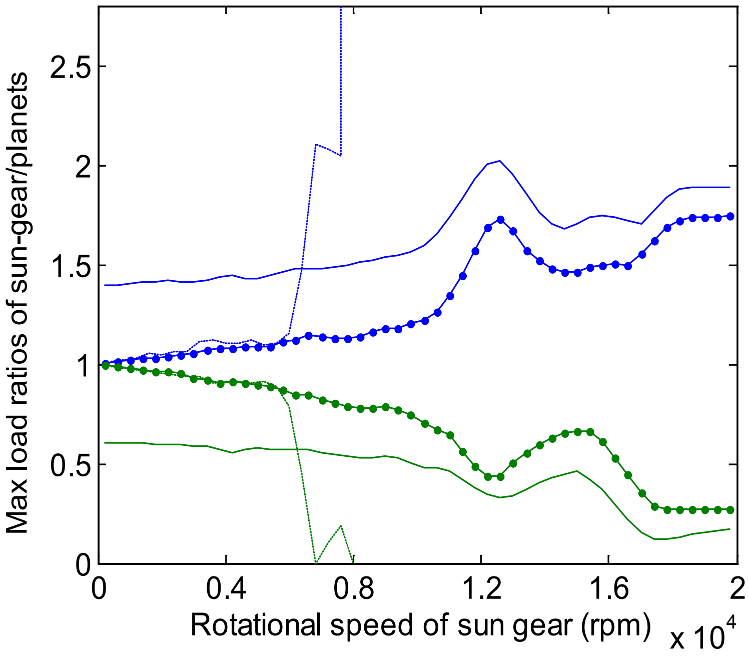

Figure 15 – Maximum dynamic load ratio of sun-gear/planet #1 mesh versus sun-gear rotational speed *(rotating carrier, sun-gear eccentricity es: 0.0002m)*

Keys:

1) rigid mounts —— *2) floating sun-gear* —●— *3) floating planets* ┈┈┈

4.3 – Influence of one planet eccentricity

4.3.1 – Static behaviour

An eccentricity of 0.1 mm is now introduced on planet #1 and the following conditions are considered: i) floating sun-gear or floating planets, ii) fixed and rotating carrier. The quasi-static load distributions for rigid mounts are given in Figure 16 which reveal that diametrically opposed planets share the same load as is the case for planet position errors [50], [100], [102].

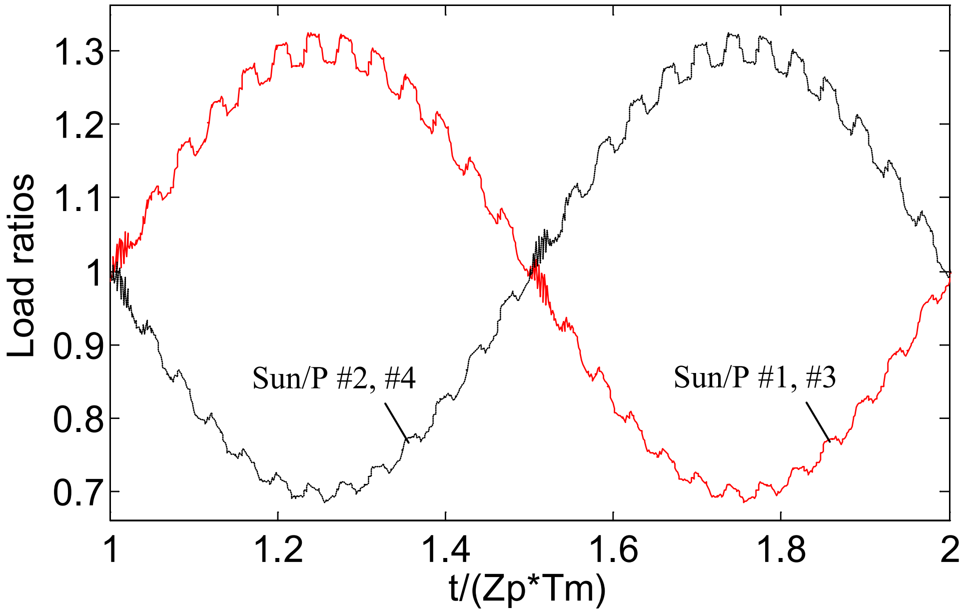

Figure 16 – Static load ratios of sun-gear/planet meshes

(floating sun-gear, rotating ring-gear, an eccentricity e1: 0.0001m, initial angle $\lambda_1 = 0°$ *on planet #1, Zp: the tooth number of planet; Tm: mesh period)*

4.3.2 – Dynamic behaviour

The corresponding dynamic tooth load curves are shown in Figures 17 and 18 which represent the variations of the maximum dynamic-to-static mesh force ratio versus sun-gear speed. The following conclusions can be drawn:

a) Floating planets seem more effective in this case too but mostly for fixed carriers since centrifugal effects strongly limit the speed range of interest for a rotating carrier (Figure 18).

b) For rigid members, eccentricities lead to contact losses at the major tooth critical speed which, of course, are detrimental both from a noise and reliability viewpoint,

c) In the case of floating sun-gear, for a fixed carrier, it can be observed that diametrically opposed planets exhibit nearly the same dynamic response (although only one planet has an eccentricity) thus extending the observations in quasi-static conditions. This symmetry, however, does not appear anymore when a rotating carrier is considered.

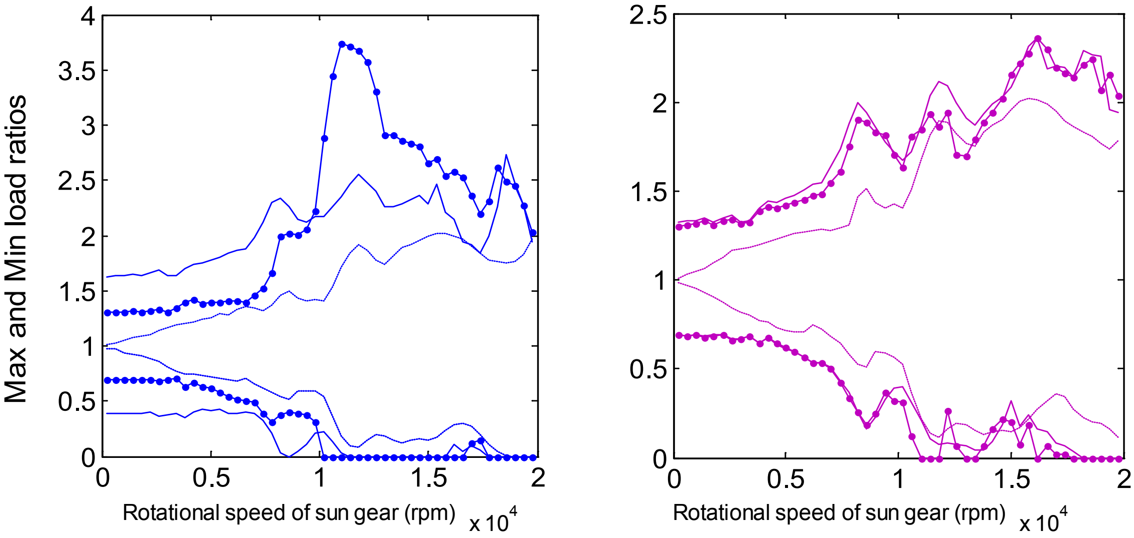

(a) sun/planet #1 (b) sun/planet #2

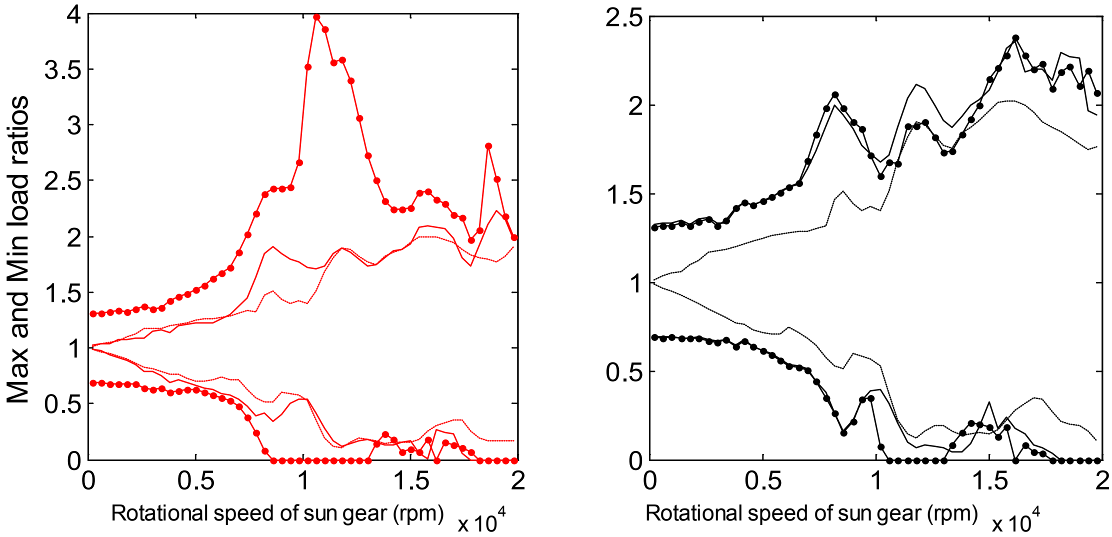

(c) sun/planet #3 (d) sun/planet #4

Figure 17 – Maximum and minimum load ratios for sun-gear/planet meshes versus sun-gear rotational speed *(rotating ring-gear, an eccentricity e1: 0.0001m on planet #1)*

Keys:

1) rigid mounts —— *2) floating sun-gear*—•— *3) floating planets* ——

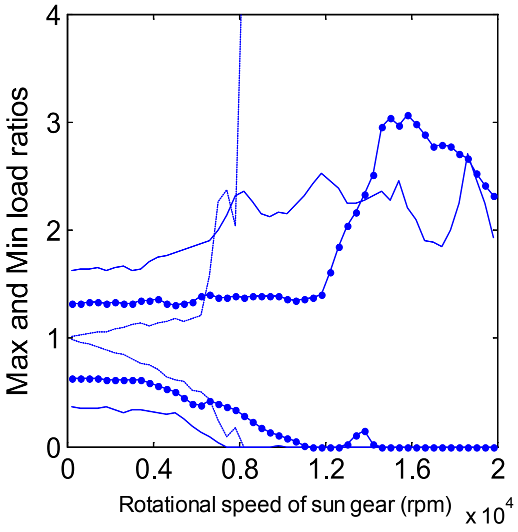

(a) sun/planet #1

(b) sun/planet #2

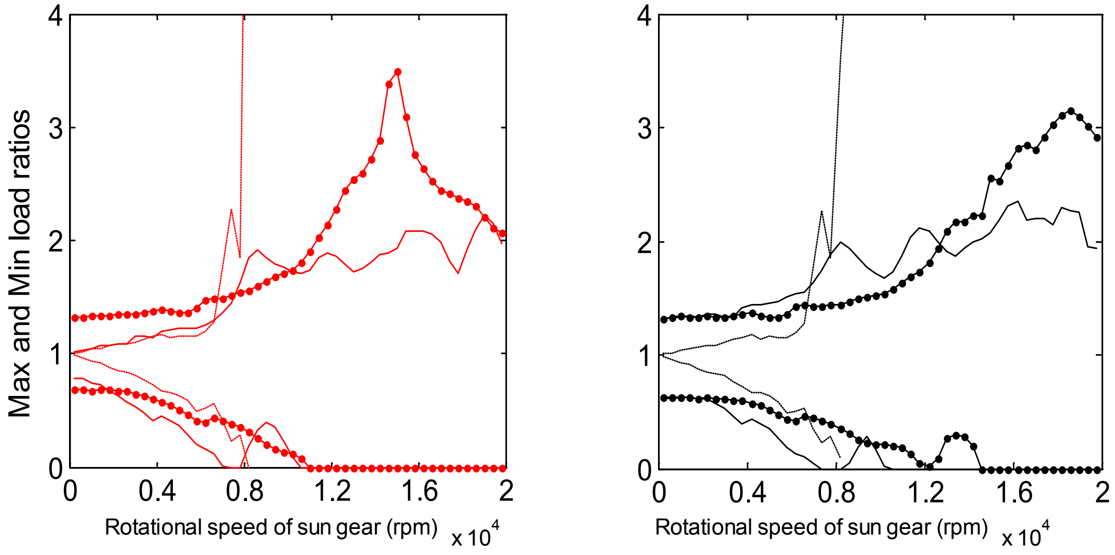

(c) sun/planet #3

(d) sun/planet #4

Figure 18 – Maximum and minimum load ratios for sun-gear/planet meshes versus sun-gear rotational speed *(rotating carrier, an eccentricity e1: 0.0001m on planet #1)*

Keys:

1) rigid mounts —— *2) floating sun-gear*—•— *3) floating planets* ——

5 – Conclusion

In the particular case of planet position error, the dynamic results in this chapter show that the couplings between the errors, the DOFs and the mesh geometry and excitations are influential in systems with rotating carriers, mostly at high speeds. The major differences between the models have been reported on sun-gear and planet trajectories whereas dynamic tooth loads appear as less sensitive to these dynamic interactions unless very large errors are considered. From a practical viewpoint, it has been confirmed that, for a fixed carrier, floating planets are superior to floating sun-gear arrangements with regard to planet loading. Similar conclusions can be drawn for rotating carriers as long as the centrifugal forces on the planets are not too large.

Considering eccentricities, the results show that, as opposed to classic parallel axis gears, tooth loading in PTGs can be very sensitive to this kind of defect when no central member is allowed to float, even in static conditions. From a practical viewpoint, floating planets seem, here again, to be an interesting solution for planet load sharing as long as the carrier is fixed. The situation is different when it comes to rotating carriers for which centrifugal forces at very high-speeds are detrimental because they reduce the actual sun-gear/planet contact ratios. As far as dynamic tooth loads are considered, eccentricities do not introduce additional critical speeds but lead to more complex response spectra with modulation sidebands. For fixed ring-gear sets, it seems that some of the quasi-static properties (as exposed by Singh [50], [102] for instance) can be extended to dynamic load sharing (equal loads on diametrically opposed planets) whereas this symmetry is not observed any longer with rotating carriers at high-speeds.

CONCLUSIONS
–
PERSPECTIVES

An original dynamic model of planetary gears has been set up in which the influences of errors and degrees-of-freedom on gear mesh geometry and excitations are coupled. The theoretical developments rely on the formalism of infinitesimal displacement screws for lumped parameter models. It has been demonstrated that the model can predict actual static load sharing between the planets for a variety of gear geometries and loading conditions. Extensions to high-speed applications are straightforward and some dynamic effects have been emphasized. It has been found that floating planets can be an interesting alternative to the classic floating sun-gear arrangement except for high-speed rotating carriers in which centrifugal forces on flexible elements can substantially deteriorate the meshing conditions (sun-gear / planet centre-distances can become too large thus leading to poor contact ratios). The results have confirmed that tangential planet errors had a much stronger influence on dynamic tooth loads than the radial errors suggesting that pin-hole tolerances in the tangential directions are critical. As opposed to classic gears, it has been demonstrated that eccentricities can be highly influential on load sharing especially when no member is allowed to float. The redundant power paths render the system hyper-static with a number of interconnected contacts and an eccentricity on one member strongly perturbs the power flow in the mechanism by unloading certain contacts and overloading some others. Eccentricities do not introduce additional tooth critical speeds but a general increase in the vibration level as speed increases. Here again, floating members appear as effective with the same limitation on floating planets for rotating carriers at high-speeds.

The proposed model has been kept conceptually simple and a number of improvements or extensions are possible. The mesh stiffness model can be refined with minimum effort and more realistic varying mesh stiffness per unit of contact length can be implemented based on the works of Weber and Banaschek, Lundberg for instance. Perfect tooth geometry has been considered with no deviations from involute flanks which, in actual systems, should be replaced by teeth with profile and lead modifications. The corresponding theory has already been developed [56] and, using the same modelling strategy, tooth modifications can be readily introduced in the present work. More realistic and/or accurate modelling of some structural parts could also be developed and inserted in the dynamic simulations based on the results of Abousleiman et al. [56] who combined sub-structuring for the elements with linear behaviour and non-linear models for the tooth contacts. Finally, the experimental evidence remains sparse; a number of interesting results by General Motors (Dr. Avinash Singh) and the Ohio State University (Dr. Ahmet Kahraman) have been used for validation purposes throughout this memoir but most of them have been obtained in quasi-static conditions. Similar measurements in high-speed application would definitely be a breakthrough in the analysis of planetary gear dynamics.

REFERENCES

[1]. LYNWANDER P., Gear Drive Systems: Design and Application (Mechanical Engineering Series), 1983, 432 p. ISBN-10 0824718968.

[2]. WEBCARS. BMW X6 ActiveHybrid at the 2009 Frankfurt Motor Show Formally Released [on line] Disponible on: <*http://www.webcars.com.cn/review/20091110 /21569/photo_3. html*> (consulted on 27.01.2012)

[3]. BMW France. La Réponse Adaptée à la Situation [on line] Disponible on: <*http://www.bmw.fr/fr/fr/insights/technology/efficient_dynamics/phase_2/activehybrid/ x6_concept_vehicle_two_mode.html*> (consulted on 27.01.2012)

[4]. Vbulletin Solutions. PPRuNe Forums [on line] Disponible on: <*http://www.pprune.org/http://www.pprune.org/rotorheads/368283-heli-ditch-north-sea-g-redl-not-condolences-18.html*> (consulted on 27.01.2012)

[5]. LIGATA H., KAHRAMAN A., and SINGH A., An Experimental Study of the Influence of Manufacturing Errors on the Planetary Gear Stresses and Planet Load Sharing, Journal of Mechanical Design, 2008, 130(4), p. 041701.

[6]. HEATH G. and BOSSLER R., Advanced Rotorcraft Transmission (ART) Program - Final Report, NASA Contractor Report CR-191057, NASA, 1993.

[7]. WEBER C., The Deformations of Loaded Gears and the Effects on their Load Carrying Capacity, British Dept. of Scientific and Industrial Research, Sponsored Research (Germany), 1949, Report no. 3.

[8]. WEBER, C. and BANASCHEK, K., Formänderung und Profilrücknahme bei Gerad- und Schrägverzahnten Antriebstechnik, F. Vieweg und Sohn, Braunschweig, 1953, vol. 11.

[9]. TAVAKOLI M.S. and HOUSER D.R., Optimum Profile Modifications for the Minimization of Static Transmission Errors of Spur Gears, ASME Journal of Mechanisms Transmissions and Automation in Design, 1986, 108, pp. 86-95.

[10]. LIN H.H., TOWNSEND D.P. and OSWALD F.B., Profile Modification to Minimize Spur Gear Dynamic Loading, Proceedings of the 5th ASME International Power Transmission and Gearing Conference, Chicago, 1989, 1, pp. 455-465.

[11]. O'DONNELL W.J., The Additional Deflection of a Cantilever due to the Elasticity of the Support, ASME, J. Applied Mechanics, 1960, 27, pp. 461-464.

[12]. O'DONNELL W.J., Stresses and Deflections in Built-In Beams, 1963, 85, pp. 265-273.

[13]. ATTIA A.Y., Deflection of Spur Gear Teeth Cut in Thin Rims, ASME J. Eng. Ind., 1964, 86, pp. 333-342.

[14]. CORNELL R.W., Compliance and Stress Sensitivity of Spur Gear Teeth, ASME J. Mech. Des., 1981, 103, pp. 447-459.

[15]. LUNDBERG G., Elastische Berührung Zweier Halbraüme, Forschung im Ingenieurwesen, 1939, 10(5), pp. 201-211.

[16]. ISO/DIS 6336-1.2, Calculation of Load Capacity of Spur and Helical Gears (Part I: Basic Principles and Influence Factors), Draft International Standard, 1990, pp. 87-95.

[17]. CHABERT G., DANG TRON T. and MATHIS R., An Evaluation of Stresses and Deflection of Spur Gear Teeth under Strain, ASME, Journal of Engineering for Industry, 1974, 96, pp. 85-93.

[18]. WANG K.L. and CHENG H.S., A Numerical Solution to the Dynamic Load, Film Thickness, and Surface Temperatures in Spur Gears, Part I: Analysis, ASME Journal of Mechanical Design, 1981, 103, pp. 177-187.

[19]. SAINSOT A., Analyse du Contact entre Dentures des Engrenages Cylindriques de Réducteurs, Thèse de Docteur Ingénieur: Institut National des Sciences Appliquées de LYON, 1989, 295p.

[20]. CAI Y. and HAYASHI T., The Linear Approximated Equation of Vibration for a Pair of Spur Gears: Theory and Experiment, Proceedings of the 6th ASME International Power Transmission and Gearing Conference, Phoenix, 1992, 2, pp. 521-528.

[21]. KUCUKAY F., Dynamic Behaviour of High Speed Gears, Proceedings of the 3th IMechE International Conference on Vibration in Rotating Machinery, 1984, C317/84 pp. 81-90.

[22]. IWATSUBO T., ARII S. and KAWAI R., Coupled Lateral-Torsional Vibration of Rotor System Trained by Gear (Part 1. Analysis by Transfer Matrix Method), JSME, 1984, 27(224), pp. 271-277.

[23]. VELEX P. and SAADA A., A Model for the Dynamic Behaviour of Multistage Geared Systems, Proc. 8th IFToMM World Congress, Prague, 1991, 2, pp. 621-624.

[24]. MAATAR M. and VELEX P., An Analytical Expression for the Time-Varying Contact Length in Perfect Cylindrical Gears: Some Possible Applications in Gear Dynamics, Journal of Mechanical Design, 1996, 118(4), pp.586-589.

[25]. SEAGER D. L., Conditions for the Neutralization of Excitation by the Teeth in Epicyclic Gearing, Journal of Mechanical Engineering Science, 1975, 17, pp. 293-298.

[26]. KAHRAMAN A., Planetary Gear Train Dynamics, ASME Journal of Mechanical Design, 1994, 116, pp. 713-720.

[27]. KAHRAMAN A. and BLANKENSHIP G. W., Planet Mesh Phasing in Epicyclic Gear Sets, Proceedings of the International Gearing Conference, Newcastle UK, 1994, pp. 99-104.

[28]. PARKER R.G. A Physical Explanation for the Effectiveness of Planet Phasing to Suppress Planetary Gear Vibration, Journal of Sound and Vibration, 2000, 236(4), pp. 561-573.

[29]. PARKER R.G. and LIN J., Mesh Phasing Relationships in Planetary and Epicyclic Gears, Journal of Mechanical Design, 2004, 126(2), pp. 365-370.

[30]. VELEX P. and FLAMAND L., Dynamic Response of Planetary Trains to Mesh Parametric Excitations, Journal of Mechanical Design, 1996, 118, pp. 7-14.

[31]. VELEX P. and MAATAR M., A Mathematical Model for Analyzing the Influence of Shape Deviations and Mounting Errors on Gear Dynamic Behaviour, Journal of Sound and Vibration, 1996, 191(5), pp. 629-660.

[32]. STOCK DRIVE PRODUCTS / STERLINIG INSTRUMENT, Elements of Metric Gear Technology [on line] Disponible on: <*http://www.sdp-si.com/D785/HTML1/D785T108_4.html*> (consulted on 27.01.2012)

[33]. BODAS A. and KAHRAMAN A., Influence of Carrier and Gear Manufacturing Errors on the Static Load Sharing Behavior of Planetary Gear Sets, JSME Int. J., Ser. C, 2004, 47, pp. 908-915.

[34]. HARRIS S. L., Dynamic Loads on the Teeth of Spur Gears, Proceedings of the Institution of Mechanical Engineers, 1958, 172, pp. 87-112.

[35]. VELEX P. and AJMI M., On the Modelling of Excitations in Geared Systems by Transmission Errors, Journal of Sound and Vibration, 2006, 290(3-5), pp. 882-909.

[36]. HIDAKA T., TERAUCHI Y. and NAGAMURA K., Dynamic Behavior of Planetary Gears (1st Report: Load Distribution), Bulletin of the JSME, 1976, 19(138), pp. 1563-1570.

[37]. HIDAKA T., TERAUCHI Y. and DOHI K., On the Relation between the Run Out Errors and the Motion of the Center of Sun Gear in a Stoeckicht Planetary Gear, Bulletin of the JSME, 1979, 22, pp. 748-754.

[38]. HIDAKA T., TERAUCHI Y. and NAGAMURA K., Dynamic Behavior of Planetary Gear (7th Report: Influence of the Thickness of the Ring Gear), Bulletin of the JSME, 1979, 22(170), pp. 1142-1149.

[39]. HIDAKA T., TERAUCHI Y. and FUJII M., Analysis of Dynamic Tooth Load on Planetary Gear, Bulletin of the JSME, 1980, 23(176), pp. 315-323.

[40]. MULLER W.H., Epicyclic Drive Trains, Wayne State University Press, Detroit, 1982.

[41]. SEAGER D. L., Load Sharing among Planet Gears, 1970, SAE Paper No. 700178.

[42]. AUGUST R. and KASUBA R. Torsional Vibrations and Dynamic Loads in a Basic Planetary Gear System, ASME J. Vib., Acoust., Stress, Reliab. Des., 1986, 108(3), pp. 348-353.

[43]. JARCHOW F., Development Status of Epicyclic Gears, ASME International Power Transmission and Gearing Conference, Chicago, 1989.

[44]. KAHRAMAN A., Static Load Sharing Characteristics of Transmission Planetary Gear Sets: Model and Experiment, 1999, SAE Paper No. 1999-01-1050.

[45]. KAHRAMAN A., Load Sharing Characteristics of Planetary Transmissions, Mechanism and Machine Theory, 1994, 29(8), pp. 1151-1165.

[46]. KAHRAMAN A. and VIJAYAKAR S., Effect of Internal Gear Flexibility on the Quasi-Static Behavior of a Planetary Gear Set, Journal of Mechanical Design, 2001, 123, pp. 408-415.

[47]. SINGH A., Application of a System Level Model to Study the Planetary Load Sharing Behavior, Journal of Mechanical Design, 2005, 127, pp. 469-476.

[48]. SINGH A., KAHRAMAN A., and LIGATA H., Internal Gear Strains and Load Sharing in Planetary Transmissions: Model and Experiments, Journal of Mechanical Design, 2008, 130(7), p. 072602.

[49]. SINGH A., Implications of Planetary Load Sharing on Transmission Torque Capacity, 6th International CTI Symposium "Innovative Automotive Transmissions", Berlin, Germany, 2007.

[50]. SINGH A., Load Sharing Behavior in Epicyclic Gears: Physical Explanation and Generalized Formulation, Mechanism and Machine Theory, 2010, 45(3), pp. 511-530.

[51]. HAYASHI T., Li Y., HAYASHI I., ENDOU K., and WATANABE W., Measurement and Some Discussions on Dynamic Load Sharing in Planetary Gears, Bulletin of the JSME, 1986, 29, pp. 2290-2297.

[52]. CHEON G.J. and PARKER R.G., Influence of Manufacturing Errors on the Dynamic Characteristics of Planetary Gear Systems, Journal of Mechanical Science and Technology, 2004, 18(4), pp. 606-621.

[53]. CHEON G.J. and PARKER R.G., Influence of Bearing Stiffness on the Static Properties of a Planetary Gear System with Manufacturing Errors, Journal of Mechanical Science and Technology, 2004, 18, pp. 1978-1988.

[54]. MONTESTRUC A.N., Influence of Planet Pin Stiffness on Load Sharing in Planetary Gear Drives, Journal of Mechanical Design, 2011, 133, p. 014501.

[55]. MONTESTRUC A.N., A Numerical Approach to Calculation of Load Sharing in Planetary Gear Drives, Journal of Mechanical Design, 2010, 132, p. 014503.

[56]. ABOUSLEIMAN V. and VELEX P., A Hybrid 3D Finite Element/Lumped Parameter Model for Quasi-Static and Dynamic Analyses of Planetary/Epicyclic Gear Sets, Mechanism and Machine Theory, 2006, 41(6), pp. 725-748.

[57]. KAHRAMAN A., KHARAZI A.A., and UMRANI M., A Deformable Body Dynamic Analysis of Planetary Gears with Thin Rims, Journal of Sound and Vibration, 2003, 262, pp. 752-768.

[58]. KAHRAMAN A., LIGATA H., and SINGH A., Influence of Ring Gear Rim Thickness on Planetary Gear Set Behavior, Journal of Mechanical Design, 2010, 132, p. 021002.

[59]. HIDAKA T., TERAUCHI Y., and NAGAMURA K., Dynamic Behavior of Planetary Gear (6th Report: Influence of Meshing-Phase), Bulletin of the JSME, 1979, 22(169), pp. 1026-1033.

[60]. AMBARISHA V.K. and PARKER R.G., Suppression of Planet Mode Response in Planetary Gear Dynamics Through Mesh Phasing, Journal of Vibration and Acoustics, 2006, 128, pp. 133-142.

[61]. CUNLIFFE F., SMITH J.D. and WELBOURN D.B., Dynamic Tooth Loads in Epicyclic Gears, Journal of Engineering for Industry, 1974, 96(2), pp. 578-584.

[62]. BOTMAN M., Epicylic Gear Vibrations, Engineering for Industry, 1976, 98(3), pp. 811-815.

[63]. FRATER J.L., AUGUST R. and OSWALD F.B., Vibration in Planetary Gear Systems with Unequal Planet Stiffnesses, 1983, NASA Technical Memorandum No. 83428.

[64]. ANTONY G., Gear Vibration-Investigation of the Dynamic Behaviour of One Stage Epicyclic Gears, 1988, ISBN 9781555895174

[65]. SAADA A. and VELEX P., An Extended Model for the Analysis of the Dynamic Behavior of Planetary Trains, Journal of Mechanical Design, 1995, 117, pp. 241-247.

[66]. ERITENEL T. and PARKER R. G., Modal Properties of Three-Dimensional Helical Planetary Gears, Journal of Sound and Vibration, 2009, 325(1-2), pp. 397-420.

[67]. GUO Y. and PARKER R.G., Sensitivity of General Compound Planetary Gear Natural Frequencies and Vibration Modes to Model Parameters, Journal of Vibration and Acoustics, 2010, 132, p. 011006.

[68]. LIN J. and PARKER R.G., Natural Frequency Veering in Planetary Gears under Design Parameter Variations, Mechanics of Structures and Machines, 2001, 29(4), pp. 411-429.

[69]. PARKER R.G. and WU X., Parametric Instability of Planetary Gears with Elastic Continuum Ring Gears, ASME Journal of Vibration and Acoustics, 2012, in press (DOI: 10.1115/1.4005836).

[70]. PARKER R.G. and WU X., Vibration Modes of Planetary Gears with Unequally Spaced Planets and an Elastic Ring Gear, Journal of Sound and Vibration, 2010, 329, pp. 2265-2275.

[71]. GUO Y. and PARKER R.G., Purely Rotational Model and Vibration Modes of Compound Planetary Gears, Mechanism and Machine Theory, 2010, 45(3), pp. 365-377.

[72]. BLANKENSHIP G.W. and KAHRAMAN A., Steady State Forced Response of a Mechanical Oscillator with Combined Parametric Excitation and Clearance Type Non-Linearity, Journal of Sound and Vibration, 1995, 185(5), pp. 743–765.

[73]. KAHRAMAN A. and BLANKENSHIP G.W., Experiments on Nonlinear Dynamic Behavior of an Oscillator with Clearance and Periodically Time Varying Parameters, Journal of Applied Mechanics, 1997, 64, pp. 217-226.

[74]. MUNRO R.G., The Dynamic Behavior of Spur Gears, PhD Dissertation, Cambridge University, 1962.

[75]. KUBO A., YAMADA K., AIDA T. and SATO S., Research on Ultra High Speed Gear Devices (Reports 1–3), Transactions of the Japan Society of Mechanical Engineers, 1972, 38, pp. 2692-2715.

[76]. KAHRAMAN A. and SINGH A., Non-Linear Dynamics of a Spur Gear Pair, Journal of Sound and Vibration, 1990, 142(1), pp. 49-75.

[77]. BOTMAN M., Vibration Measurements on Planetary Gears of Aircraft Turbine Engines, 1980, 17(5), pp. 351–357.

[78]. SUN T. and HU H., Nonlinear Dynamics of a Planetary Gear System with Multiple Clearances, Mechanism and Machine Theory, 2003, 38(12), pp. 1371-1390.

[79]. AMBARISHA V.K. and PARKER R.G., Nonlinear Dynamics of Planetary Gears Using Analytical and Finite Element Models, Journal of Sound and Vibration, 2007, 302(3), pp. 577-595.

[80]. LIN J. and PARKER R.G., Structured Vibration Characteristics of Planetary Gears with Unequally Spaced Planets, Journal of Sound and Vibration, 2000, 233(5), pp. 921-928.

[81]. BAHK C.J. and PARKER R.G., Analytical Solution for the Nonlinear Dynamics of Planetary Gears, Journal of Computational and Nonlinear Dynamics, 2011, 6(2), pp. 021007.

[82]. GUO Y. and PARKER R.G., Dynamic Modeling and Analysis of a Spur Planetary Gear Involving Tooth Wedging and Bearing Clearance Nonlinearity, European Journal of Mechanics-A/Solids, 2010, 29(6), pp. 1022-1033.

[83]. JARCHOW F. and VONDERSCHMIDT R., Tooth-Forces in Planetary Gears, Proceedings of the International Symposium on Gearing and Power Transmissions, 1981, 11, pp. 327-332.

[84]. MA P. and BOTMAN M., Load Sharing in a Planetary Gear Stage in the Presence of Gear Errors and Misalignments, ASME J. Mech. Trans., 1984, 107, 84-DET-54, 7p.

[85]. KASUBA R. and AUGUST R., Gear Mesh Stiffness and Load Sharing in Planetary Gearing, ASME 4th Power Transmission Conference, Transactions of the ASME, 1984, 84-DET-229.

[86]. KAHRAMAN A., Natural Modes of Planetary Gear Trains, Journal of Sound and Vibration, 1994, 173(1), pp. 125-130.

[87]. KAHRAMAN A., Free Torsional Vibration Characteristics of Compound Planetary Gear Sets, Mechanism and Machine Theory, 2001, 36, pp. 953-971.

[88]. KIRACOFE D. R. and PARKER R. G., Structured Vibration Modes of General Compound Planetary Gear Systems, Journal of Vibration and Acoustics, 2007, 129, pp. 1-16.

[89]. WU X. and PARKER R.G., Modal Properties of Planetary Gears with an Elastic Continuum Ring Gear, Journal of Applied Mechanics, 2008, 75, p. 031014.

[90]. ABOUSLEIMAN V., Comportement Dynamique des Trains Planétaires et Épicycloïdaux—Conditions de Contact et Influence de Sous-Ensembles Flexibles, Ph.D. Dissertation, INSA Lyon, 2004, 04ISAL0054, 226 p.

[91]. HIDAKA T. et al., Dynamic Behavior of Planetary Gear (3rd Report: Displacement of Ring Gear in Direction of Line of Action), Bulletin of the JSME, 1977, 20(150), pp. 1663-1672.

[92]. YUKSEL C. and KAHRAMAN A., Dynamic Tooth Loads of Planetary Gear Sets having tooth profile wear, Mechanism and Machine Theory, 2004, 39(7), pp. 695-715.

[93]. PARKER R.G., AGASHE V., and VIJAYAKAR S.M., Dynamic Response of a Planetary Gear System Using a Finite Element/Contact Mechanics Model, Journal of Mechanical Design, 2000, 122, pp. 304-310.

[94]. PARKER R.G., VIJAYAKAR S.M., and IMAJO T., Non-Linear Dynamic Response of a Spur Gear Pair: Modelling and Experimental Comparisons, Journal of Sound and Vibration, 2000, 237(3), pp. 435-455.

[95]. HELSEN J., VANHOLLEBEKE F., MARRANT B., VANDEPITTE D., and DESMET W., Multibody Modelling of Varying Complexity for Modal Behaviour Analysis of Wind Turbine Gearboxes, Renewable Energy, 2011, 36(11), pp. 3098-3113.

[96]. HELSEN J., VANDEPITTE D. and DESMET W., Flexible Modelling of Wind Turbine Gearboxes with Special Focus on Shaft Flexibilities, 10th International Conference, Southampton, 2010.

[97]. HELSEN J., VANHOLLEBEKE F., DE CONINCK F., VANDEPITTE D., and DESMET W., Insights in Wind Turbine Drive Train Dynamics Gathered by Validating Advanced Models on a Newly Developed 13.2 MW Dynamically Controlled Test-Rig, Mechatronics, 2011, 21(4), pp. 737-752.

[98]. KIM W., LEE J.Y., and CHUNG J., Dynamic Analysis for a Planetary Gear with Time-Varying Pressure Angles and Contact Ratios, Journal of Sound and Vibration, 2012, 331(4), pp. 883-901.

[99]. INALPOLAT M. and KAHRAMAN A., A Dynamic Model to Predict Modulation Sidebands of a Planetary Gear Set Having Manufacturing Errors, Journal of Sound and Vibration, 2010, 329(4), pp. 371-393.

[100]. LIGATA H., KAHRAMAN A., and SINGH A., A Closed-Form Planet Load Sharing Formulation for Planetary Gear Sets Using a Translational Analogy, Journal of Mechanical Design, 2009, 131, p. 021007.

[101]. INALPOLAT M. and KAHRAMAN A., A Theoretical and Experimental Investigation of Modulation Sidebands of Planetary Gear Sets, Journal of Sound and Vibration, 2009, 323(3-5), pp. 677-696.

[102]. SINGH A., Epicyclic Load Sharing Map — Development and validation, Mechanism and Machine Theory, 2011, 46(5), pp. 632-646.

APPENDIX

1 – Length of mesh lines in contact zone

2 – Time-step Newmark's integration scheme combined with fixed-point procedure and relaxation method

Appendix 1 – Length of mesh lines in contact zone

Under the hypotheses that, at every time step, the mesh parameters are constant, the length of one contact line l in the contact zone is given as:

(1) For spur gears $l = b$ where b is the tooth width

(2) and for helical gears (Figure 1), $l = |A_a A_b|$ where $|A_a A_b|$ is the distance between the two intersecting points between the inclined contact line and the limits of the mesh zone in the base plane, and can be calculated in the following steps:

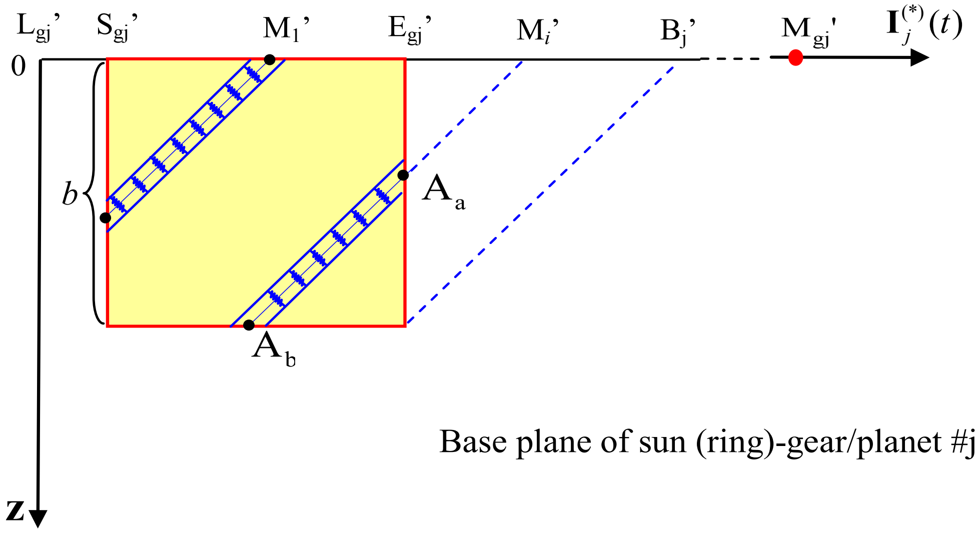

Figure 1 – Length of contact lines in meshing area

(a) At any time t, the position of first contact line in the contact zone on the sun (ring)-gear/planet #j base plane is given by $\mathbf{L}_{gj}'\mathbf{M}_1$ is:

$$\mathbf{L}_{gj}'\mathbf{M}_1' = \left\| \frac{\left|\mathbf{L}_{gj}'\mathbf{M}_{gj}'\right|^{t+\Delta t}}{pb_a} \right\| \tag{1}$$

(b) Whereas, the other contact lines are deduced from:

$$\begin{gathered} \mathbf{L}_{gj}'\mathbf{M}_i' = \mathbf{L}_{gj}'\mathbf{M}_1' + (i-1)\cdot \mathrm{p_{ba}} \qquad i=1,\ 2,\ 3\ldots \\ \mathrm{L_{gj}}'\mathrm{S_{gj}}' \le \mathrm{L_{gj}}'\mathrm{M}_i' \le \mathrm{L_{gj}}'\mathrm{B_j}' \end{gathered} \tag{2}$$

where $\mathrm{p_{ba}}$ is the apparent base pitch

(c) Calculate the coordinates of intersecting points between one contact line and the limit of the mesh zone.

$$\begin{gathered}
A_a=\left(\mathbf{L}_{gj}\,'\mathbf{E}_{gj}^{'},\frac{\mathbf{L}_{gj}\,'\mathbf{M}_i\,'-\mathbf{L}_{gj}\,'\mathbf{E}_{gj}^{'}}{tg\beta_b}\right);\qquad A_b=\left(\mathbf{L}_{gj}\,'\mathbf{M}_i\,'-b\cdot tg\beta_b,b\right)\\
A_c=\left(\mathbf{L}_{gj}\,'\mathbf{S}_{gj}\,',\frac{\mathbf{L}_{gj}\,'\mathbf{M}_i\,'-\mathbf{L}_{gj}\,'\mathbf{S}_{gj}\,'}{tg\beta_b}\right);\qquad \mathbf{M}_i\,'=\left(\mathbf{L}_{gj}\,'\mathbf{M}_i\,',0\right)
\end{gathered}\tag{3}$$

$$\begin{gathered}
For\quad A_a:0\le\frac{\mathbf{L}_{gj}\,'\mathbf{M}_i\,'-\mathbf{L}_{gj}\,'\mathbf{S}_{gj}\,'}{tg\beta_b}\le b;\qquad For\quad A_b:\mathbf{L}_{gj}\,'\mathbf{S}_{gj}\,'\le\mathbf{L}_{gj}\,'\mathbf{M}_i\,'-b\cdot tg\beta_b\le\mathbf{L}_{gj}\,'\mathbf{E}_{gj}^{'}\\
For\quad A_c:0\le\frac{\mathbf{L}_{gj}\,'\mathbf{M}_i\,'-\mathbf{L}_{gj}\,'\mathbf{S}_{gj}\,'}{tg\beta_b}\le b;\qquad For\quad \mathbf{M}_i\,':\mathbf{L}_{gj}\,'\mathbf{S}_{gj}\,'\le\mathbf{L}_{gj}\,'\mathbf{M}_i\,'\le\mathbf{L}_{gj}\,'\mathbf{E}_{gj}^{'}
\end{gathered}$$

(d) Remove the repeat intersecting points. If two intersecting points are remained, the length of mesh line in the contact zone is the length between the two intersecting points, if one intersecting point is remained, the length of mesh line in the contact zone is 0.

(e) Finally, at time t, the sum of all contact lines in a contact zone is expressed as:

$$L\left(t+\Delta t,\mathbf{X}\right)=\sum_{i=1}^{i}l\left(M_i\,'\right)\tag{4}$$

The details of solving flaw are shown in Table 1.

Table 1 – Length of mesh lines in contact zone

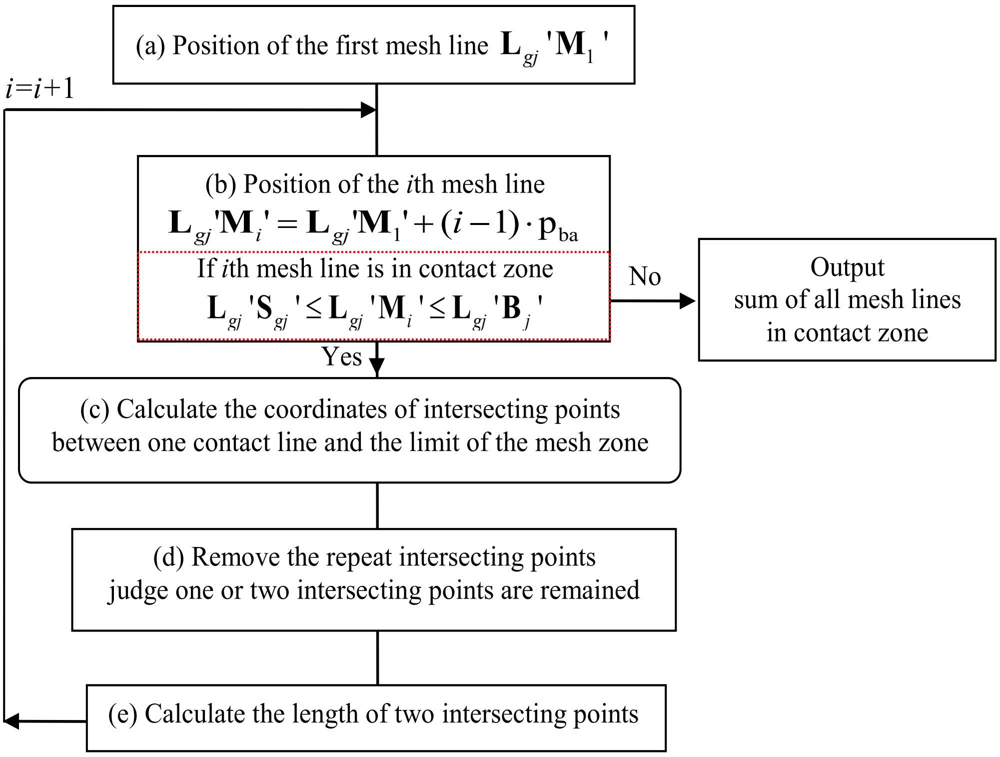

Appendix 2 – Time-step Newmark's integration scheme combined with fixed-point procedure and relaxation method

1 – Time-step Newmark integration scheme

The scheme of Newmark is a step by step integration method, can be used to solve the linear dynamic equilibrium equations written in the following form:

$$\mathbf{M\ddot{X}}+\mathbf{C\dot{X}}+\mathbf{KX}=\mathbf{F} \tag{1}$$

This scheme is based on the development of Taylor series, provided a rigorous approach to express the displacement and velocities as:

$$\begin{cases} X_{t+\Delta t}=X_t+\Delta t\cdot\dot{X}_t+\dfrac{\Delta t^2}{2}\ddot{X}_t+\dfrac{\Delta t^3}{6}\cdot\left[\dddot{X}_t\right]_1+\ldots\ldots \\ \dot{X}_{t+\Delta t}=\dot{X}_t+\Delta t\cdot\ddot{X}_t+\dfrac{\Delta t^2}{2}\cdot\left[\dddot{X}_t\right]_2+\ldots\ldots \end{cases} \tag{2}$$

Newmark truncated these equations and expressed them in the following form:

$$\begin{cases} X_{t+\Delta t}=X_t+\Delta t\cdot\dot{X}_t+\dfrac{\Delta t^2}{2}\ddot{X}_t+\alpha\Delta t^3\dddot{X}_t \\ \dot{X}_{t+\Delta t}=\dot{X}_t+\Delta t\cdot\ddot{X}_t+\beta\Delta t^2\dddot{X}_t \end{cases} \tag{3}$$

The acceleration is assumed to be linear within the time step Δt, the following equation can be given:

$$\dddot{X}_t=\frac{\ddot{X}_{t+\Delta t}-\ddot{X}_t}{\Delta t} \tag{4}$$

Where α and β are the weighting coefficients, $\dddot{X}_t$ in the Eq. (3) are substituted by Eq. (4) and produces Newmark's equations in standard form:

$$\begin{cases} \mathrm{X}_{t+\Delta t} = \mathrm{X}_t + \Delta t \cdot \dot{\mathrm{X}}_t + \left(\frac{1}{2} - \alpha\right) \Delta t^2 \cdot \ddot{\mathrm{X}}_t + \alpha \Delta t^2 \cdot \ddot{\mathrm{X}}_{t+\Delta t} \\ \dot{\mathrm{X}}_{t+\Delta t} = \dot{\mathrm{X}}_t + (1-\beta) \Delta t \cdot \ddot{\mathrm{X}}_t + \beta \Delta t \cdot \ddot{\mathrm{X}}_t \end{cases} \tag{5}$$

The scheme of Newmark becomes unconditional stable, if the weighting coefficients satisfy:

$$\alpha \geq \frac{1}{4} \cdot (0.5 + \beta)^2 \text{ and } \beta \geq 0.5 \tag{6}$$

Generally, weighting coefficients $\alpha = \frac{1}{4}$ and $\beta = 0.5$ are recommended.

Application time-step Newmark integration scheme on the equations of motion of planetary gear sets. The equations of motion of planetary gear sets, including the effect of gyroscopic and centrifugal forces and non-linear character, are expressed as:

$$\mathbf{M}\ddot{\mathbf{X}} + (2\Omega_C \mathbf{D} + \mathbf{C})\dot{\mathbf{X}} + \left(\mathbf{K_b} + \mathbf{K_G}(t, \mathbf{X}) + \Omega_C^2 \mathbf{L}\right)\mathbf{X} = \mathbf{F_0} + \mathbf{F_\Omega}(t) + \mathbf{F_{KE}}(t, \mathbf{X}) \tag{7}$$

Introducing Eq. (5) of displacement and velocity into Eq. (7), the form of the state equation therefore is:

$$\begin{aligned} &\left\{\left(\mathbf{K_b} + \mathbf{K_G}(\mathrm{t}, \mathbf{X}_t) + \Omega_C^2 \mathbf{L}\right) + \frac{\beta}{\alpha \Delta t}(2\Omega_C \mathbf{D} + \mathbf{C}) + \frac{1}{\alpha (\Delta t)^2} \mathbf{M}\right\} \mathbf{X}_{t+\Delta t} \\ &+ (2\Omega_C \mathbf{D} + \mathbf{C})\left\{\frac{\beta}{\alpha \Delta t} \mathbf{X}_t + (\frac{\beta}{\alpha} - 1)\dot{\mathbf{X}}_t + \Delta t(\frac{\beta}{2\alpha} - 1)\ddot{\mathbf{X}}_t\right\} + \mathbf{M}\left\{\frac{1}{\alpha (\Delta t)^2}\mathbf{X}_t + \frac{1}{\alpha \Delta t}\dot{\mathbf{X}}_t + \frac{1-2\alpha}{2\alpha}\ddot{\mathbf{X}}_t\right\} \\ &= \mathbf{F_0} + \mathbf{F_{\dot{\Omega}}}(\mathrm{t}) + \mathbf{F_{KE}}(\mathrm{t}, \mathrm{X}_t) \end{aligned} \tag{8}$$

2 – Fixed point procedure

Fixed point method allows us to solve non-linear equations. An iterative method is built, using a sequence which converges to a fixed point, and this fixed point is the exact solution of the equation which need be solved. For the equation of type:

$$\mathrm{f}(\mathbf{X}) = 0 \tag{9}$$

The idea is to reexpress Eq. (9) as the following form:

$$G\left(\mathbf{X}\right)=\mathbf{X} \tag{10}$$

let $\mathbf{X}^k$ be the solution of Eq. (10), we introduce a convergent sequence $\left(\mathbf{X}^n\right)^{n\geq 0}$ to the fixed point $\mathbf{X}^k$:

$$G\left(\mathbf{X}^k\right)=\mathbf{X}^{k+1} \tag{11}$$

$\left(\mathbf{X}^n\right)^{n\geq 0}$ will be the solution of Eq. (9).

The equations of motion of planetary gear can be expressed as the following form:

$$\begin{aligned}
&\left\{\left(\mathbf{K_b}+\mathbf{K_G}\left(\mathrm{t},\mathbf{X}_\mathrm{t}^\mathrm{k}\right)+\Omega_\mathrm{C}^2\mathbf{L}\right)+\frac{\beta}{\alpha\Delta\mathrm{t}}\left(2\Omega_\mathrm{C}\mathbf{D}+\mathbf{C}\right)+\frac{1}{\alpha(\Delta\mathrm{t})^2}\mathbf{M}\right\}\mathbf{X}_{\mathrm{t}+\Delta\mathrm{t}}^{\mathrm{k}+1}\\
&+\left(2\Omega_\mathrm{C}\mathbf{D}+\mathbf{C}\right)\left\{\frac{\beta}{\alpha\Delta\mathrm{t}}\mathbf{X}_\mathrm{t}^{\mathrm{k}=1}+\left(\frac{\beta}{\alpha}-1\right)\dot{\mathbf{X}}_\mathrm{t}^{\mathrm{k}=1}+\Delta\mathrm{t}\left(\frac{\beta}{2\alpha}-1\right)\ddot{\mathbf{X}}_\mathrm{t}^{\mathrm{k}=1}\right\}+\mathbf{M}\left\{\frac{1}{\alpha(\Delta\mathrm{t})^2}\mathbf{X}_\mathrm{t}^{\mathrm{k}=1}+\frac{1}{\alpha\Delta\mathrm{t}}\dot{\mathbf{X}}_\mathrm{t}^{\mathrm{k}=1}+\frac{1-2\alpha}{2\alpha}\ddot{\mathbf{X}}_\mathrm{t}^{\mathrm{k}=1}\right\}\\
&=\mathbf{F_0}+\mathbf{F}_{\dot{\boldsymbol{\Omega}}}\left(\mathrm{t}\right)+\mathbf{F_{KE}}\left(\mathrm{t},\mathbf{X}_\mathrm{t}^\mathrm{k}\right)
\end{aligned} \tag{12}$$

Rewrite Eq. (12) into the form:

$$\mathbf{X}_t^{k+1}=G\left(\mathbf{X}_t^k\right) \tag{13}$$

The system equations can be solved by this iterative method. The numerical solution procedure is detailed in Table 2. It combines a time-step Newmark integration scheme, a fixed-point method aimed at updating mesh geometry based on the DOFs, a relaxation method is adopted to control the speed of mesh geometry update and a unilateral normal condition which sets mesh stiffness to zero when contact is lost on the associated mesh. In an instant, these differential equations and contact conditions are resolved simultaneously.

Table 2 – Planetary dynamic model with Newmark integration scheme combined fixed-point procedure and relaxation method

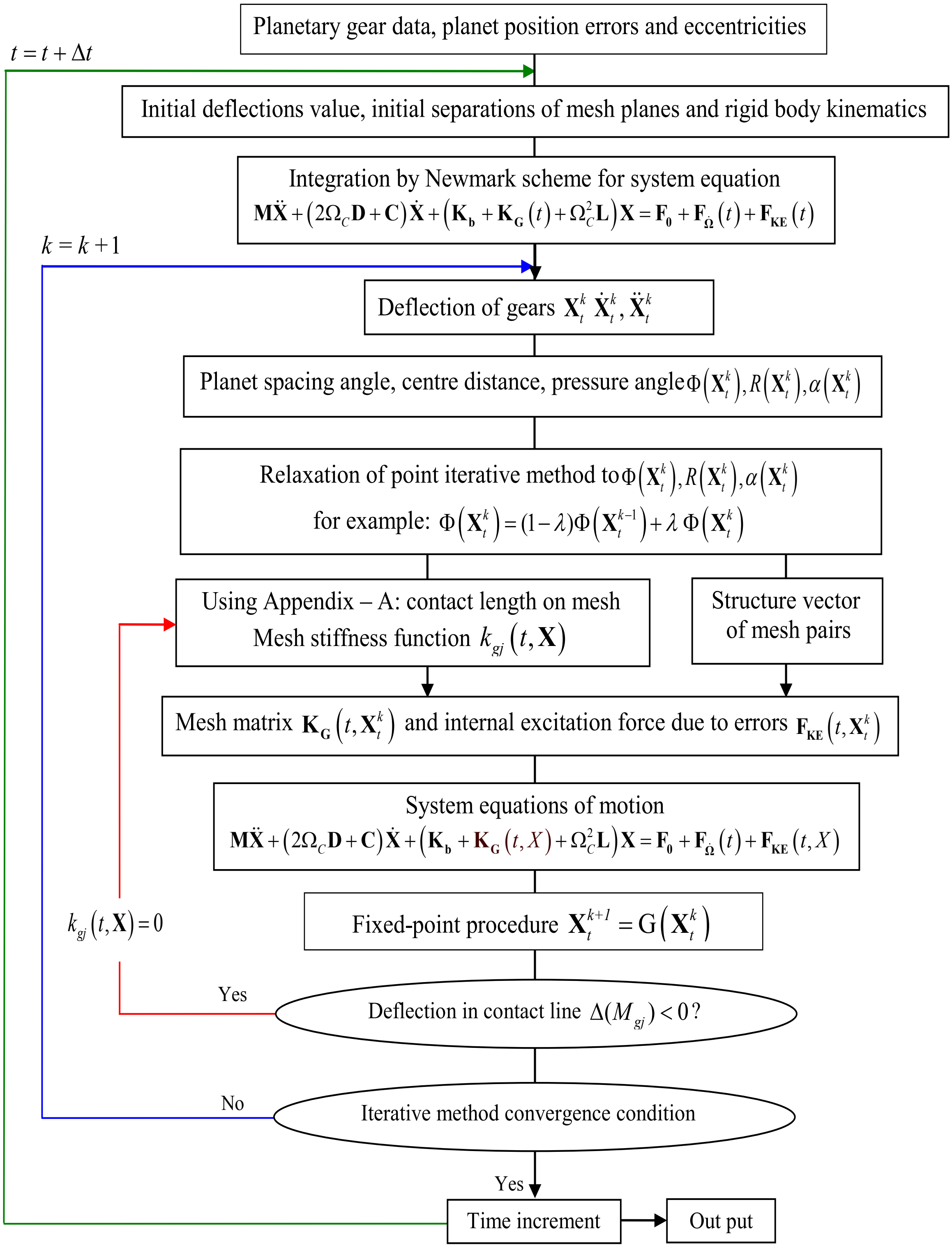
Planetary gear data, planet position errors and eccentricities
$t = t + \Delta t$
Initial deflections value, initial separations of mesh planes and rigid body kinematics
Integration by Newmark scheme for system equation
$\mathbf{M}\ddot{\mathbf{X}} + (2\Omega_C\mathbf{D} + \mathbf{C})\dot{\mathbf{X}} + (\mathbf{K}_\mathbf{b} + \mathbf{K}_\mathbf{G}(t) + \Omega_C^2\mathbf{L})\mathbf{X} = \mathbf{F}_\mathbf{0} + \mathbf{F}_{\dot{\Omega}}(t) + \mathbf{F}_\mathbf{KE}(t)$
$k = k + 1$
Deflection of gears $\mathbf{X}_t^k\ \dot{\mathbf{X}}_t^k, \ddot{\mathbf{X}}_t^k$
Planet spacing angle, centre distance, pressure angle $\Phi(\mathbf{X}_t^k), R(\mathbf{X}_t^k), \alpha(\mathbf{X}_t^k)$
Relaxation of point iterative method to $\Phi(\mathbf{X}_t^k), R(\mathbf{X}_t^k), \alpha(\mathbf{X}_t^k)$
for example: $\Phi(\mathbf{X}_t^k) = (1-\lambda)\Phi(\mathbf{X}_t^{k-1}) + \lambda\,\Phi(\mathbf{X}_t^k)$
Using Appendix – A: contact length on mesh
Mesh stiffness function $k_{gj}(t, \mathbf{X})$
Structure vector of mesh pairs
Mesh matrix $\mathbf{K}_\mathbf{G}(t, \mathbf{X}_t^k)$ and internal excitation force due to errors $\mathbf{F}_\mathbf{KE}(t, \mathbf{X}_t^k)$
System equations of motion
$\mathbf{M}\ddot{\mathbf{X}} + (2\Omega_C\mathbf{D} + \mathbf{C})\dot{\mathbf{X}} + (\mathbf{K}_\mathbf{b} + \mathbf{K}_\mathbf{G}(t, X) + \Omega_C^2\mathbf{L})\mathbf{X} = \mathbf{F}_\mathbf{0} + \mathbf{F}_{\dot{\Omega}}(t) + \mathbf{F}_\mathbf{KE}(t, X)$
$k_{gj}(t, \mathbf{X}) = 0$
Fixed-point procedure $\mathbf{X}_t^{k+1} = \mathrm{G}(\mathbf{X}_t^k)$
Yes
Deflection in contact line $\Delta(M_{gj}) < 0$?
No
Iterative method convergence condition
Yes
Time increment
Out put

FOLIO ADMINISTRATIF

THESE SOUTENUE DEVANT L'INSTITUT NATIONAL DES SCIENCES APPLIQUEES DE LYON

NOM : GU DATE de SOUTENANCE : 11 Avril 2012
(avec précision du nom de jeune fille, le cas échéant)

Prénoms : Xiaoyu

TITRE : INFLUENCE DES ERREURS DE POSITION ET EXCENTRICITES SUR LA DYNAMIQUE D'UN TRAIN PLANETAIRE
(INFLUENCE OF PLANET POSITION ERRORS AND ECCENTRICITIES ON PLANETARY GEAR DYNAMICS)

NATURE : Doctorat Numéro d'ordre : XXX

Ecole doctorale : MEGA de Lyon

Spécialité : Génie Mécanique

RESUME :

Un modèle de trains planétaires est proposé afin de tenir compte de l'influence d'erreurs de position et d'excentricités en lien avec d'éventuels montages 'flottants' sur le comportement dynamique d'une transmission. La formulation théorique repose sur le formalisme des torseurs de déplacements infinitésimaux pour simuler à la fois les erreurs géométriques et les degrés de liberté du modèle. Une des propriétés principales de cette approche est que la géométrie des engrènements et les excitations correspondantes sont couplées aux degrés de liberté, conduisant ainsi à des excitations complexes présentant des modulations d'amplitude et de phase. Les résultats de simulation sont comparés avec des mesures sur banc d'essai et un très bon accord est obtenu en terme de partage de charge entre les satellites, validant ainsi le modèle de contact développé. Enfin, des résultats d'études paramétriques portant sur le rôle de certaines erreurs ainsi que sur l'apport éventuel de solaire et/ou satellites flottants dans des applications grandes vitesses concluent ce travail de thèse.

(A dynamic model of planetary gears is presented which accounts for planet position errors and eccentricities for either rigid mounts or floating members. The theoretical formulation relies on infinitesimal generalised displacement screws which can simulate both errors and deflections. A unique feature of this model is that mesh properties (geometry and excitations) are coupled with the degrees-of-freedom thus leading to complex frequency and amplitude modulated excitation sources. For a number of planetary gears, it is found that the simulated load sharing between the planets compare well with the experimental evidence thus validating the contact modelling strategy. Finally, the results of extensive parameter analyses are displayed which illustrate the role of certain errors along with the interest and drawbacks of floating sun-gears or planets in high-speed applications.)

MOTS-CLES : Trains planétaires, Comportement dynamique, Erreurs de montage, Excentricités, Membres flottants, Charges sur les contacts, Trajectoires, Vitesses critiques.
(Planetary gears, Dynamics, Errors, Floating members, Tooth forces, Trajectories, Critical speeds)

Laboratoire (s) de recherche : Laboratoire de Mécanique des Contacts et des Structures
UMR CNRS-INSA n° 5514

Directeur de thèse : Professeur Philippe VELEX

Président de jury : Professeur Georges JACQUET-RICHARDET

Composition du jury : Samuel DECQUERELLE, Georges JACQUET-RICHARDET, Rober G. PARKER, Karsten STAHL, Philippe VELEX.